The magnetization and relative paleointensity of experimentally deposited natural sediments

A Thesis
SUBMITTED TO THE FACULTY OF THE
UNIVERSITY OF MINNESOTA
BY

Frank R. Molinek III

IN PARTIAL FULFILLMENT OF THE REQUIREMENTS
FOR THE DEGREE OF
MASTER OF SCIENCE

Joshua Feinberg, Dario Bilardello

June 2017

Acknowledgements

I would like to thank the National Science Foundation (NSF/EAR1447035) for funding this project over the last two years. Thanks to Dario Bilardello and Joshua Feinberg for their guidance and support throughout this project, and Lee Penn for sitting on my committee. Thanks to Anthony Runkle and Alan Knaeble at the MGS for their help in identifying and procuring the sediment used in our experiments. Thanks to Peat Solheid for help building the Helmholtz coils and input on results along the way. Thanks to Dan Maxbauer for his help with using MaxUnmix. Thanks to Mike Jackson for help with the DRM modelling, and input throughout the process. Thanks to Bruce Moskowitz for helping to identify the cause of the decreasing remanence during ARM acquisition. Thanks to Jonathon Cooper at Carleton College for his support and advice. Thanks to the rest of the Institute of Rock Magnetism, especially Michelle Stillinger, for their input and advice.

Abstract

The magnetization of a sediment occurs when ferromagnetic detrital particles align with a depositional magnetic field. The geomagnetic field can be approximated by a dipole that averages to share an axis with the rotation of the Earth. This field exerts a magnetic torque on ferromagnetic particles such as magnetite. However, processes including flocculation, contact with the substrate, bioturbation, and compaction disrupt this alignment, leading to shallowed remanent inclinations and biased intensities. The dependence of paleointensity on the inclination of the depositional field leads to complications in interpretations, despite the relative continuity and ubiquity of the global sedimentary record. We present a series of 12 deposition experiments in varying field strengths and inclinations, and attempt to correct relative paleointensity estimates using the anisotropy of anhysteretic remanence. We find experimentally that this correction reduces the inclination dependence of relative paleointensity, suggesting that it should also improve those estimates in naturally occurring sediments.

Table of Contents

List of Tables

List of Figures

1. The Fundamentals of Detrital Remanent Magnetizations

The magnetization of a sediment or sedimentary rock results from the alignment of detrital magnetic grains with an ambient field during deposition and lithification. However, there are many complex processes that disrupt this simple model. These deviations, examined in detail below, produce shallowed remanent inclinations and biased remanent intensities (e.g. Verosub, 1977; Tauxe and Kent, 1984; Shcherbakov and Sycheva, 2010). As sediments are a continuous and globally ubiquitous geologic record compared to igneous rocks, they are a prime target of researchers investigating the history of the magnetic field and geodyanamo or using magnetostratigraphy as a geochronometer (Constable and Tauxe, 1996). Thus, there is a long history of attempting to explain and correct the inherent errors of sedimentary magnetizations to improve their usefulness as a tool for Earth scientists.

This section examines the entire process of the acquisition of a detrital remanent magnetization (DRM), from the origins of the Earth's magnetic field, to the physics of magnetic minerals and the chemical and physical processes that govern their alignment (or lack thereof) during deposition. Then, section two presents a first experimental approach to correcting sedimentary magnetizations with the intent of improving estimates of relative paleointensity.

1.1 The Earth's magnetic field

This section, concerning the fundamentals of the Earth's magnetic field, is based on the work of Butler, 1992.

In natural settings, the ambient field with which detrital particles align during deposition is that of the Earth. About 90% of the magnetic field as experienced on the

Earth's surface can be approximated by a simple dipole, called the geocentric axial dipole (GAD) model (Fig. 1.1).

At any given time, the orientation of this dipole is inclined to the Earth's rotation axis, so that the magnetic poles do not align with geographic North and South. The orientation of the dipole relative to the rotational axis varies through time in the process of secular variation. Secular variation consists of both changes in the dipole field, as well as shorter-term variations in the non-dipole component of the Earth's field. Over time spans of about 10^3 years, however, secular variation averages so that the GAD orientation and the Earth's rotational axis are approximately equal. The axes exhibit this relationship independently of polarity switches of the Earth's magnetic field.

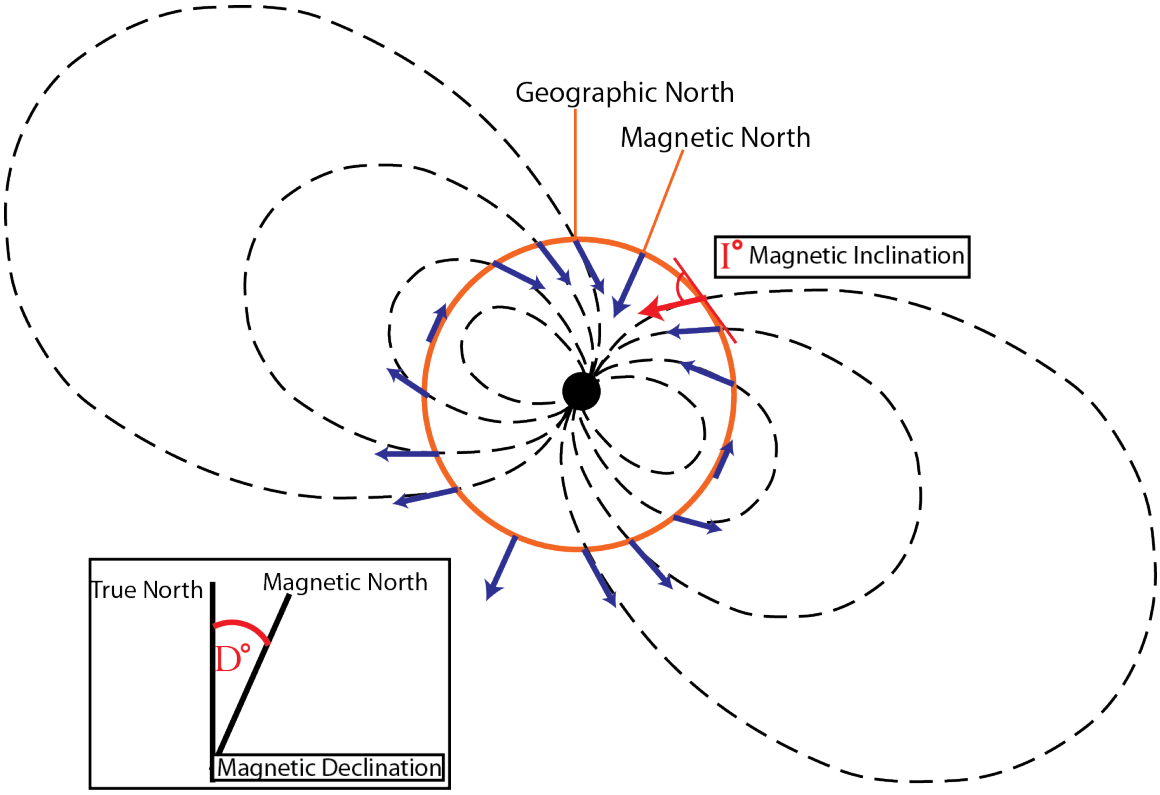

Figure 1.1. The Earth's magnetic field, with the magnetic dipole inclined to the rotation axis (represented by geographic north. The inclination is the angle between horizontal at a point on the Earth's surface (orange circle) and the vertical component (blue arrows) of the geomagnetic field (dashed lines). Declination is the angle between true geographic north and magnetic north at a given location. Redrawn after Butler (1992) and Campbell, 2003.

The mechanism that creates the magnetic field of the Earth has been the subject of numerous studies, and is still the subject of investigation (e.g. Davies and Constable, 2014; Ziegler and Constable, 2015; Buffet, 2016; Yadav et al., 2016; Veikkolainen et al., 2017). However, the favored explanation for the geomagnetic field is a self-exciting magnetohydrodynamic dynamo, or geodynamo.

There are several main necessary conditions that a geodynamo model must satisfy to be a plausible mechanism for the origin of the geomagnetic field. First, there must be a moving electrical conductor, and this conductor must be exposed to an initial magnetic field. Then, interactions between this magnetic field and the conductor must produce positive feedback that sustains the field. Finally, for this positive feedback to occur, energy must be supplied to replace that which is lost to electrical resistivity in the system.

These conditions are likely met by the liquid iron-nickel outer core of the Earth. This material is an electrical conductor that is capable of producing the types of interactions that would create a sustaining geomagnetic field. Additionally, about 25% of the total geothermal flux, mostly generated by freezing of the outer core, would provide sufficient energy to sustain the field. In this model, secular variation and non-dipole components of the magnetic field can be explained by fluid-eddy currents at the core-mantle boundary.

On the Earth's surface, the magnetic field at a given point can be described by a three-component vector (H). This vector, which represents the magnetic field line that intersects the Earth's surface at that point, can also be expressed with the declination, inclination, and intensity of the magnetic field (Fig. 1.1). These value vary based on latitude, longitude, and any non-dipole field components present at a location on the

Earth's surface. The declination is the angle between the horizontal component of the magnetic field and a line of longitude. In the ideal, secular variation-averaged, GAD model, where the GAD shares an axis with the rotation of the Earth, declination would be 0° at all points. However, on smaller time scales the magnetic declination deviates from the ideal GAD model due to the inclination of the dipole. Magnetic inclination is the small angle between the tangent line to the Earth's surface at that point and the vertical component of the geomagnetic field.

1.2 Magnetism of detrital minerals

This section, concerning the fundamentals of the magnetic properties of relevant minerals, is based on the work of Butler, 1992.

In addition to a depositional magnetic field, other necessary element of a DRM is a detrital magnetic particle that will align with it. The magnetic characteristics of a solid material are determined by individual atomic magnetic moments and their interactions within a mineral structure. Some solid materials have atomic magnetic moments because of the orbital and spin motions of electrons. These are typically transition element solids, especially iron, that have an unfilled 3d electron orbital.

When there are no strong atomic magnetic moments present in a solid, the material will acquire a small induced magnetization (M_i) in the opposite direction of an applied field. This "diamagnetic" response is present in all materials, but atomic magnetic moments completely overwhelm it when they are present. The diamagnetic response is a linear, negative dependence of M_i on H.

If a solid material contains atoms with magnetic moments, but these are non-interacting, it will exhibit a paramagnetic response. In these cases, there is a positive, linear dependence of M_i on H. After the applied field, H, is removed in both diamagnetic

and paramagnetic materials, M_i will revert to zero as the atomic magnetic moments oscillate randomly.

The ferromagnetic response is of greater interest to studies concerned with the remanent magnetization a material retains after the applied field is removed. In ferromagnetic materials, adjacent atomic magnetic moments interact strongly. The induced magnetization in ferromagnetic materials is orders of magnitudes larger than a diamagnetic or paramagnetic material in the same applied field. Additionally, interactions between atomic magnetic moments prevent the magnetization of the material from returning to zero after removal of the applied field, and the remaining magnetization is the magnetic remanence (M_r) of the material. The magnetization of ferromagnets increases with increasing applied fields until it reaches saturation, the saturation magnetization (M_s), above which the material can no longer acquire increasing induced magnetization. Removal of a saturating field will result in the saturation remanent magnetization (M_{rs}).

In many sedimentary depositional settings, including the experiments in this study, the primary ferromagnetic iron-titanium oxides carrying magnetic remanence are magnetite and hematite. The basic chemical unit of magnetite is Fe_3O_4, though titanium can substitute in the form of ulvöspinel (Fe_2TiO_4) as a solid solution of titanomagnetites between endmembers magnetite and ulvöspinel. Intermediate compositions have the generic formula $Fe_{3-x}Ti_xO_4$ (Fig. 1.2).

Magnetite has a cubic-close packed crystallographic lattice with an inverse spinel structure. The primary crystallographic unit of magnetite consists of 16 Fe^{3+}, 8 Fe^{2+}, and 32 O^{2-}. The distribution of the cations in the tetra- and octahedral sublattices, and the exchange coupling between them, control the magnetic properties of titanomagnetites.

Titanohematites have a hexagonal close packed lattice and a chemical unit of varying titanium concentration given as $Fe_{2-x}Ti_xO_3$. When x is equal to zero the mineral is hematite, and if x = 1 it is ilmenite (Fig. 1.2). The atomic magnetic moments in the structure tend to align within the <0001> crystallographic plane, and are contained within the basal cation plane (within the "platy" structure of the hematite mineral).

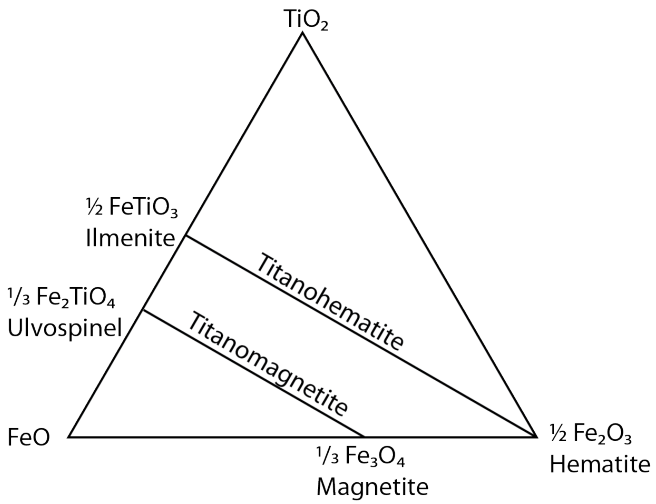

Figure 1.2. Ternary diagram of the iron-titanium oxides. Redrawn after Butler, 1992.

Magnetic mineral domains

The magnetic moments of the ferromagnetic grains are held in domains, or regions of a mineral with variably oriented magnetic moments, which function to minimize the magnetostatic energy within a grain. The simplest case occurs in small grains, where there is space for only one domain (Fig. 1.3a). The threshold size for a single domain (SD) grain depends upon the shape and saturation magnetization of the mineral. A typical SD threshold grain size for magnetite, as an example, is <0.1 μm if the mineral is cubic, or <1 μm if it is highly elongate. If the grain is much larger than that, there will be multiple magnetic domains (multi-domain or MD grains) to maintain energetically favorable conditions (Fig. 1.3b). These domains will have magnetic

moments that have variable orientations, reducing the total magnetization of the particle and its ability to carry remanence.

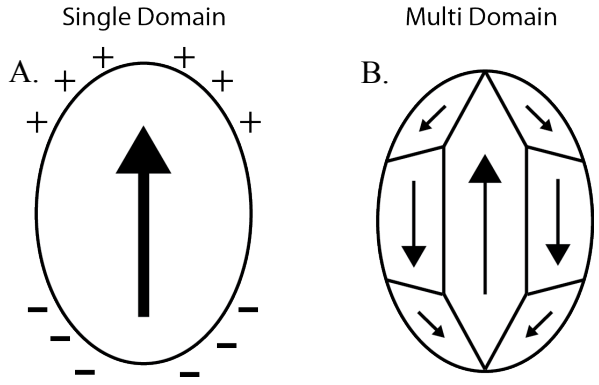

Figure 1.3. Magnetic domains. On the left is a single domain particle with a simple dipole moment. On the left is a multi-domain particle with 7 domains in various orientations, separated by domain walls. SD grains are reliable recorders of magnetic remanence, while MD particles are not. This figure is schematic and not to scale. Redrawn after Butler, 1992.

In the transitory grain sizes between SD and MD particles are pseudo-single domain (PSD) grains. These particles have several magnetic domains but are still small enough to reliably carry a magnetic remanence. An elongate magnetite particle is typically PSD in the 1 to 10 μm size range.

Shape and magnetocrystalline anisotropy

A final important aspect of mineral magnetism is the anisotropy, both shape and magnetocrystalline, of ferromagnetic grains, which are responsible for the differential grain size thresholds for SD elongate or cubic magnetite. Because of shape anisotropy, a highly elongate SD mineral has its lowest magnetostatic energy when magnetized along its long axis. Similarly, the anisotropy of certain ferromagnetic grains is controlled by their crystallographic sublattices. In minerals with magnetocrystalline anisotropy, energy is minimized when the magnetic moment is in a magnetic “easy” direction that is

dependent on the crystal and atomic structure. Hematite is an example of this - when atomic magnetic moments tend to align within the <0001> crystallographic plane it is due to the magnetocrystalline anisotropy of the mineral.

1.3 The remanence of rocks

This section, concerning the types of magnetic remanence, is based on the work of Butler, 1992.

The remanence of individual ferromagnetic grains, when those grains are bound in a rock along with other minerals, add vectorially to a total magnetic remanence for that rock. The remanent magnetization of a rock that has not experienced any laboratory treatment is the natural remanent magnetization (NRM) and may be acquired by several mechanisms. As one example, thermoremanent magnetization (TRM) results when the magnetic moment of ferromagnetic minerals are “locked in” an induced direction as the material cools past a characteristic blocking temperature, below which thermal energy has decreased to the point that atomic magnetic moments can interact. Another mechanism for NRM acquisition is chemical remanent magnetization (CRM), and it is acquired when chemical changes to a material (i.e. low-temperature oxidation, exsolution, diagenesis, or dehydration) allow magnetic moments to realign with a magnetic field.

Sedimentary Magnetizations

In sedimentary rocks, central to this study, magnetization is acquired as a detrital remanent magnetization (DRM). At the simplest level, a DRM is acquired through the alignment of a detrital ferromagnetic particle with an ambient field during deposition. Unlike a TRM, where magnetic moments internal to grains align with an ambient field

before locking in, DRMs occur when fine ferromagnetic particles rotate in a fluid so that their internal magnetic moments (original TRMs, CRMs, etc.) align. In other words, magnetic grains enter the depositional system already magnetized.

The DRM process can be divided into two distinct parts: a depositional (DRM) and post-depositional remanent magnetization (pDRM) (Verosub, 1977). A depositional DRM refers to the process of magnetic grain alignment during settling, through the water column and until contact with the substrate; a post-depositional DRM refers to further movement of detrital magnetic particles after they come to rest on the substrate.

First, we examine the processes of depositional DRM as outlined by Nagata (1961) and Collinson (1965). The classic model of a DRM only considers the case of an isolated spherical magnetic particle aligning with an ambient field in the moment before contact with the substrate. The fundamental physical processes at work in this model are expressed through the equation:

$$\Omega \cdot \left(\frac{d^2\theta}{dt^2}\right) + \beta \cdot \left(\frac{d\theta}{dt}\right) + mH \cdot sin\theta = 0 \qquad (1.1)$$

Where θ is the angle between the magnetic moment of the particle and the direction of the ambient field, *t* is time, the first term, Ω, represents the moment of inertia, β represents the rate of rotation due to viscous drag, and *mH* is the aligning torque, Γ, exerted by the ambient field (*H*) on the magnetic moment of the particle (*m*). The first and second terms are defined as:

$$\Omega = \left(\frac{\pi D^5 p}{60}\right) \qquad (1.2)$$

and

$$\beta = \pi D^3 \eta \qquad (1.3)$$

Where D is the diameter of the particle, p is the density of the particle, and η is the viscosity of the fluid.

In geologically realistic conditions, Ω is negligible as the grains involved in remanence are smaller than 10 μm and the grain rotates quickly and θ approaches zero so that $sin\theta = \theta$. Taking this into account, equation 1.1 reduces to

$$\frac{d\theta}{dt} = \left(\frac{-mH\theta}{\pi D^3 \eta}\right) \quad (1.4)$$

which describes how θ will decrease from an initial angle, θ_0. Furthermore, the function of the angle θ changing through time:

$$\theta(t) = \theta_0 \, exp\left(\frac{-t}{t_0}\right) \quad (1.5)$$

describes an exponential alignment process where t_0 is a characteristic alignment time period for a given depositional condition within which θ decreases from $\theta_0$to θ_0/e, and is defined as:

$$t_0 = \left(\frac{\pi D^3 \eta}{mH}\right) \quad (1.6)$$

To further simplify, the magnetic moment of a spherical particle is defined as:

$$m = \left(\frac{\pi D^3 M}{6}\right) \quad (1.7)$$

where *M* is the net magnetic moment of a unit of volume. Substituting this back into equation 1.6, we find:

$$t_0 = \frac{6\eta}{m \cdot H} \quad (1.8)$$

With geologically reasonable values for *m, H,* and η, the time for perfect alignment is less than around 0.1 second (magnetite) to 1 second (hematite; Collinson, 1965). This would imply a rapid and complete alignment of detrital grains with an ambient field, so that a DRM would be fully saturated. However, decades of experimentation and investigation of natural sediments find that the magnetization of sediments is generally orders of magnitudes below saturation magnetization, and that the inclination recorded is

usually erroneous relative to the depositional field (e.g. Verosub, 1977; Tauxe and Kent, 1984; Shcherbakov and Sycheva, 2010; Heslop et al., 2014).

1.4 Sources of error in a DRM

The error of a DRM results from the misalignment of individual magnetic grains with respect to an ambient field. The causes of this misalignment are numerous and complex and we attempt to parse them below.

McNish and Johnson (1938) were among the first to publish concerning the magnetization of sediments, following years of work on the magnetization of igneous rocks (Verosub, 1977). Since that time, many workers have studied the magnetization of natural sediments ranging from glacial varves to deep-sea sediments to marginal and lacustrine deposits. While many studies report a DRM of naturally deposited sediments, the accuracy with which a DRM records an applied magnetic field has been a major question (see Verosub, 1977 and references within). This line of inquiry has centered on inclination error, post-depositional remanent magnetization (pDRM), and the ability of sediments to efficiently align.

An early effort to explain the inclination error invoked gravitational effects on grains of different shapes. Either the rolling of magnetic spherical particles or flattening of the more platey particles owing to gravitational forces upon contact with the substrate were postulated, introducing the “plates and spheres” models (King, 1955; Griffiths et al., 1960; Tauxe and Kent, 1984).

King (1955) was among the first to report results of redeposition experiments. The premise of these experiments is to let sediment with a magnetic component settle in a water column under an artificially induced and controlled magnetic field. King found that inclination errors in the remanent magnetic vector of these sediments could be

caused by the slope of the bedding plane, water currents just above the sediment-water interface, and the state of dispersal of the sediment during deposition. King concluded that the most important parameter was the ratio of platey (typically hematite) and spherical (typically magnetite) particles making up the magnetic component of the sediment. In this model, the spheres align perfectly with the ambient magnetic field on a horizontal depositional bed, while the platey particles settle so that the plane containing their magnetic moment is horizontal (Fig. 1.4a). Furthermore, the fraction of magnetic particles that are spheres is the flattening factor *f* used in the expression of the inclination error:

$$\tan (I_M) = f \tan (I_H) \qquad (1.9)$$

where I_M is the measured remanent inclination, and I_H is the inclination of the depositional field (King, 1955).

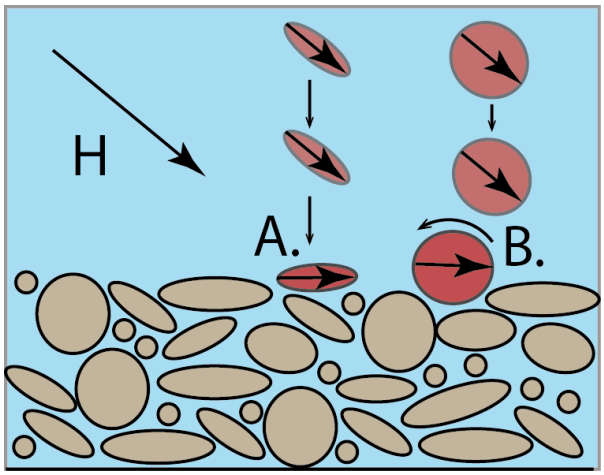

Figure 1.4. Inclination error in platey and spherical particles, represented in schematic two-dimensions. A) An elongate platey particle aligned with the ambient field (H) flattens to the bedding plane upon contact with the substrate. B) A spherical particle rolls upon encountering an uneven surface. Both processes contribute to inclination shallowing.

Griffiths et al. (1960) refined this model and proposed a directional error due to the rolling of particles when they encounter the substrate (Fig. 1.4b). In this model, inclination error is primarily due to spherical particles rolling into depressions between

grains on the substrate. Assuming a random distribution of rolling directions for the spheres, the declination of each particle will err, but the average of the whole sediment will remain accurate, while the inclination will on average be shallower than the applied field. In this model, the flattening factor, *f*, is the average angle that the spheres roll (Griffiths et al., 1960; Bilardello, 2013).

Based on the aforementioned studies, two models involving mechanical interaction of magnetic particles with the plane of sedimentation compete to explain inclination error. Tauxe and Kent (1984) conducted redeposition experiments using sediment containing both magnetite, which is generally more equant, and hematite, which is generally platey, and tried to determine which particles are responsible for the inclination error, and by extension, determine which model was correct. Their results, however, were inconclusive in this respect.

Bilardello et al. (2013) and Bilardello (2013) take the next step in this line of questioning, conducting deposition experiments with purely spherical and purely platey magnetic particles. The goal of these studies was to directly compare the influence of each particle shape on DRM acquisition by running simplified experiments to isolate individual factors. Bilardello (2013) found that platey particles do not solely align with the bedding plane, as proposed by King (1955), and are not the sole cause of inclination shallowing. Bilardello et al. (2013) found that measurements of inclination of the purely spherical particles were much more repeatable, and the influence of rolling or translation of spheres on inclination error is confirmable. Thus, both particle shapes, can contribute to the inclination error.

Inclusions of small magnetic particles in larger siliciclastic grains can also be a cause of lower than expected magnetization of a DRM (Hatfield et al., 2013; Chang et al., 2016). Using magnetic techniques and transmission electron microscopy (TEM),

Chang et al., (2016) found a widespread occurrence of silicate-hosted ferromagnetic particles in marine sediments. These inclusions may appear to be individual single-domain or PSD grains when the material is analyzed using magnetic technique, but TEM revealed that many were actually hosted within larger grains. This could lead to protection of the ferromagnetic inclusions from chemical processes during diagenesis - potentially leading to better preservation of a remanent magnetic signal than independent magnetic particles.

However, the deposition of larger (> ~18-20 μm) silicate particles containing ferromagnetic inclusions is controlled by gravitational and hydrodynamic forces rather than magnetic torque induced by the geomagnetic field, contributing to the randomization of remanent directions. In host particles smaller than about 18 μm, SD ferromagnetic inclusions can contribute meaningfully to a DRM, dependent upon their aspect ratio (Chang et al., 2016). Thus a sediment may appear to be an ideal carrier of remanence after magnetic analysis, but grain inclusions could cause a lower net magnetization than expected, and an erroneous direction.

1.5 Flocculation

This section is based on the work of Stumm and Morgan (1996) and Katari and Tauxe (2000).

The process of flocculation, where aggregation of individual particles creates larger groups of particles called flocs, can also lower the magnetization of a DRM and create bias in the remanence.

In aqueous slurries of clay-sized particles, flocculation occurs spontaneously after the cessation of mechanical agitation. Clay sized mineral grains can be colloidal when suspended in water, and carry charges due to their surficial chemistry. Colloidal

particles in a solution acquire charges by chemical reactions on their surface, isomorphous replacement of ions within the solid crystal lattice, or adsorption of a surfactant ion. Once the particles in the colloid solution have a surface charge, counter ions compensate by forming a diffuse layer where ions are brought into contact with the mineral by their thermal motions. This results in an electrical double layer with fixed charges at the particle's surface and another layer diffusely distributed through the liquid in contact with the mineral surface.

In a colloidal slurry, both double-layer repulsive and van der Waals attractive forces act on the charged suspended particles. The repulsive force (V_R) is dependent upon double-layer thickness and distance between particles:

$$V_R \propto e^{-\kappa x} \tag{1.10}$$

where x is the distance between particles and $\kappa$is the inverse thickness of the double layer, which varies as the square root of the ionic molarity of the solution.

The attractive van der Waals forces, on the other hand, depend on small charge fluctuations in atoms instead of the chemistry of the colloid solution. These fluctuations lead to mutually induced dipole moments between interacting atoms. Van der Waals forces are very small and decay rapidly between individual atoms. However, when a large number of atoms are involved, like when two mineral grains come into contact, the total attraction can be considerable. The van der Waals forces are inversely proportional to the third power of the distance between particles.

Thus, when two particles come into contact, the balance of attractive and repulsive forces determines whether the particles will aggregate to form a floc. In the absence of a strong repulsive force, Brownian motion brings particles close together, and van der Waals forces bond the particles. Brownian motion occurs when collisions with much smaller particles cause larger ones (i.e. H_20 molecules and a clay particle,

respectively) to move randomly in a fluid. When aggregate particle size exceeds 1 μm, Brownian motions ceases to drive flocculating collisions and differential settling rates or flow of the fluid bring particles together.

In saline waters, the presence of salt increases the molarity of ions in the solution, thus decreasing the double-layer repulsive force as κ increases in equation 1.10. This allows van der Waals forces to produce particle aggregation and the formation of floccules, since the attractive force depends on the distance between particles, not water chemistry. In fresh water, the process is more complex, but Droppo and Ongley (1994) found that flocculation in the absence of high concentrations of salt ions is due to suspended solid concentrations, percent organic carbon, and bacteria attached to particles. In a non-saline colloidal slurry of clay particles, high concentrations of those particles are likely a driver of flocculation.

The surface chemistry of relevant particles

The Fe cations on the surface of magnetite, as a relevant example, adsorb a hydroxyl anion from the dissociation of water. The adsorption forms an Fe-(OH) radical, which results in a negative surface charge as the hydroxyl radical dissociates acidicly, or in a positive surface charge if a proton balances a neutral surface. A simple model of these two pathways is:

$$Fe - (OH)_{(surface)} + H_2O = Fe - O^- + H_3O^+ \quad (1.11)$$

Or

$$Fe - (OH)_{(surface)} + H_3O^+ = Fe - (OH_2)^+ + H_2O \quad (1.12)$$

This charge is determined by the balance of H^+ and OH^- ions, or potential determining ions. The overall charge of an iron-oxide mineral's surface (C_S), then, is given as:

$$C_s = (F/A)(\Gamma_{H+} - \Gamma_{OH-}) \quad (1.13)$$

where F is the Faraday constant, A is the surface area of the mineral, and Γ is the number of H^+ or OH^- ions, respectively, adsorbed per unit area.

If $\Gamma_{H+} = \Gamma_{OH-}$, then the surface of the magnetite is electrically neutral, at the point of zero charge (PZC). This balance is dependent of the pH of the solution. If pH exceeds the PZC the surface charge will be negative, and if the pH is lower the charge will be positive. For magnetite, the pH at which there is no charge is approximately 7.4.

The surface charge of clays depends upon the arrangement of cations in the crystal lattice of the mineral. The general structure consists of layers of O^- or OH^- anions, with the remaining spaces, both within and between anion layers, filled by cation such as silicon, magnesium, iron, or aluminum. The surface charge of the larger, flat surfaces of the basal plane of the mineral results from cation substitutions and is negative - independent of pH. The edges of the particles, which constitute about 10% of the surface area, do have charges that depend on the pH of the solution, and can be negative or positive.

Flocculation and magnetization

The effect of flocculation on magnetization is to essentially lower the magnetic remanence and add to randomization of particle moment alignment (e.g. Van Vreumingen, 1993; Katari and Tauxe, 2000; Tauxe et al., 2006; Heslop 2007; Mitra and Tauxe, 2009; Shcherbakov and Sycheva, 2010). When magnetic particles that are capable of carrying a reliable remanence (SD or PSD ferromagnetic particles, like <10 μm magnetite) are bound into flocs, two processes are at play. First, if there is more than one magnetic particle bound into the floc, and the particles' magnetic moments are aligned differently respective to the ambient field, the direction and overall magnetization of the floc will be skewed and more variable than if only one magnetic particle was

contributing remanence (Fig. 1.5). Second, as the particle size increases with floc growth, the importance of magnetic torque diminishes as the role of hydrodynamic and gravitational forces increases, resulting in increased misalignment of the magnetic particles.

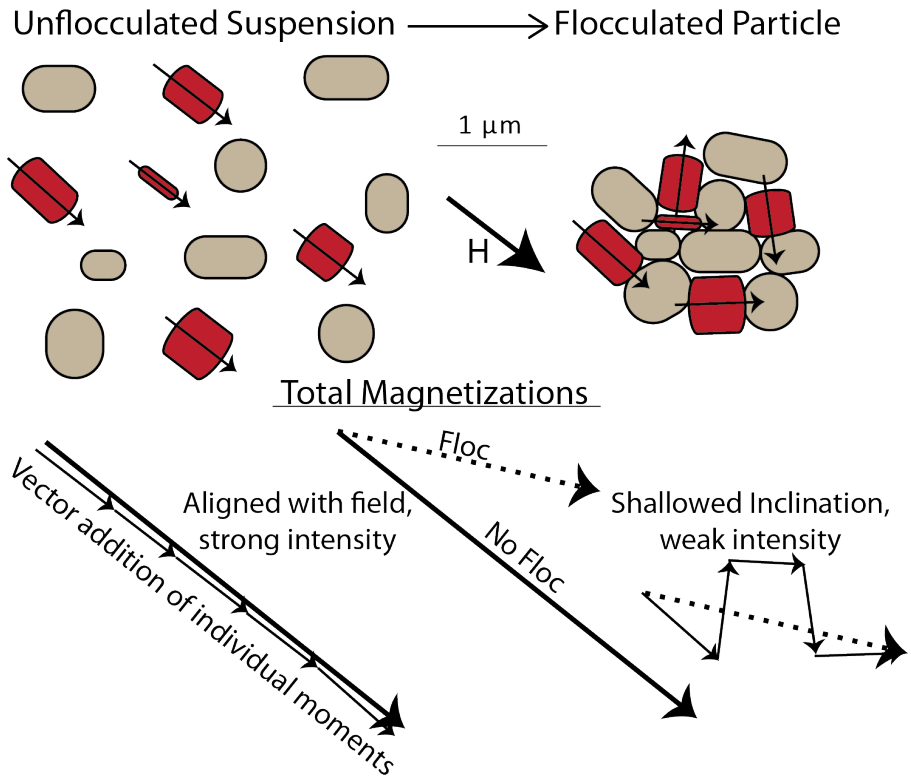

Figure 1.5. Flocculation and magnetization. (TOP) Sub-micron magnetic and nonmagnetic particles in an un-flocculated colloidal slurry experience bonding van der Waals forces to aggregate into a floccule. When the particles are isolated in suspension, they align with the magnetic field. When they are bound into a floc, their magnetic orientations are randomized. (BOTTOM) The magnetic directions of the isolated and flocculated particles. The magnetic moment add vectorially to produce a total magnetization. The particles in suspension align perfectly to produce a magnetization that is parallel to the ambient field with strong intensity (left). The flocculated particles are scattered in orientation, and their total magnetization is shallowed and weak relative to the ambient field (right).

1.6 Post-depositional processes

After deposition, the already-shallowed magnetic grains continue to experience directional changes, and can acquire a post-depositional remanent magnetization

(pDRM). Despite simplification in many models, the sediment/water interface is not typically well defined (Roberts et al., 2013). In the lowermost region of the water column, concentration of suspended particles increases in what is known as the nepheloid or benthic boundary layer. In the lowest parts of this layer, sediment is heavily flocculated and fluffy in texture. This is directly above the uppermost reaches of the sediment column, which contains large amounts of water and is often mixed by bioturbation.

As the sediment column becomes more consolidated with increasing depth, the sediment is no longer mixed and magnetic minerals no longer rotate freely with respect to the nonmagnetic components of the sediment. At this point, dewatering of clay-rich sediments and compaction during burial further rotates all grains, potentially causing further inclination shallowing.

In natural settings bioturbation plays an important role by “loosening” particles in the sediment column and allowing further rotation of magnetic grains, typically improving alignment with the ambient field (e.g. Irving and Major, 1964; Kent, 1973). When benthic organisms burrow they consume and expel sediment. This process reduces the density of the sediment, which reduces the forces opposing particle rotation via magnetic torque and Brownian motion of the submicron magnetic particles (Kent, 1973). The resultant sediment mixing in the top portion of the sediment column allows realignment with the geomagnetic field and the acquisition of a pDRM.

The other pDRM process of note is compaction and sediment dewatering, especially in clay rich sediments (e.g. Anson and Kodama, 1987; Arason and Levi, 1990; Kodama and Sun, 1990). Sun and Kodama (1992) conducted experiments where they applied increasing pressure (up to 0.157 MPa, simulating a burial depth of 400-500 m) to an artificial sediment containing kaolinite and illite clays, as well as magnetite with grain sizes of 0.45 and 2-3 μm. The same effects can be produced by allowing the sediment to

dewater by evaporation. They found that void space and inclination shallowing decrease rapidly up to 0.02 MPa, along with a 20-30% decrease in magnetic intensity. Continued compaction from 0.02 to 0.05 MPa causes moderate decreases in those parameters. Increasing pressure above 0.05 MPa has little effect on the magnetic remanence. Attempting to relate the experimental results to a natural setting scenario Sun and Kodama (1992) concluded that at burial depths up to about 200 meters, randomization of directions of magnetic minerals (by Brownian motions or other collisions in the sediment pore spaces) drives inclination shallowing and remanence decreases, but below 200 m magnetic particles attach to clay particles (by electrostatic or van der Waals forces) and further shallowing occurs as the clay fabric becomes horizontal. At burial depths corresponding to pressures greater than 0.05 MPa (several hundred meters deeper than 200 m) the sediment's fabric is already completely horizontal and no further shallowing occurs (Sun and Kodama, 1992).

During diagenesis, magnetic remanence is affected by such processes as the dissolution of iron oxides and growth of iron sulfides in the sulphate reduction zone (Roberts et al., 2013). These processes are controlled by organic carbon flux and the oxidation state of the sedimentary environment. However, these factors are not applicable to the experimental settings involved in this study, and a more comprehensive review can be found in Roberts et al. (2013).

1.7 Summary

The magnetic field of the Earth, produced by the geodynamo and approximated by a simple dipole, exerts a torque on ferromagnetic particles during sedimentary deposition that causes them to align. In ideal situations (an isolated magnetic particle settling uninterrupted) it is predicted that rapid and total alignment will occur. However, several factors disrupt this alignment and lead to error in a DRM. Particles may be

bound in flocs while settling, which can cause non-magnetic forces to overwhelm magnetic torque due to the large aggregate grain size. Additionally, if magnetic particles exist as inclusions in larger, non-magnetic grains, it is likely that the efficiency of their DRM will be reduced. When magnetic particles encounter the substrate, they may roll or flatten - further producing error. After deposition, bioturbation, Brownian motion, and compaction in the sediment column cause grains to rotate. All of these factors combine to shallow the inclination of remanent magnetization in sediments, and bias the intensity. Thus, despite the ubiquitous and continuous nature of the global sedimentary record, investigation of DRMs remains a challenging field fraught with uncertainty and biases.

2. Application of an anisotropy-based correction to relative paleointensity estimates of experimentally deposited sediments*

2.1 Introduction

Relative paleointensity (RPI) estimates derived from sediments and sedimentary rocks present both opportunities and challenges to those researchers who investigate them. Because of their relatively continuous nature, sedimentary records are a prime target for study of the past of the earth's magnetic field. However, the overall weak alignment of magnetic particles (e.g. Heslop et al., 2014) and inherent biases in their remanent magnetizations (e.g. Verosub, 1977; Tauxe and Kent, 1984; Shcherbakov and Sycheva, 2010) complicate interpretations. In this study we present a first experimental attempt at investigating these effects on RPI estimates in the laboratory.

Magnetic polarity reversals form the crux of magnetic geochronology and its application to the geologic timescale, but fluctuations in the intensity of the paleomagnetic field can be used for finer-scaled magnetostratigraphy (Roberts et al., 2013). Igneous rocks and archeological artifacts can record the absolute paleointensity of the ancient field by acquiring a thermoremanent magnetization when they cool past the magnetic carriers' unblocking temperatures. Laboratory magnetization and demagnetization experiments on these materials enable determinations of reliable absolute paleointensities (Thellier and Thellier,1959). Unlike continuous and globally ubiquitous sedimentary records, however, thermoremanent materials are sporadic in their temporal and spatial availability (Constable and Tauxe, 1996).

The magnetization of a sediment results from the alignment of already magnetized detrital grains with an ambient magnetic field during deposition (e.g. Nagata,

*A version of this chapter, with the same title, will be submitted for publication in summer, 2017, and is coauthored by Dario Bilardello.

1961). Thus, it is not possible to obtain direct absolute paleointensity values from sediments, and investigators of these records must rely upon estimates of RPI.

The intensity of the remanence is proportional to the particle's efficiency at aligning with the ambient magnetic field, the stronger the field, the higher degree of alignment (e.g. Butler, 1990; Heslop et al., 2014). Therefore, for sediments and sedimentary rocks the higher the magnetization, the higher the paleo field intensity likely was. However, the intensity of detrital remanence also depends on the grain size, composition, and concentration of the magnetic mineralogy, in addition to the depositional field. To attempt to account for these variations, Levi and Banerjee (1976) developed a technique for estimating RPI, which is calculated by normalizing the intensity of a detrital remanent magnetization (DRM).

Magnetic mineralogy, grain size and concentration vary widely across lithologies and even within the same depositional sequence, and the RPI method aims to compensate for these differences by normalizing the natural remanent intensity with an applied laboratory field that will account for such variations (Levi and Banerjee, 1976; Tauxe and Yamazaki, 2007, Roberts et al., 2013). A laboratory saturation remanence magnetization will fully align the magnetic moments within a sample and serve as a constant material property, enabling the estimation of the paleointensity. One can therefore simplistically view an RPI estimate as a measure of the degree of alignment of the magnetic grains, corrected for variations in mineralogy, grain size and concentrations. Realistically, however, for the technique to be successful, variation in grain size and concentration should not exceed ~30% within a sequence (Levi and Banerjee, 1976).

Using this technique, workers have used stacked sedimentary magnetic records to produce globally coherent models of the global axial dipole moment, dating back to 3 Ma

(Guyodo and Valet 1996, 1999, 2006; Valet et al., 2005; Ziegler et al., 2011). Attempts have been made at calibrating relative paleointensity records in order to obtain absolute values of depositional field strength by utilizing a constant factor to scale the RPI estimates and obtain an absolute field intensity determination (Constable and Tauxe, 1996; Korte and Constable, 2003, 2005, 2006; Korte et al., 2009; Korte and Constable, 2011; Korte et al., 2011; Nilsson et al., 2014; Panovska et al., 2015). The outstanding challenge is to place such techniques that utilize the relationship between a DRM and a depositional field on a more secure theoretical and empirical framework, so that future improvement may allow millennial-scale intensity records of the ancient magnetic field (Roberts et al., 2013).

Furthermore, it has long been recognized that DRM is an inefficient remanence acquisition mechanism, owing to the overall weak alignment (< a few %, e.g. Heslop et al., 2014) of the magnetic particles (more below). This alignment bias propagates into the RPI estimates and further offsets their accuracy.

The classic model of a DRM was laid out by Nagata (1961) and Collinson (1965). This model consists of isolated magnetic particles settling through a viscous medium (either air or water). Magnetic particles that enter the depositional system are influenced by the magnetic torque exerted by the Earth's field, depending on their volume, mass and magnetization. Opposing this aligning torque, motion of the particles is dampened by their moment of inertia, the viscous drag exerted by the settling medium, and mechanical interactions with the subsurface once the particles reach the sediment layer (Collinson, 1965). Assigning reasonable values for particle size, density, and magnetization, as well as water density, viscosity, gravitational acceleration and the Earth's field strength it is possible to calculate a characteristic alignment time by which all particles will be fully aligned with a depositional field according to this model:

$$t_0 = \frac{\lambda}{m \times H} \quad (2.1)$$

where *t* is the time to ideal alignment, λ is a viscosity coefficient of the fluid, *m* is the magnetization of the particle, and *H* is the strength of the ambient field. This function accurately describes the time to alignment of an isolated detrital magnetic particle and, for magnetic minerals in the size ranges of interest, predicts an efficient and almost instantaneous alignment with the Earth's field (Roberts et al., 2013). However, this model does not account for sources of particle scatter such as grain interactions, contact with the substrate, and post-depositional effects. In fact, it is a common observation that DRMs are ~10 times lower the magnetization predicted by the classic model and are highly dependent on the strength of the depositional field (e.g. Johnson et al.,1948; Tauxe and Kent, 1984; Verosub, 1977). Moreover, it has long been recognized that the magnetic inclination recorded by the sediments is shallow with respect to the settling field inclination, an effect known as the inclination error (e.g. Johnson et al., 1948; King, 1955; Griffiths et al., 1960).

King (1955) proposed that the remanent inclination is related to the depositional field by the equation:

$$\tan(I_M) = f * \tan(I_H), \quad (2.2)$$

where I_M is the remanent inclination, I_B is the depositional field inclination, and *f* is a "flattening factor," which describes the amount of shallowing that has occurred, a relationship that has been proven valid to date for natural and redeposited sediments (e.g. Bilardello and Kodama, 2010). This shallowing has been determined to be caused by particle interactions in the water column, rolling and translation of particles on the substrate, and post-depositional rotations (eg. King, 1955; Griffiths et al., 1960; Irving and Major, 1964; Kent, 1973; Verosub, 1977; Tauxe and Kent, 1984; Bilardello, 2013; Bilardello et al., 2013)

Compaction of clay-rich sediments also contributes to inclination shallowing and inefficient DRMs, and is particularly important for deposition experiments that utilize sediments of this grain size. Because of the resultant physical rotation of grains, the remanent intensity and direction is altered, but this probably does not become a factor in natural deposition until ~100 meters below the sediment water interface (Anson and Kodama, 1987; Arason and Levi, 1990). In experimental settings, compaction is simulated when clay-rich sediment is dried through evaporation (e.g. Blow and Hamilton, 1978; this study) or by pressure dewatering (Anson and Kodama, 1987). This mechanism alone results in 10°-15° of inclination shallowing (Kodama and Sun, 1990; Sun and Kodama, 1992).

The classical model of a DRM was impacted by the recognition of the importance of flocculation in many depositional settings (see Roberts et al., 2013). It is rare for isolated particles to settle through a water column without interacting, instead clusters of particles are bound together by van der Waals or electrostatic forces forming larger particles known as flocs or floccules (Stumm and Morgan, 1996). Shcherbakov and Shcherbakova (1983) modeled the behavior of flocs and determined that the flocculation process lowers the efficiency of magnetization and increases the time required to acquire magnetic intensity.

Individual magnetic particles are often captured into flocs with non-magnetic particles, typically larger clay minerals, as they settle in the water column. The resulting floc will contain variably aligned magnetic particles, and thus record a resultant magnetization that can be lower than that of the individual magnetic grains (Katari and Tauxe, 2000). Moreover, these larger flocs are subject to a greater settling velocity (because of their increased size), a greater viscous torque (which increases as the cube of the size of the floc) and variable magnetic torque (depending on the degree of

alignment of the magnetic grains), resulting in a less efficient particle alignment because of increasing time to alignment with the ambient field (Mitra and Tauxe, 2009; Shcherbakov and Sycheva, 2010).

Flocculation occurs in both saline and non-saline environments (eg. Droppo and Ongley, 1994; Katari and Tauxe, 2000). At high salinity or low pH bonding forces between particles are enhanced (Katari and Tauxe, 2000). Droppo and Ongley (1994) found that over 90% of sediment volume transported by six rivers in southeastern Canada was bound in floccules, and that flocculation is controlled by suspended solids concentration, particulate organic carbon concentration, and attached bacteria in non-saline environments.

Recognition of the importance of flocculation in sedimentary magnetizations by Shcherbakov and Shcherbakova (1983) led to several numerical and physical experiments that refined the flocculation model of DRM acquisition (e.g. Van Vreumingen, 1993; Katari and Tauxe, 2000; Tauxe et al., 2006; Heslop 2007; Mitra and Tauxe, 2009; Shcherbakov and Sycheva, 2010). This led to the finding that flocculation results in a non-linear relationship between the remanent intensity of a sediment and the strength of the depositional field (Mitra and Tauxe, 2009). A linear relationship between magnetization acquisition and applied field is one of the fundamental underpinnings of paleointensity estimates in igneous and archeological materials. This phenomenon of non-linear magnetization acquisition in flocculating environments further complicates attempts to derive meaningful information about the depositional field from the remanent intensity of sediments and sedimentary rocks.

Previous studies have determined that the intensity and inclination error of sedimentary remanence depend on both the inclination and intensity of the depositional field (Tauxe and Kent, 1984; Bilardello, 2013, Bilardello et al., 2013). Remanent intensity

decreases with decreasing field strength and increasing depositional inclination (Tauxe and Kent, 1984), and remanent inclination shows the most flattening with decreasing field strengths and mid inclinations - around 60° (Tauxe and Kent, 1984; Bilardello et al., 2013).

Inclination shallowing is negligible at equatorial and polar inclinations, and significant at intermediate latitudes (Tauxe and Kent, 1984). At inclinations near 0°, the magnetic field is aligned with the bedding plane, and so gravitational forces predispose the grains to align efficiently with the ambient field. At inclinations near 90°, the magnetic direction of grains scatters in a roughly equal distribution around the vertical direction, thus maintaining the average orientation but decreasing the length of the resultant vector significantly. The overall result of polar sediment magnetization is a DRM that is highly inefficient in terms of remanent intensity, even though the direction accurately records the depositional field.

The compaction that occurs in clay-rich sediment can also distort the intensity of remanence. Jezek and Gilder (2006) modeled the effects of compaction numerically by rotating aligned grains until the *f*-factor reached a predetermined value. From this model they calculated the resulting intensity and found that in depositional inclinations less than 45° compaction increased the magnitude of the DRM vector while shallowing the inclination. In depositional fields with inclination greater than 45°, the compaction acts to reduce the DRM vector's magnitude (Jezek and Gilder, 2006).

The effect of these biases is to make it challenging to reliably determine the strength and direction of the paleofield as recorded by sedimentary magnetizations. Though techniques have been developed for correcting remanent directions, reliable relative paleointensity estimates are not straightforward to obtain (Jackson et al., 1991; Kim and Kodama, 2004; Kodama, 2009; Roberts et al., 2013).

Jackson et al. (1991) first conceived of a correction for the inclination error based on the anisotropy of anhysteretic remanent magnetization (AARM). This correction is based on the assumption that the orientations of remanence-carrying grains, as reflected by measured AARM, control the direction of a DRM. This is expressed by the equation:

$$DRM = k_D * H \tag{2.3}$$

where *DRM* and *H* are three-component vectors representing the remanence and depositional field of the sediment, respectively, and k_D is a second order tensor representing the anisotropy of the DRM, of the form:

$$\begin{bmatrix} \boldsymbol{k_{xx}} & \boldsymbol{k_{xy}} & \boldsymbol{k_{xz}} \\ \boldsymbol{k_{yx}} & \boldsymbol{k_{yy}} & \boldsymbol{k_{yz}} \\ \boldsymbol{k_{zx}} & \boldsymbol{k_{zy}} & \boldsymbol{k_{zz}} \end{bmatrix}$$

where each row consists of a vector representing an orthogonal axis of the anisotropic DRM ellipsoid. As ARM activates a similar spectrum of coercivities as a DRM, the AARM tensor can be used as an approximation of the DRM tensor (Levi and Banerjee, 1976; McCabe et al., 1985; Jackson et al., 1991).

To best make that approximation, Jackson et al., (1991) used the anisotropy of individual particles to relate the AARM to the anisotropy of a DRM. Defining normalized magnitudes of the AARM principal components q_x, q_y, and q_z, respectively as:

$$q_{(x,y,z)} = ARM_{(x,y,z)} / ARM_{(x+y+z)} \tag{2.4}$$

they express the magnitudes of the diagonal elements of the DRM tensor as:

$$k_{(x,y,z)} = \frac{q_{(x,y,z)} \times (a+2) - 1}{(a-1)} \tag{2.5}$$

with *a* representing the average anisotropy of the individual grains for the bulk sediment.

By left multiplying both sides of the equation ($DRM = k_D * H$) by the inverse of k_D, the DRM vector can be restored to the depositional field. In this scheme the flattening

factor, *f* of King (1955, Equation 2), is related to the AARM tensor elements by the equation:

$$f = \frac{q_z(a+2)-1}{q_x(a+2)-1} \quad (2.6)$$

The DRM correction method as proposed by Jackson et al. (1991) was primarily concerned with inclination shallowing in the plane of the maximum/minimum (X/Z) axes. To allow for correction in the intermediate direction as well, Kim and Kodama (2004) updated the anisotropy correction to allow for rotation in the X/Y plane, and to allow non-zero values in the off-diagonal element of the anisotropy tensor. Both Jackson et al., (1991) and Kim and Kodama (2004) assumed unit length of the DRM vectors.

The inclination correction described above restores the remanent inclinations to those of the depositional field by correcting particle misalignment. In this study we attempt to improve RPI estimates by applying a full-vector anisotropy correction to the remanent magnetization of sediment redeposited in the laboratory. By retaining the full length of the DRM vectors throughout the correction, and not ascribing unit length we test whether restoring the depositional inclination also improves the estimates of the RPI. We present the results of a series of twelve deposition experiments conducted with sediment redeposited under variable field intensities and inclinations. Our experiments isolate and enhance the process of inclination shallowing, imposing consequences on RPI determinations. In turn, we test the efficiency of the anisotropy correction technique to restore the DRM magnitude and evaluate its effect on the RPI.

In the study presented here the assumption is that inclination shallowing can be replicated in the laboratory and will be governed by the same physical laws that govern nature, though at different scales. If, as has been extensively demonstrated, the inclination error can be corrected for (in nature and the laboratory), then the same effects that shallowing corrections have on RPI estimates must also apply to the natural

and the laboratory environment. Thus, our deposition experiments, while not replicating a natural setting, will allow a level of insight into inclination shallowing's effects on sedimentary paleointensity and an increased understanding of processes in nature.

2.2 Materials and Methods

2.2.1 Sediment

Interbedded red clays and tan-yellowish silts of Glacial Lake Duluth affinity were collected near Deer Creek, MN, and were selected for their high concentration of magnetic mineral grains. Glacial Lake Duluth was a pro-glacial lake that last formed at the end of the Lake Superior lobe of the Wisconsin Glacial Episode and covered an area larger than present day Lake Superior (Winchell, 1901). Due to the abundance of iron-oxide bearing minerals in the proximal Mesabi Iron Range (Jirsa et al., 2008), the glacial sediments derived from this area have abundant detrital magnetic minerals.

The silt fraction was first separated from the clays using a small trowel and subsequently disaggregated in water and cleaned of any organic remains. The red clay was then further gravity-separated, by allowing the stirred sediment to settle in a 1L beaker of water (~10 cm height) water for 30 seconds. The fraction of the sediment that was still in suspension after 30 seconds was collected, and the process repeated to insure homogeneity. The resulting fine sediment fraction was collected for use in our experiments.

We measured a grain size frequency distribution of the final sediment separate using a Horiba (Kyoto, Japan) Grain Size Analyzer LA-920 (Jiilavenkatesa et al., 2001; Kirby, 2009) and results are reported (Fig. 2.1a**)**. The distribution shows the sediment grain size ranges from 0.2 to 50 μm, with 90% of the grains below ~12μm in diameter. We observe a population of nano-grains that are smaller than 1 μm, a second population

of clay particles ranging from 1 to 4 μm, and a silt fraction with a distribution that peaks at 5 μm. The smallest grain fraction is interpreted to be the hematite pigment responsible for the red color of the mud.

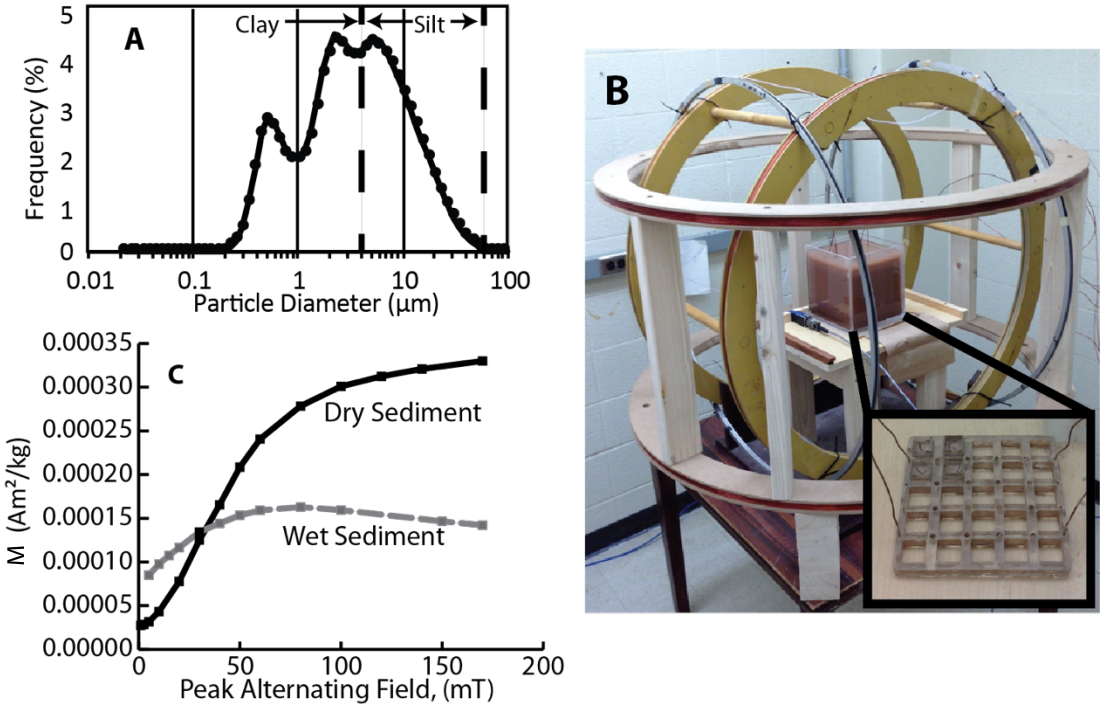

Figure 2.1. Sediment and deposition methods. A) Grain size distribution of the sediment used in our experiments. About 90% of the sediment is smaller than 12μm. B) The Helmholtz coils used. At center is the sediment tank during deposition. The red color of the sediment is due to pigmentary hematite. Inset is the tray that holds sample boxes orthogonal to the depositional field, and four boxes during drying are pictured. C) ARM acquisition of fully dried and damp sediment. The fully dried sediment continues to acquire magnetization with increasing peak AF fields, while the damp sediment declines in J after about 80 mT. This is due to the movement of magnetic grains in high AF fields. Experiments were dried completely in the depositional field before laboratory treatments to avoid this. The dry sediment was given an ARM with a 0.2 mT DC bias field, while the damp sediment was only given a 0.1 mT DC field, explaining the large difference in total remanent intensity.

2.2.2 Deposition procedures

Deposition of disaggregated natural sediments is conducted under controlled magnetic fields using specially constructed Helmholtz coils at the Institute for Rock Magnetism, University of Minnesota (Fig. 2.1b). We used Helmholtz coils of ~1 m diameter, which allow us to precisely control the direction and strength of a depositional

field over a volume of ~15,000 cm^3. We have conducted experiments in 12 ambient fields, at intensities of 25, 50, and 100 μT, with inclinations of 0°, 30°, 60° and 90° for each field intensity. The power supply for the coils is routed through an uninterruptable power supply in order to protect against power outages during deposition.

Prior to deposition, 550 mL of wet sediment is mixed with 450 mL of filtered water, resulting in one liter of slurry. The slurry is first mixed by hand, then placed in an ultra-sonic cleaner for five minutes to ensure complete disaggregation of the particles. After sonication the slurry is poured directly into a deposition tank containing filtered water, with a base area of 17.5 cm^2 and a water depth of 15 cm, positioned within the Helmholtz coils. The tank contains a 5x5 array of 25 sample boxes that have 1.8x1.8 cm bottoms and 1.5 cm depth (internal dimensions) and are held orthogonal to the field declination by a specially constructed plexiglass tray (inset, Fig. 2.1b). The sediment slurry was allowed to settle for approximately 60 hours, ensuring a 25 mm thick sediment cover over the sample boxes.

The ambient field is monitored regularly through deposition and drying using a Fluxgate Magnetometer placed next to the tank (Fig. 2.1b). After 60 hours of settling time, the sample tray is removed from the tank and the sediment is allowed to dry out completely in the applied field (approximately 72-96 hours dependent on ambient humidity). Experiments were repeated if their NRM had an erroneous declination, since no process in our experiments should cause variation in the Y direction, or if the estimated paleointensity was far different than would be expected from comparison with other experiments. Some repeat experiments confirmed the initial results, but if the repeat experiment brought an improvement, then those results were used.

2.2.3 Magnetic measurements

All magnetic measurements were conducted at the University of Minnesota Institute for Rock Magnetism in Minneapolis, Minnesota.

Sediment characterization

The magnetic properties of the sediment employed for the deposition experiments were measured to ensure its suitability for use in deposition experiments. Hysteresis loops, backfield demagnetizaiton curves, and first order reversal curves (FORC) were measured on a vibrating sample magnetometer (VSM, model 3900 "MicroMag", Princeton Measurements, Princeton, NJ) using maximum fields of 1.5 T. Backfield curves are used to unmix the coercivity spectra using the MaxUnmix software of Maxbauer et al., (2016). FORC data were processed with the FORCinel software package (Harrison and Feinberg, 2008), along with the VARIFORC module of Egli (2013).

Low temperature magnetic responses between 300 K and 20 K were measured on a Quantum Design (San Diego, Ca) Magnetic Properties Measurement System. We performed field cooled (FC) measurements by applying a 2.5 T field as the specimen cools from room temperature (300 K) to 20 K, and measuring the remanence upon warming. We also measured zero field cooled (ZFC) curves by cooling the specimen to 20 K in zero-field, applying a low-temperature SIRM of 2.5 T, and measuring the remanence upon warming. We then measured room temperature saturation isothermal remanent magnetization (RTSIRM) curves, by applying a 2.5 T field at room temperature and then measuring the remanence upon cooling to 20 K and warming back to 300 K.

Experimental measurements

The anisotropy of magnetic susceptibility (AMS) of all redeposited specimens was measured on an AGICO MFK1-FA with a three axis sample rotator, operating at 200 A/m field intensity and 976 Hz frequency. A subset of at least four specimens per experiment are used for a pseudo-Thellier experiment (Tauxe et al., 1995): AF demagnetization of the NRM and subsequent ARM acquisition are performed and measured on a 2G DC SQUID U-Channel magnetometer and degaussing subsystem. Demagnetization is done progressively in AF beginning at 5 mT, up to 170 mT. Progressive ARM application is conducted on a 2G ARM magnetizer Model 615, with a peak field of 170 mT and a DC bias field of 0.2 mT. This step ensures verifying that the sediment is completely dry and that high fields will not cause the grains to rotate (Figure 2.1c).

Anisotropy of anhysteretic remanent magnetization (AARM) was measured using the 9 position scheme of Girdler (1961). For this process, all specimens are demagnetized and magnetized in a Precision Instruments DTech D-2000 AF demagnetizer. First, a background measurement is taken in the 2G DC SQUID U-Channel magnetometer after a 200 mT maximum field demagnetization along the three primary axes (X, Y, Z). Then ARMs are applied to each of the 9 directions using a maximum AF of 150 mT with a DC bias field of 0.2 mT. After each measurement the previous ARM is removed using 200 mT AF demagnetizing fields.

Saturating magnetizations used for RPI normalization are applied using both anhysteretic remanent magnetizations, which best represent the spectrum of coercivity that records a DRM, and isothermal remanent magnetizations (Levi and Banerjee, 1976; McCabe et al., 1985; Jackson et al., 1991). ARMs are applied in 200 mT AF in the presence of a 0.2 mT DC bias field using our DTech AF (de)magnetizer. Saturation

isothermal remanent magnetizations of 200 mT are applied in a 2G model 670 long-core impulse remanent magnetizer. The saturation magnetizations are measured in the 2G DC SQUID U-Channel magnetometer.

2.3 Results

2.3.1 Sediment characteristics

Hysteresis loops show a combination of paramagnetic and ferromagnetic response. After paramagnetic slope correction the saturation magnetization (M_s) is of the order of ~ 6 x 10^{-2} Am^2/kg, saturation remanence magnetization (M_{rs}) of ~1 x 10^{-2} Am^2/kg, and coercive force (H_c) of ~21 mT (Fig. 2.2a). Hysteresis loops are also somewhat constricted, indicating the presence of different coercivities, which we attribute to magnetite and pigmentary hematite. IRM backfield curves shows remanent coercivity (H_{cr}) of ~56 mT (Fig. 2.2b). On a Day plot (Day et al., 1977), hysteresis parameters plot in the pseudo-single domain (PSD) state, slightly off of Dunlop's (2002) SD-MD theoretical mixing curves for titanomagnetite (Fig. 2.2c). We attribute the offset to the presence of pigmentary hematite in our sediment, which increases the H_{cr}/H_c ratio.

Unmixing of the coercivity distribution was conducted using the software MaxUnmix (Maxbauer et al., 2016). We interpret 3 populations of magnetic minerals (Fig. 2.2d). The lowest coercivity population, with a mean coercivity of ~10 mT, is interpreted to be multi-domain magnetite. The primary population has a mean coercivity of ~60 mT which we interpret as fine grained high coercivity magnetite. The third population has a mean coercivity of ~600 mT, and we interpret this to indicate pigmentary hematite. These data are in agreement with the hysteresis parameters, indicating a mixture of MD magnetite, fine grained magnetite and pigmentary hematite that plots within the PSD field of the Day et al., (1977) diagram above the SD-MD magnetite mixing curve.

Analysis of the FORC diagram confirms a dominance of PSD grains (Fig. 2.2e). The dominant distribution is concentrated at coercivities <100 mT with little dispersion along the H_u axis (+/- 30 mT), with a poorly defined "ridge" along the horizontal H_c axis that is prominent to ~300 mT but persists up to ~600 mT within 95% confidence bounds. We interpret these data as a dominant magnetite population with accessory hematite. The dispersion along the H_u axis is consistent with the low coercivity component modeled from the unmixing of the backfield curves and is interpreted as minor MD magnetite. The dominant magnetite population, however, is of higher coercivity, with a modeled peak at ~60 mT, consistent with PSD and possibly minor SD grains, in full agreement with the modeling of the coercivity spectra. The dominant magnetite distribution is thus within the ideal remanence carrier grain size range. The hematite pigment, although abundant, contributes negligibly to the total remanence.

The field-cooled and zero-field-cooled remanences measured upon warming show a magnetite Verwey transition at about 115 K. The field-cooled remanence possesses higher magnetization than the zero-field-cooled experiment**,** suggesting that magnetite is present in single domain (SD) or pseudo-single domain (PSD) state (Fig. 2.2f). The room temperature saturation isothermal remanent magnetization (RTSIRM) measurements measured upon cooling and heating display a broader, but still evident, Verwey transition. The full RTSIRM is not fully recovered after temperature cycling, suggesting demagnetization of PSD and/or the presence of multi domain (MD) grains.

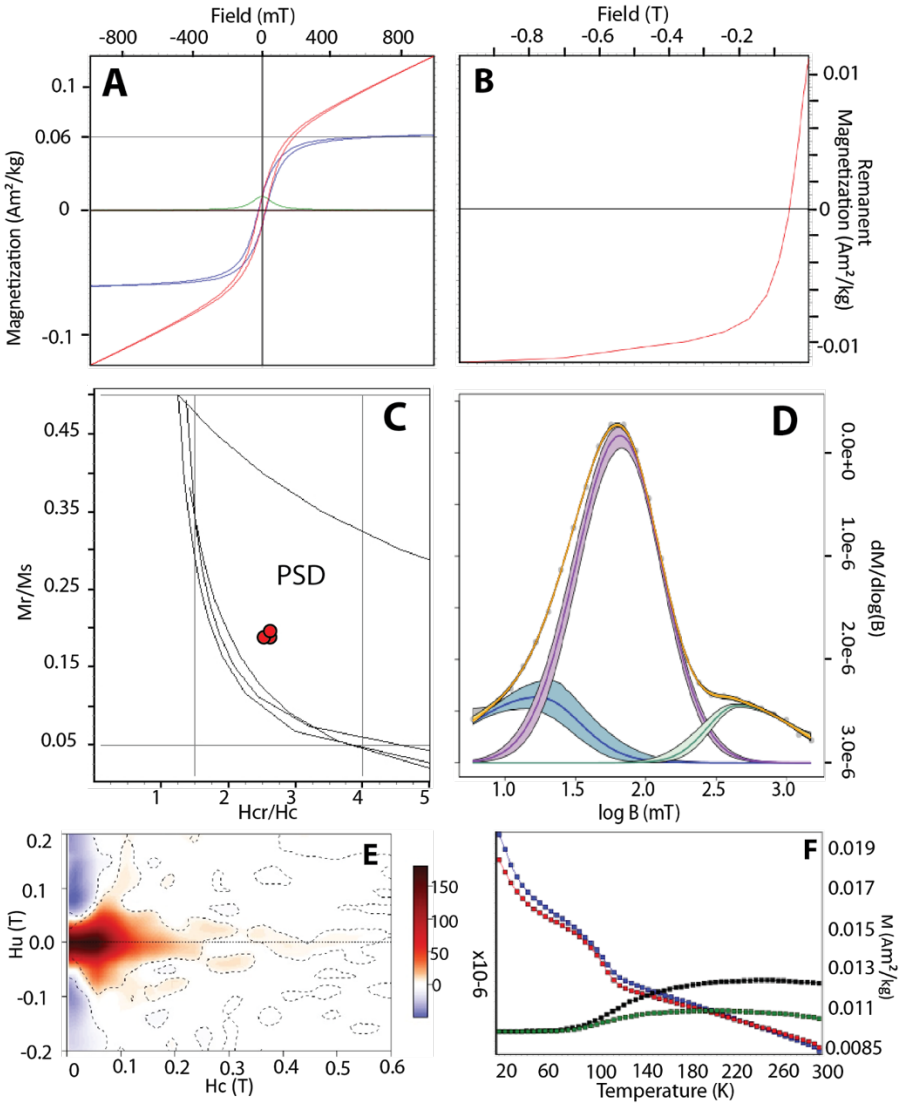

Figure 2.2. Magnetic characteristics of the sediment. **(A)** Hysteresis loops with the paramagnetic component (red) and with that component removed (blue). **(B)** IRM Backfield curve. Failure to fully saturate is likely due to the pigmentary hematite, which is not an important contributer to remanence. **(C)** Day et al., (1977) plot with the theoretical titanomagnetite mixing curves of Dunlop (2002). The sediment plots in the pseudo-single domain range, and is pulled off the mixing lines by the presence of pigmentary hematite. **(D)** Unmixed coercivity distribution using MaxUnmix (Maxbauer et al., 2016). There are three distinct populations corresoponding to MD magnetite (blue), PSD magnetite (purple), and pigmentary hematite (green), in order of increasing coercivity. **(E)** First order reversal curve processed using the FORCinel software package (Harrison and Feinberg, 2008), along with the VARIFORC module of Egli (2013) with a smoothing factor of 4. There is little dispersion along the H_u axis and a poorly defined ridge along the H_c axis, consistent with an interpretation of dominant PSD magnetite with accessory populations of MD magnetite and pigmentary hematite. **(F)** Low temperature measurements. Field-cooled (blue) and zero-field-cooled (red) remanence upon warming. RTSIRM upon cooling (black) and warming (green).

2.3.2 Magnetic remanence

Remanent directions

For each experiment, mean uncorrected remanent vectors, their Fisher (1953) statistics, and the *f*-factor of King (1955) are reported in Table 1.

Table 1. Uncorrected Remanence

Depositional conditions		Fisher (1953) Means								
Intensity (μT)	Inclination (°)	Declination (°)	Inclination (°)	Number of Specimens	Resultant Vector	Dispersion (Precision Parameter (k))	α_{95} (°)	Circular Standard Deviation	*f* Factor King (1955)	Remanent Magnetization Am^2/kg
25	0	179.5	1.9	25	24.9737	912.6	0.9	2.7	-	1.13E-03
25	30	180.9	7.2	25	24.9642	671.2	1.1	3.1	0.218	6.10E-04
25	60	179.9	15.8	25	24.9275	330.8	1.5	4.5	0.163	6.16E-04
25	90	173.7	65.1	25	24.5192	49.9	4.0	11.5	0.722	1.88E-04
50	0	178.1	-0.7	25	24.9830	1415.0	0.7	2.2	-	1.23E-03
50	30	177.6	6.3	25	24.9781	1096.7	0.8	2.4	0.191	9.55E-04
50	60	180.0	20.9	25	24.9664	714.2	1.0	3.0	0.221	6.92E-04
50	90	176.6	79.0	25	24.6689	72.5	3.3	9.5	0.878	3.92E-04
100	0	178.0	-1.4	25	24.9827	1385.3	0.8	2.2	-	1.59E-03
100	30	178.4	8.2	25	24.9801	1208.5	0.8	2.3	0.279	1.48E-03
100	60	175.0	22.5	25	24.9390	393.5	1.4	4.1	0.239	9.56E-04
100	90	191.9	81.0	25	24.6033	60.5	3.6	10.4	0.9	5.93E-04

We observe considerable inclination shallowing at depositional field inclinations of 30° and 60° (Fig. 2.3). At field inclinations of 0° the magnetic field is aligned with the bedding plane, causing a more efficient particle alignment than at other depositional fields, and no resulting inclination shallowing. At a 90° depositional inclination, perpendicular to the bedding plane, DRMs are not an efficient magnetization process. Particle scatter, however, is evenly distributed around the vertical azimuth, resulting in minimal total shallowing in vertical fields with the exception of the weaker 25 μT field strength.

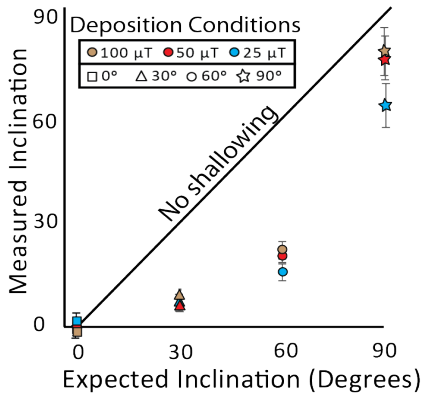

Figure 2.3. Inclination shallowing as represented by comparing measured with expected inclination. Error is 1σ of the 25 specimens of each experiment.

As expected, no inclination shallowing is observed at 0° whereas moderate shallowing is observed at depositional field inclinations of 90°. We observe the most shallowing as a percentage of the depositional field inclination at 30°, with 70 – 79% shallowing, than there is at 60° where it reaches 62 - 74%. At a 90° field inclination there is 10 – 13% shallowing at intensities of 100 and 50 μT, however, for the weaker field strength of 25 μT we observe 27% of inclination shallowing. The average flattening factor, *f* of King (1955, Equation 2), for 30° and 60° settling field inclinations for all experimental intensities is 0.22 (standard deviation = 0.04).

The inclination error increases with decreasing depositional field strength with the least amount of shallowing observed in the strongest field intensity of 100 μT and the most error observed at 25 μT, as observed by previous studies (e.g. Tauxe and Kent, 1984; Bilardello et al., 2013; Bilardello, 2013). The only exception to this pattern, however, occurs for the depositional fields of 25 and 50 μT at 30° field inclination where the degree of shallowing for both experiments is within one standard deviation.

The observed dependence of the inclination error on field strength is further supported by the Fisher (1953) statistics (Table 1): The largest resultant vector magnitudes occur in horizontal fields, and the smallest in vertical inclinations, indicating more tightly grouped directions, and the precision parameter (*k*), also a measure of the estimated dispersion of directions, decreases with increasing inclination. A high precision parameter indicates that the dispersion of directions is more closely concentrated around the estimated true mean than at a lower value of *k*. All experiments show highly reproducible results with 95% confidence circles varying between 0.7° and 4° over the different field intensities. The α_{95} confidence intervals and the circular

standard deviation increase with increasing inclination in all experimental intensities, indicating increased particle dispersion.

Where the Fisher (1953) statistics indicate better alignment of remanent magnetizations of the specimens within an experiment, we also observe higher remanent intensities, indicating improved particle alignment (i.e. decreased scatter) in field with stronger remanent magnetizations, and that the efficiency of alignment depends on the depositional inclination.

Shape Analysis of the DRM vector distribution

Analysis of the shape of the distribution of remanent directions can be useful in the correction of DRM shallowing in paleomagnetic studies (Tauxe and Kent, 2004; Bilardello et al., 2011). An east-west elongation of remanent directions is often indicative of inclination shallowing (Tauxe and Kent, 2004). To analyze the shape of the distribution, Table 2 reports a principal component analysis of the remanent vectors calculated using the goprinc.py function of the PmagPy software package (Tauxe et al., 2016). The maximum eigenvalue corresponds to a vector that is aligned with the direction of the DRM, and by studying the relationship between the intermediate and minimum eigenvalues and vectors it is possible to gain insights into the shape of the distribution in a quantitative manner.

Table 2. Uncorrected Distributions
Principal Component Analysis - go_princ.py of the PmagPy software (Tauxe et al., 2016)

Depositional Conditions											
Intensity (μT)	Inclination (°)	Max (τ1)	Declination	Inclination	Int (τ2)	Declination	Inclination	Min (τ3)	Declination	Inclination	Circularity τ2/τ3
25	0	0.9979	179.5	1.9	0.0016	276.1	74	0.0005	88.9	15.9	3.2
25	30	0.99714	180.9	7.2	0.00223	69.9	70.7	0.00063	273.3	17.8	3.5
25	60	0.99422	179.9	15.8	0.00396	273.9	13.9	0.00183	43.4	68.7	2.2
25	90	0.96208	173.6	65.2	0.02893	63.6	9	0.00898	329.8	22.9	3.2
50	0	0.99864	358.1	0.7	0.00116	241.1	88.5	0.00019	88.1	1.3	6.1
50	30	0.99825	177.6	6.3	0.00131	301.8	78.9	0.00044	86.6	9.1	3.0
50	60	0.99732	180	20.9	0.00158	71.5	39.7	0.00111	290.9	43	1.4
50	90	0.97387	176.6	79	0.01458	321.5	9	0.01155	52.4	6.2	1.3
100	0	0.99862	358	1.4	0.00122	112	86.5	0.00016	268	3.2	7.6
100	30	0.99841	178.4	8.2	0.00117	295.6	72.5	0.00042	86.1	15.4	2.8
100	60	0.99513	175	22.5	0.00271	279.6	31.2	0.00216	55.6	49.9	1.3
100	90	0.96912	191.1	81	0.01889	85.9	2.4	0.01199	355.5	8.6	1.6

The ratio of the intermediate to minimum eigenvalues (τ_2 and τ_3, respectively) can be used as a measure of circularity - if the ratio is close to 1, the distribution is circular; if it is larger, it is more elongate.

In depositional field intensities of 100 and 50 $\boldsymbol{\mu}$T, experiments at field inclinations of 90° and 60° show a near-circular distribution with τ_2/τ_3 ratios of 1.3 to 1.6. Experiments in a field inclination of 30° are elongate at a ratio of about 3, and in horizontal fields the ratio is greater than 6 (Table 2). As will be shown below, however, the high ratio of intermediate over minimum eigenvalues for the horizontal field-data is mediated by a high maximum eigenvalue, indicating that these data are in fact strongly clustered. Experiments conducted in a field intensity of 25 $\boldsymbol{\mu}$T show a ratio between 2.2 and 3.5, independent of field inclination. The lack of a discernable trend in the experiments conducted in the weakest field may point to an inefficient DRM acquisition in low intensities, independent of the inclination. The direction of the elongation of the distribution, as determined by the direction of the eigenvector corresponding to the intermediate eigenvalue, ranges from horizontal in the E-W direction (vertical fields) to near vertical (horizontal fields, Fig. 2.4). This fits the model of Bilardello (2013) of 4 particles that are magnetically oriented horizontally or vertically rotating about a horizontal axis in each of the cardinal directions.

A quantification of the shape of a distribution of vectors was proposed by Woodcock (1977), and determines a shape parameter (γ) that ranges from clustered to girdled, and a strength parameter (ζ) of that shape. Figure 2.5 shows that the vector distributions of our experiments are clustered, with γ <5 for most experiments. Experiments tend to group on the Woodcock (1977) diagram based on their deposition inclination - the loosest clustering of the distribution, in terms of the strength parameter, ζ, is observed in experiments conducted with a 90° depositional inclination,

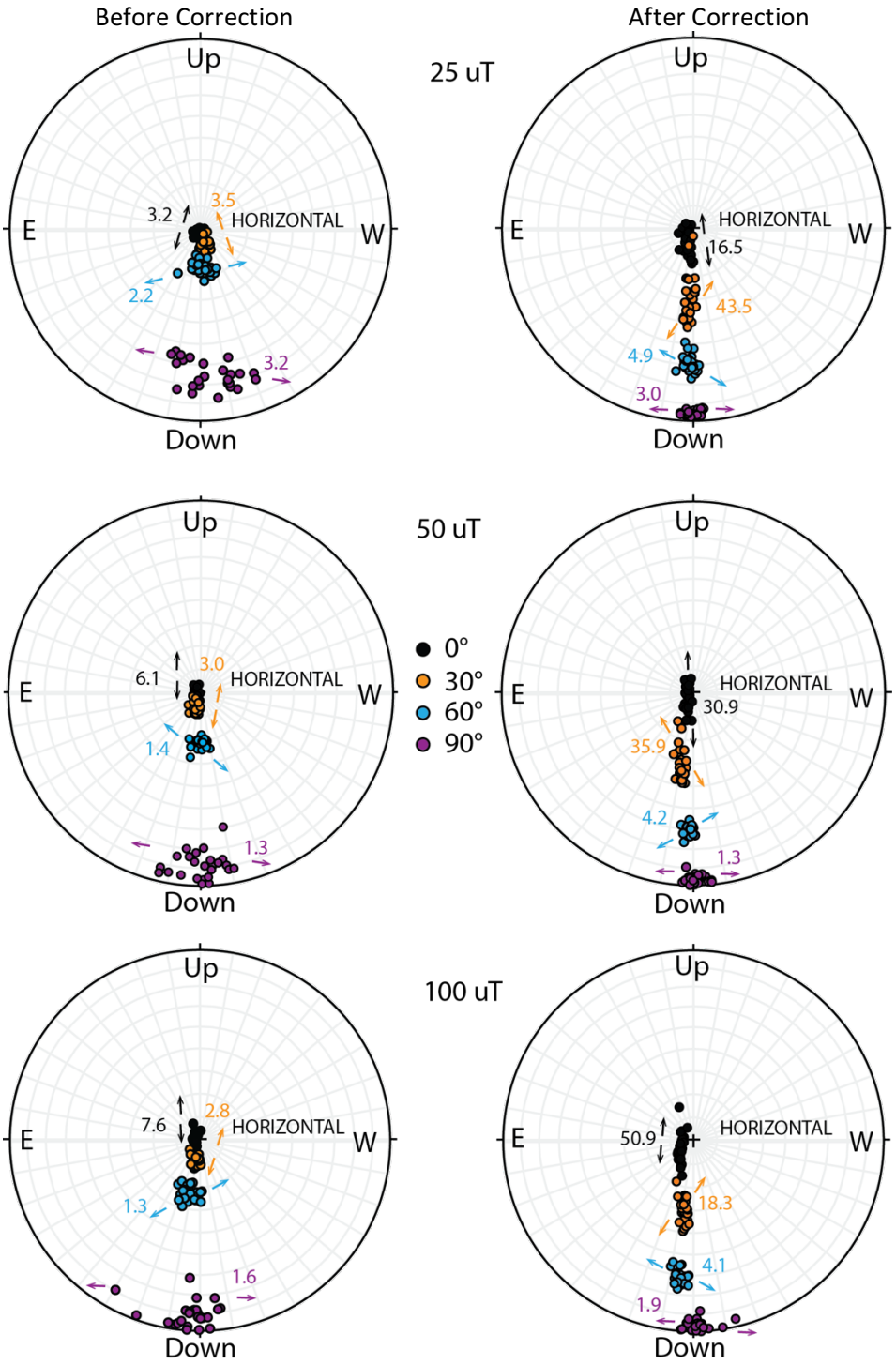

Figure 2.4. Remanent vectors distributions, uncorrected (left) and corrected (right). Stereonets are oriented so that the view is south and horizontal. Arrows correspond to the direction of elongation, which is oblique to the stereonet view in some cases (especially for the corrected distributions of intermediate inclinations). The number next to the arrows is the circularity of the distribution ($\tau 2/\tau 3$). The distributions are elongate vertically in horizontal depositional fields, and horizontally in vertical fields, with elongation generally increasing with decreasing inclination.

while the tightest clustering of the distributions occurs in horizontal depositional fields. Overall, in experiments conducted in the same field intensities, the strength parameter decreases and the shape parameter increases with increasing field inclination. For example, the remanent magnetic directions of sediment deposited in a vertical field is more circular (smaller τ_2/τ_3), and less strongly clustered than sediment deposited in a horizontal field (larger τ_2/τ_3). This observation further confirms that particle scatter increases with inclination in our experiments.

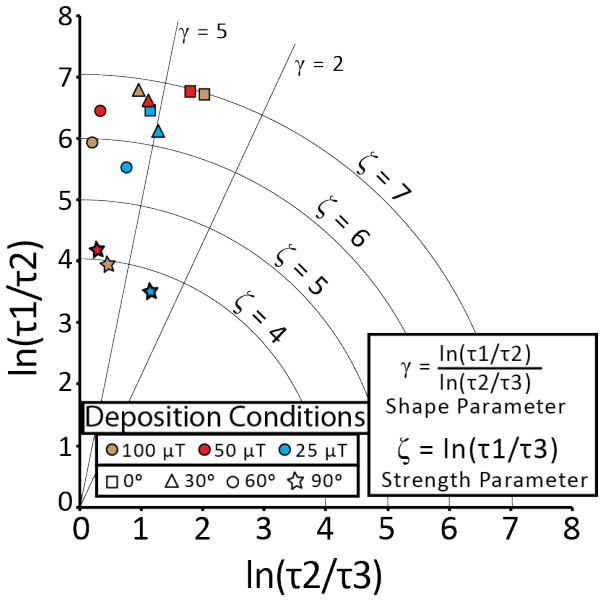

Figure 2.5. Woodcock (1977) shape analysis of the uncorrected NRM vector distribution. As γ increases the distribution become more clustered or circular, and less girdled (elongate). As ζ increases, the tightness of clustering or girdling increases. Our experiments are all clustered ($\gamma > 1$), with the strongest clustering in horizontal fields and the weakest in vertical fields.

Remanent intensities and uncorrected RPI

We find that the intensity of remanence depends on both the inclination and intensity of the depositional field. With increasing depositional inclination, we observe a decreasing remanent intensity (Fig. 2.6a). However, in the 25 μT experiment series this trend is somewhat disrupted, and the 30° and 60° inclinations have remanent intensities

that are within one standard deviation of each other. Additionally, with decreasing depositional field strengths there is decreasing remanent intensity. This trend is evident for each depositional field inclination. All these observations are consistent with previously published results (e.g. Tauxe and Kent, 1984; Jezek and Gilder, 2006; Bilardello et al., 2013; Bilardello, 2013).

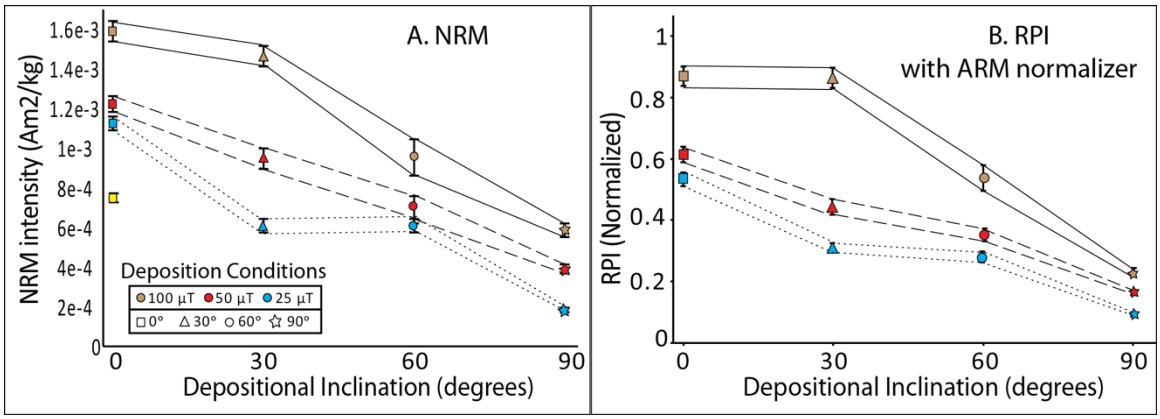

Figure 2.6. Uncorrected NRMs (A) and RPI estimates (B). Both show decreasing intensity with increasing inclination, showing the intensity's dependence upon inclination – the effect we attempt to remove with the anisotropy correction. A single experiment was conducted in a depositional field of 12.5 μT and 0 degree inclination (Yellow square); it highlights the non-linearity of the remanent intensity's dependence on depositional intensity. Error envelopes are 1σ of the 25 specimens in each experiment.

To calculate relative paleointensity estimates, remanent intensities are normalized with an anhysteretic remanent magnetization with a maximum alternating field of 200 mT and a DC bias field of 0.2 mT applied along the +X specimen axis. The uncertainty of the RPI estimates is determined as one standard deviation of the 25 specimen determinations for each experiment run. The RPI estimates reflect the same trends as the raw intensities, where the remanent intensity decreases with increasing depositional inclination and decreasing field strength (Fig. 2.6b). This negative correlation between intensity and field inclination hinders the validity of making direct comparisons between sediments deposited under different field inclinations, or for natural sediments, at different latitudes.

Furthermore, the non-linear relationship between depositional and remanent intensity complicates interpretations. Though there is a clear dependence of remanent intensity on the depositional field, this dependence is non-linear. For example, in the 0° experiments for depositional fields strengths of 100, 50, 25, and 12.5 μT, remanent intensities do not decrease by the same proportions. This non-linearity undermines a fundamental underpinning of relative paleointensity estimates (Roberts et al., 2013).

To make RPI estimates more useful for stratigraphic, chronometric, geodynamic, and other applications, sediment deposited in a given field strength should be able to allow determination of a consistent relative intensity, regardless of the depositional inclination. We test whether a correction technique for our laboratory deposited sediments can restore the non-linearity and variations observed between the remanent intensity and the field inclination.

Modeling the tensorial nature of DRM acquisition

To evaluate the tensorial relationship between the DRM vector and that of the depositional magnetic field, we fit our magnetization and inclination data with 2-dimensional model of the vertical and horizontal components of a DRM tensor (Fig. 2.7). The main goal of this study is to attempt to use the AARM tensor to approximate that of the DRM, and use it to restore the depositional field; by modeling the tensor fit of the data, we are able to confirm if this approach is valid. Error for the horizontal and vertical components of the data is determined as one standard deviation of the 25 specimens. The 50 μT and 100 μT field intensity experiments' data fits the modeled relationship well, with the best fit in the strongest field. For the 25 μT field intensity experiment series, the horizontal component of the model does not fit within the error of the data. Thus, with the exception of the horizontal component of the 25 μT depositional intensity

experiments, the data fit the modeled 2-D tensors. The decay of the model's fit with decreasing depositional intensity suggests that weaker fields are less efficient at aligning detrital particles. This increases particle scatter in the sediment and weakens the tensorial relationship.

The ratio of the vertical and horizontal components of each intensity, as calculated from the model in a manner similar to Tauxe and Kent (1984) ($R = k_{zz}/k_{hh}$, where the k_{zz} and k_{hh} are the diagonal elements of the 2-D modeled tensor), are lower than the average f-factors derived with Equation 2 (Table 1). According to Tauxe and Kent (1984), this confirms that particle misalignment is not due solely to rolling spheres (in which case R = 1), and that the proportion of plates and spheres in the magnetic mineralogy controls inclination shallowing as long as R is close to *f*. However, the supposition that R should equal *f* under the 'plates and spheres' model is not necessarily true. As R is the ratio of intensities of sediment deposited in vertical and horizontal fields, and *f* is the ratio of measured and depositional inclinations, they represent fundamentally different properties, and should not be expected to be equal.

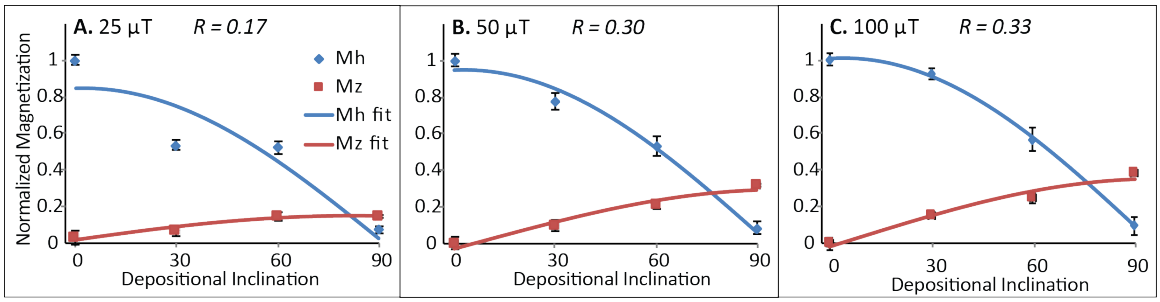

Figure 2.7. Modeling the tensorial nature of DRM acquisition. In the 100 μT experiment series the data are within error of the model for all cases. In the 50 μT experiment series the fit is good, but the modeled 0 and 30 inclination horizontal components are outside of 1σ of the data. The model does not fit the data for the 25 μT series. This decreasing fit with decreasing depositional intensity is due to the inefficiency of weaker fields to align detrital particles. Error is 1σ for each component of each specimen in an experiment.

2.3.3 Anisotropy of anhysteretic remanent magnetization

Measurements of the anisotropy of anhysteretic remanent magnetization (AARM) show a typical sedimentary fabric (e.g. Tarling and Hrouda, 1993). The shape of the

AARM ellipsoids for all experiments, as shown on a Jelinek (1981) plot, is oblate (0.51 > T > 0.76) and the degree of anisotropy (Pj) is between 1.23 and 1.32 (Fig. 2.8). Experiments conducted at 90° have the lowest degree of anisotropy, corresponding to the more evenly distributed particle scatter that occurs in a vertical field. By definition of their oblate shape, all experiments have a stronger foliation than lineation, with a typical average lineation for an experiment being ~1.05, and a foliation of ~1.2.

The maximum and intermediate axes of the AARMs are contained within the bedding plane, and the minimum axes are vertical, perpendicular to bedding, as is expected for a sedimentary magnetization (Table 3, Tarling and Hrouda, 1993). The maximum and intermediate axes are generally clustered, with the maximum axes typically showing a north-northeast orientation and the intermediate axes having a west-northwest orientation.

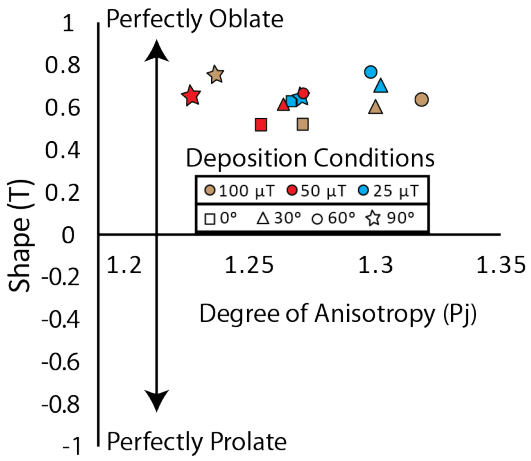

Figure 2.8. Jelinek (1981) plot of average AARM fabrics for each experiment. All fabrics are oblate with a shape parameter (T) between 0.51 and 0.76. The degree of anisotropy (Pj) ranges from 1.23 and 1.32.

2.4 Correction and Discussion

2.4.1 The anisotropy correction process

Corrections of DRM vector inclinations are carried out using the procedure of Kim and Kodama (2004) and modified by the authors to also correct for the magnitude. We

use the measured individual specimen DRM vectors, normalized by the specimen mass, corrected by the mean AARM anisotropy eigenvalues and eigenvectors for each experiment. To obtain the average anisotropy, we remove any individual specimens that have obvious outlying axial orientations or shape and compute the mean eigenvalues and eigenvectors from the AARM tensor elements of the selected data (Table 3).

Table 3. Anisotropy of Anhysteretic Remanent Magnetization
Eigenvalues and eigenvectors of the anisotropy tensor calculated with s_eigs.py of PmagPy (Tauxe et al., 2016)

Depositional Conditions											
Intensity (μT)	Inclination (°)	Min (K_{zz})	Declination	Inclination	Int (K_{yy})	Declination	Inclination	Max (K_{xx})	Declination	Inclination	Number of Specimens
25	0	0.290	109.3	88.5	0.347	282.8	1.5	0.362	12.8	0.2	25
25	30	0.285	111.6	89.2	0.351	287.6	0.8	0.364	17.6	0.1	25
25	60	0.285	146.6	88.6	0.353	283.1	1.0	0.362	13.1	1.0	25
25	90	0.290	124.3	89.1	0.349	288.0	0.8	0.361	18.0	0.2	25
50	0	0.291	124.8	88.2	0.343	281.8	1.7	0.366	11.8	0.7	24
50	30	0.291	134.5	87.7	0.348	284.7	2.0	0.361	14.7	1.2	24
50	60	0.290	148.2	88.8	0.350	288.0	0.9	0.361	18.0	0.8	25
50	90	0.296	84.0	88.3	0.347	286.1	1.6	0.357	196.1	0.7	25
100	0	0.290	151.4	85.9	0.345	284.3	2.8	0.364	14.4	3.0	25
100	30	0.286	161.8	88.3	0.348	282.5	0.9	0.366	12.5	1.5	25
100	60	0.283	90.6	88.6	0.350	286.0	1.4	0.366	196.0	0.4	25
100	90	0.294	75.0	88.8	0.349	281.6	1.1	0.357	191.6	0.5	24

To restore the depositional field, we iterate the correction using different *a*-values until we reproduce the known depositional field inclination. We assume that the *a*-value that produces the correct depositional field inclination also correctly restores the magnitude of the DRM vectors, and we use this corrected magnitude to compute the corrected RPIs. Throughout all the experimental field conditions we observe an average individual particle anisotropy of 1.82 (standard deviation= 0.1). The *a*-value ranges from 1.65 to 2 across experiments of varying depositional field intensity and inclination (Table 4), however, since it represents the average anisotropy of individual grains and since we reuse the same sediment in every experiment, it should remain a constant material property (Jackson et al., 1991). We attribute the variation observed to changes in degree of flocculation as the particles interact in the water column. Entrapment of magnetic grains in flocs causes differences in grain alignment, in turn affecting the bulk anisotropy of a floc (e.g. Katari and Tauxe, 2000; Mitra and Tauxe, 2009; Shcherbackov and

Sycheva, 2010). Flocculation is expected to occur in our experiments due to the high concentration of sediment in the water column (Droppo and Ongley, 1994).

On top of the deflection of DRMs by the anisotropy of the particles, the bulk anisotropy of the specimens will also deflect laboratory fields such as the normalizing ARMs, further affecting the RPI estimates. To obviate this effect, we use the AARM fabric to apply a correction to the saturation ARM fields (e.g. Selkin et al., 2000) and we use the corrected ARMs to normalize the corrected DRM vectors.

2.4.2 Corrected DRM vectors

The anisotropy-based correction restores the inclination, but does not always improve the Fisher (1953) statistics for all experiments (Table 4). In all depositional field intensities, the precision parameter decreases, the α_{95} increases, and the circular standard deviation increases for field inclinations of 0° and 30° after the correction. Those parameters do not vary before and after the correction for 60° depositional inclinations, and are improved in 90° fields.

Table 4. Corrected Remanence

Depositional Conditions		Fisher Means								
Intensity (μT)	Inclination (°)	Declination (°)	Inclination (°)	Number of Specimens	Resultant Vector	Dispersion (Precision Parameter (k))	α_{95} (°)	Circular Standard Deviation	a-value used	Remanent Magnetization Am^2/kg
25	0	177.4	6.0	25	24.8545	164.9	2.2	6.3	2	2.57E-03
25	30	178.4	30.1	25	24.6447	67.5	3.4	9.9	1.79	1.51E-03
25	60	177.4	59.6	25	24.9234	313.5	1.6	4.6	1.71	2.54E-03
25	90	177.0	85.3	25	24.9734	901.0	0.9	2.7	1.65	1.84E-03
50	0	177.6	1.7	25	24.9000	239.9	1.8	5.2	2	2.79E-03
50	30	174.1	30.1	25	24.8037	122.3	2.5	7.3	1.68	2.36E-03
50	60	177.0	59.9	25	24.9726	876.8	0.9	2.7	1.71	2.82E-03
50	90	190.2	86.4	25	24.9594	590.9	1.2	3.3	1.7	2.78E-03
100	0	174.7	3.0	25	24.8557	166.3	2.2	6.3	1.9	3.51E-03
100	30	175.6	30.1	25	24.8936	225.5	1.9	5.4	1.92	3.69E-03
100	60	169.9	60.2	25	24.9447	434.1	1.3	3.9	1.86	3.82E-03
100	90	202.6	86.2	25	24.9280	333.3	1.5	4.4	1.9	3.56E-03

Experiments conducted in vertical fields exhibit the most statistical dispersion before correction, and this scatter becomes reduced after correction, effectively improving statistical measures of alignment. However, the correction does not improve alignment in depositional fields that produce less initial scatter than the vertical inclination (e.g. depositional fields <45°). Horizontal and intermediate depositional

inclinations are highly clustered from the outset, which does not allow the correction to increase clustering of the distribution, and instead increases elongation in the vertical direction (Figs. 2.4, 2.5). The near-constant conditions of our experiments yield highly clustered distributions, but rolling and flattening of detrital magnetic particles of various morphologies leads to higher dispersion in the horizontal plane for vertical depositional fields and increased elongation in the vertical plane for shallower depositional field inclinations. It is important to note that these elongate distributions are not well described by Fisher (1953) statistics, which work best for circular dispersions of directions.

Shape analysis of the corrected distributions

The shape of the distribution of DRM vectors changes to become more elongate after the correction in all cases except the experiments deposited with 90° inclinations, which remain unchanged or become more circular (Table 5). The elongation of the distribution also tightens in the E-W plane, but the same pattern of vertical elongation in horizontal fields, and slight horizontal elongation in vertical depositional fields with intermediate elongations in intermediate fields still remains (Fig. 2.4).

Table 5. Corrected Distributions

Depositional Conditions		Principal Component Analysis - go_princ.py of the PmagPy software (Tauxe et al., 2016)									
Intensity (μT)	Inclination (°)	Max (τ1)	Declination	Inclination	Int (τ2)	Declination	Inclination	Min (τ3)	Declination	Inclination	Circularity τ2/τ3
25	0	0.98844	177.4	6	0.0109	324	82.9	0.00066	87	3.9	16.5
25	30	0.97242	178.4	30.2	0.02696	6.2	59.5	0.00062	270.4	3.4	43.5
25	60	0.9939	177.4	59.6	0.00506	351	30.2	0.00104	82.6	2.8	4.9
25	90	0.99787	177	85.3	0.0016	65	1.8	0.00053	334.8	4.4	3.0
50	0	0.99203	177.6	1.7	0.00773	3.7	88.3	0.00025	267.6	0.2	30.9
50	30	0.98449	174.1	30.2	0.01509	353	59.8	0.00042	83.8	0.5	35.9
50	60	0.99781	177	59.9	0.00176	1.9	30	0.00042	270.6	2.1	4.2
50	90	0.99676	190.2	86.4	0.00182	296.4	1	0.00143	26.5	3.5	1.3
100	0	0.98858	174.7	3	0.0112	30.7	86.3	0.00022	264.8	2.2	50.9
100	30	0.99154	175.6	30.1	0.00803	346.8	59.6	0.00044	83.4	3.9	18.3
100	60	0.99559	169.9	60.2	0.00355	344.6	29.6	0.00086	75.9	2.3	4.1
100	90	0.99427	202.5	86.2	0.00373	89.7	1.5	0.002	359.6	3.5	1.9

The Woodcock (1977) diagram of the corrected distributions shows more girdling than before the correction is applied, except for experiments conducted in 90° inclinations (Fig. 2.9). Whereas before the corrected almost all of the experiments fell above a shape parameter of 5, only the 90° inclinations experiment do so after.

Additionally, the pre-correction trend of increasing strength parameter with decreasing depositional inclination is reversed after the correction, though more importantly, ζ becomes more constant throughout different depositional field inclinations.

Overall, experiments that are initially loosely clustered (those with vertical depositional fields) tighten after the correction. Those that are tightly clustered before the correction become elongate, typically in the vertical direction (Fig. 2.4, 2.5, 2.9). A restoration of the original depositional field inclination from the remanent vector should theoretically produce a circular distribution of directions in a natural setting where paleosecular variation occurs. However, because our sediment was deposited extremely rapidly compared to a natural setting, and there is no magnetic polar wander, our uncorrected distributions are significantly more clustered than would be expected in nature. Because the distributions start out almost circular and tightly clustered, the correction produces distributions of directions that are elongated in the vertical plane, which is reflected in the higher girdling. The 90° field inclination experiments instead start out more elongate in the horizontal plane and become more circular after correction. In vertical fields, particle scatter is enhanced as the magnetic field is orthogonal to the bedding plane, and the correction works well to restore that scatter.

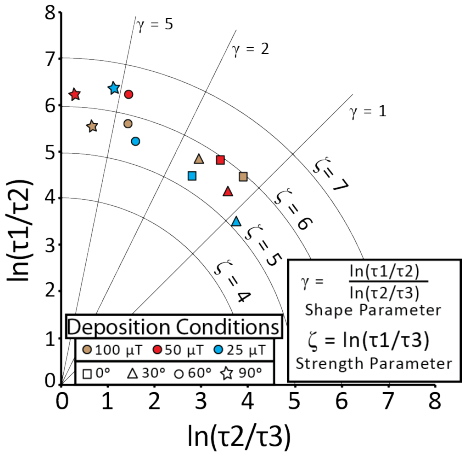

Figure 2.9. Woodcock (1977) shape analysis of the corrected NRM vector distribution. Strength of clustering increases in vertical fields. The shape of the distributions becomes closer to girdling in all other inclinations, with the strength parameter decreasing only slightly overall.

2.4.3 Corrected RPI estimates

After correction of the DRM vector and of the normalizing ARMs, the dependence of the RPIs on the depositional field inclination is reduced (Fig 2.9). The variance between experiments conducted in the same depositional intensity but different inclinations, as measured by the standard deviation of the mean RPI, is reduced after the correction (Table 6). In the 25 μT and 100 μT experiment series the standard deviation is cut by approximate 50% after the correction, and by about 65% in the 50 μT series.

Table 6. Variance of the RPI estimates

Depositional Intensity (μT)	Uncorrected Average RPI	Uncorrected Standard Deviation	Corrected Average RPI	Corrected Standard Deviation
25	0.3	0.16	0.46	0.08
50	0.39	0.16	0.57	0.06
100	0.63	0.31	0.85	0.16

This improvement is also visually apparent when Figure 2.10 is compared with Figure 6b. After the correction is applied, there is consistent RPI across experiments conducted at a given field intensity, rather than decreasing with increasing depositional intensity, as observed for the uncorrected RPIs. Variation remains, however, complicating the interpretations of the corrected RPI estimates: the 90° field inclination experiment from the 100 μT series is significantly lower than the other experiments, and falls just above the RPI of the experiment with the same inclination and 50 μT field intensity. Repeats of this experiment confirm this result, and further investigation is needed to determine whether this effects reflects a limitation of the DRM process in vertical fields. We postulate that this effect may be due to a saturation of the DRM in shallower inclinations of our strongest depositional field strength, but a failure to saturate in the vertical field. Experiments at inclinations between 60° and 90°, and in fields between 50 and 100 μT are needed to fully evaluate this effect.

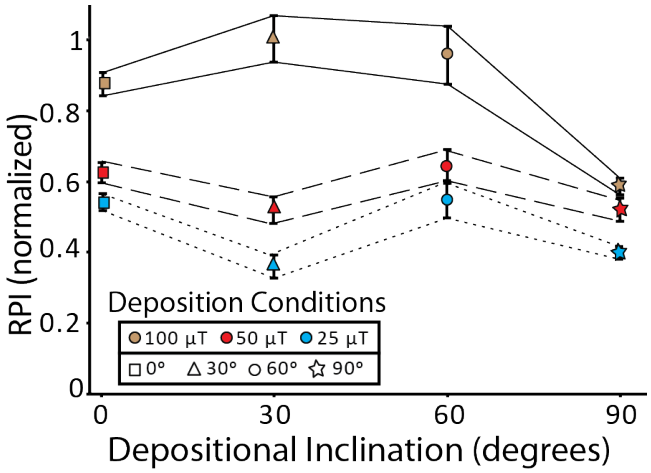

Figure 2.10. Corrected relative paleointensity estimates. With the exception of the 100 μT vertical field deposition experiment, RPI is generally stable across inclinations, and the dependence of intensity on inclination (decreasing intensity with increasing inclination) is removed.

2.5 Conclusions

These experiments, though not intended to fully replicate the complexities of natural deposition, let us evaluate the correction of RPI in cases of extreme inclination shallowing. In most depositional field inclinations and intensities, the AARM based correction of the DRM vectors improves RPI estimates. The RPI estimates derived from uncorrected DRMs and uncorrected saturating magnetizations fail to overcome the declining remanent intensity with increasing depositional inclination. Before correction we observe that the inclination and intensity of remanence depend of the inclination and intensity of the depositional field. We find an average *f* factor 0.22 with a standard deviation of 0.04. This is smaller (indicating more inclination shallowing) than would be expected in naturally deposited sediments (0.4 to 0.8, Bilardello and Kodama, 2010) and indicates that the high concentration of sediment in our experiments successfully enhanced the process of inclination shallowing. The best correction that fully restores

settling field inclination is obtained with an average anisotropy of individual particles of 1.82 with a standard deviation of 0.1.

Due to the rapid-settling and high concentration of suspended solids of our experiments, the distribution of DRM vectors in non-vertical depositional fields is highly clustered before the correction, with a horizontal E-W distribution for vertical settling fields, and a vertical up-down elongation for horizontal settling fields. After the correction, the distributions become more tightened in the E-W plane but more elongate in the vertical plane for all settling fields except 90° inclinations, which become nearly circular. This is further confirmed statistically by the increasing precision parameter and decreasing of the α_{95} of Fisher (1953), though this statistical scheme is best suited for circular distributions and ours are quite elongate ($\tau_2/\tau_3 > 1$).

Our experiments were designed to enhance inclination shallowing, and such a highly clustered vector distribution would be rare in a natural depositional setting. Since the correction changes the shape of the distribution from nearly circular to elongate in the vertical plane, it would be reasonable that it would take an initial east-west elongation, which is expected for naturally deposited, shallowed sediments that capture paleosecular variation, and restore a more circular distribution.

The trend of decreasing RPI with increasing inclination and decreasing intensity of the depositional field is removed by the correction, while the RPI's dependence on depositional intensity is preserved. This stabilization of RPI in constant depositional intensities and across varying inclinations helps us improve RPI estimates in our experiments and decreases the remanent intensity's dependence on depositional inclination. However, future experiments conducted under additional field intensities, and a finer scale of inclinations will further improve RPI estimates.

Future study may be able to determine directly whether the magnitude of this effect applies to naturally deposited sediments, however, to establish the validity of our experiments we make the following considerations: inclination shallowing occurs in nature and we have successfully reproduced the shallowing process in the laboratory; the inclination error can be corrected for in natural rocks, and we have restored the inclinations to that of the laboratory field. In nature, inclination shallowing leads to a field inclination dependence of the RPIs, and we have reproduced the same conditions experimentally. We find that correcting the DRMs (and saturating magnetizations) betters the RPIs over a range of inclinations in the laboratory, suggesting that our results are valid for the same processes occurring in nature, yet at different scales.

References

Anson, G. L. & Kodama K.P., 1987, Compaction-induced inclination shallowing of the post-depositional remanent magnetization in a synthetic sediment *Geophysical Journal of the Royal Astronomical Society*, **88**, 673-692.

Arason, P. & Levi, S., 1990, Compaction and inclination shallowing in deep sea sediments from the Pacific Ocean, *Journal Geophysical Research*, **95**, 4501-4510.

Bilardello, D., 2013, Understanding DRM acquisition of plates and spheres: a first comparative experimental approach, *Geophyical Journal International*, **195**, 148-158, DOI: 10.1093/gji/ggt240.

Bilardello, D. & Kodama, K.P., 2010, Rock magnetic evidence for inclination shallowing in the early Carboniferous Deer Lake Group red beds of western Newfoundland, *Geophys. J. Int*., **181**, 275-289, doi: 10.1111/j.1365-246X.2010.04537.x.

Bilardello, D. Jezek. J. & Kodama, K. P., 2011, Propagating and incorporating the error in anisotropy-based inclination corrections, *Geophys. J. Int*., **187**, 1, 75-84, doi: 10.1111/j.1365-246X.2011.05138.x.

Bilardello, D., Jezek, J. & Gilder, S.A., 2013, Role of spherical particles on magnetic field recording in sediments: Experimental and numerical results, *Physics of the Earth Planetary Interiors*, **214,** 1-13, DOI: 10.1016/j.pepi.2012.10.014.

Blow, R. A. & Hamilton, N., 1978, Effect of compaction on the acquisition of a detrital remanent magnetization in fine-grained sediments, *Geophysical Journal of the Royal Astronomical Society*, **52**, 13-23.

Buffett, B., 2016, Another energy source for the geodynamo, *Nature*, **529**, 288-289

Butler, R. F., 1992, Paleomagnetism: Magnetic Domains to Geologic Terranes, *Blackwell, Boston*, 319 pp.

Campbell, W.H., 2003, Introduction to Geomagnetic Fields, Second Edition, *Cambridge University Press, Cambridge,* 337 pp.

Chang, L., Roberts, A.P., Heslop, D., Hayashida, A., Li, J., Zhao, X., Tian, W., & Huang, Q., 2016, Widespread occurrence of silicate-hosted magnetic mineral inclusions in marine sediments and their contribution to paleomagnetic recording, *J. Geophys. Res. Solid Earth*, **121**, 8415-8431, doi:10.1002/2016JB013109.

Collinson, D.W., 1965, DRM in sediments. *J. Geophys. Res*., **70**, 4663-4668.

Constable, C., & Tauxe, L., 1996, Towards absolute calibration of sedimentary paleointensity records, *Earth Planet. Sci. Lett*., **143**, 269-274.

Davies, C.J., & Constable, C.G., 2014, Insights from geodynamo simulations into long-term geomagnetic field behavior, *Earth Planet. Sci. Lett*., **404**, 238-249.

Day, R., Fuller, M. & Schmidt, V.A., 1977, Hysteresis properties of titanomagnetites: Grain-size and compositional dependence. *Phys. Earth Planet. Int*., **13**, 260-267.

Droppo, I.G. & Ongley, E.D., 1994, Flocculation of suspended sediment in rivers of southeastern Canada, *Wat. Res.,* **28** (8), 1799-1809.

Dunlop, D., 2002, Theory and application of the Day plot (Mrs/Ms versus Hcr/Hc) 1. Theoretical curves and tests using titanomagnetite data, *Journal of Geophysical Research*, **107**, B3, doi: 10.1029/2001JB000486.

Egli, R., 2013, VARIFORC: An optimized protocol for the calculation of non-regular first-order reversal curve (FORC) diagrams, *Global and Planetary Change*, **110,** 302-320, doi:10.1016/j.glopacha.2013.08.003.

Fisher, R. A., 1953. Dispersion on a sphere. *Proceedings of the Royal Society of London*, *Ser. A*, **217**, 295-305.

Girdler, R.W., 1961, The measurement and computation of anisotropy of magnetic

susceptibility in rocks, *Geophys. J. R. Astron. Soc.*, **5**, 34-44.
Griffiths, D. H., King, R. F., Rees, A. I. & Wright, A. E., 1960, Remanent magnetism of some recent varved sediments, *Proceedings of the Royal Society of London, Ser. A.*, **256**, 359-383.
Guyodo, Y. & Valet, J.-P., 1996, Relative variations in geomagnetic intensity from sedimentary records: the past 200 thousand years, *Earth Planet. Sci. Lett***. 143**, 23-36.
Guyodo, Y. & Valet, J.P., 1999, Global changes in intensity of the Earth's magnetic field during the past 800 kyr, *Nature*, **399**, 249-252.
Guyodo, Y., & Valet, J.P., 2006, A comparison of relative paleointensity records of the Matuyama Chron for the period 0.75-1.25 Ma, *Phys. Earth Planet. Int.,* **156**, 205-212.
Harrison, R. J., & Feinberg, J. M., 2008, FORCinel: An improved algorithm for calculating first-order reversal curve distributions using locally weighted regression smoothing, *Geochemistry, Geophysics, Geosystems*, **9**, Q05016, doi:10.1029/2008GC001987.
Hatfield, R.G., Stoner, J.S., Carlson, A.E., Reyes, A.V., & Housen, B.A., 2013, Source as a controlling factor on the quality and interpretation of sediment magnetic records from the northern North Atlantic, *Earth Planet. Sci. Lett*., **368,**69-77.
Helsop., D., 2007, Are hydrodynamic shape effects important when modelling the formation of depositional remanent magnetization?, *Geophys. J. Int.*, **171**, 1029-1035, doi:10.1111/j.1365-246X.2007.03588.x.
Heslop, D., Roberts, A.P., Hawkins, R., 2014, A statistical simulation of magnetic particle alignment in sediments, *Geophysical Journal International*, **197**, 828-837, doi: 10.1093/gji/ggu038.
Irving, E and Major, A., 1964, Post-depositional remanent magnetization in a synthetic sediment, *Sedimentology*, **3**, 135-143.
Jackson, M., Banerjee, S. K., Marvin, J.A., Lu, R. & Gruber, W., 1991, Detrital remanence inclination errors and anhysteretic remanence anisotropy: quantitative model and experimental results, *Geophysical Journal International*, **104**, 95-103.
Jelinek, V., 1981, Characterization to the magnetic fabric of rocks, *Tectonophysics*, **79**, T63–T67.
Jezek, J. & Gilder, S.A., 2006, Competition of magnetic and hydrodynamic forces on ellipsoidal particles under shear: Influence of the Earth's magnetic field on particle alignment in viscous media, *Journal of Geophysical Res*earch, **111**, B12S123, doi:10.1029/2006JB004541.
Jiilavenkatesa, A., Dapkunas, S. J., & Lum, L. H. 2001, Particle Size Characterization, U.S. Department of Commerce*, Chapter 6: Size characterization by laser light diffraction techniques.*
Jirsa, M.A., Miller Jr., J.D., & Morey, G.B., 2008, Geology of the Biwabik Iron Formation and Duluth Complex, *Regulatory Toxicology and Pharmacology,* **52,** S5-S10, doi:10.1016/j.yrtph.2007.09.009.
Johnson, E.A., Murphy, T. and Torreson, O.W., 1948, Pre-history of the Earth's magnetic field, *Terrestrial Magnetism and Atmospheric Electricity*, **53**, 349–372.
Katari, K. & Tauxe, L., 2000, Effects of pH and salinity on the intensity of magnetization in redeposited sediments, *Earth and Planetary Science. Lett*ers, **181**, 489-496.
Kent, D. V., 1973, Post-depositional remanent magnetization in deep-sea sediment, *Nature*, **246**, 32-34.
Kim, B. Y., Kodama, P.K., 2004, A compaction correction for the paleomagnetism of

the Nanaimo Group sedimentary rocks: Implications for the Baja British Columbia hypothesis, *Journal of Geophysical Research*, **109**, B02102, doi:10.1029/2003JB002696.
King, R. F., 1955, The remanent magnetism of artificially deposited sediments, *Mon. Notic. Roy. Astron. Soc. Geophys. Suppl*, **7**, 115-134.
Kodama, K.P. & Sun, W.W., 1990, SEM and magnetic fabric study of a compacting sediment, *Geophys. Res. Lett.,* **17**, 795-798.
Kodama, K. P., 2009, Simplification of the anisotropy-based inclination correction technique for magnetite- and hematite bearing rocks: A case study for the Carboniferous Glenshaw and Mauch Chunk Formations, North America, *Geophys. J. Int*., **176**, 467-477, doi: 10.1111/j.1365-246X.2008.04013.x
Korte, M., & Constable, C.G., 2003, Continuous global geomagnetic field models for the past 3000 years, *Phys. Earth Planet. Inter*., **140**, 73–89.
Korte, M., & Constable, C.G. 2005, Continuous geomagnetic field models for the past 7 millennia: 2. CALS7K, *Geochem. Geophys. Geosyst*., **6**, Q02H16, doi:10.1029/2004GC000801.
Korte, M., and Constable, C.G., 2006, On the use of calibrated relative paleointensity records to improve millennial scale geomagnetic field models, *Geochem. Geophys. Geosyst.* **7** (9), Q09004, doi:10.1029/2006GC00136.
Korte, M. & Constable, C., 2011, Improving geomagnetic field reconstructions for 0–3 ka*, Phys. Earth Planet. Int.,* **188**, 247–259.
Korte, M., Constable, C. & Donadini, F., 2009, Geomagnetic field for 0-3 ka: 2. Revised global time-varying models, *Geochem. Geophys. Geosyst.*, **10**, Q06008, doi:10.1029/2008GC002297.
Korte, M., Constable, C., Donadini, F. & Holme, R., 2011, Reconstructing the Holocene geomagnetic field, *Earth Planet. Sci. Let.,* **312**, 497-505.
Levi, S., and Banerjee, S.K., 1976, On the possibility of obtaining relative paleointensities from lake sediments, *Earth Planet. Sci. Lett*., **29**, 219-226.
Maxbauer, D.P., Feinberg, J.M., and Fox, D.L., 2016, MAX UnMix: A web application for unmixing magnetic coercivity distributions, *Computers & Geosciences*, **95**, 140-145.
McCabe, C., Jackson, M., and Elwood, B. B., 1985, Magnetic anisotropy in the Trenton limestone: Results of a new technique, anisotropy of anhysteretic susceptibility, *Geophys. Res. Lett*., **12**, 6, 333-336.
McNish, A.G. & Johnson, E.A., 1938, Magnetization of sediments from the bottom of the Atlantic Ocean, *Eos Transactions, American Geophysical Union,* **19**, 204-205.
Mitra, R. & Tauxe, L., 2009, Full vector model for magnetization in sediments, *Earth Planet. Sci. Lett*., **286**, 535-545.
Nagata, T., 1961, Rock Magnetism, Maruzen, Tokyo, 348 pp.
Nilsson, A., Holme, R., Korte, M., Suttie, N., Hill, M., 2014, Reconstructing Holocene geomagnetic field variation: new methods, models and implications, *Geophys. J. Int.*, **198**, 229-248.
Panovska, S., Korte, M., Finlay, C.C., & Constable, C.G., Limitations in paleomagnetic data and modelling techniques and their impact on Holocene geomagnetic field models, *Geophys. J. Int.*, **202**, 402-418, doi: 10.1093/gji/ggv137.
Roberts, A., Tauxe, L., Heslop, D., 2013, Magnetic paleointensity stratigraphy and high-resolution Quaternary geochronology: successes and future challenges, *Quat. Sci. Rev*., **61**, 1-16.
Selkin, P.A., Gee, J.S., Tauxe, L., Meurer, W.P., Newell, A.J., 2000, The effect of remanence anisotropy on paleointensity estimates: a case study from the

Archean Stillwater Complex, *Earth Planet. Sci. Lett*., **183**, 403-416.
Shcherbakov, V., Shcherbakova, V., 1983, On the theory of depositional remanent magnetization in sedimentary rocks, *Geophys. Surv*., **5**, 369–380.
Shcherbakov, V., Sycheva, N.K., 2010, On the mechanism of formation of depositional remanent magnetization, *Geoch. Geophys. Geosyst*., **11**, 2, doi:10.1029/2009GC002830.
Stumm, W. & Morgan, J., 1996, Aquatic Chemistry: Chemical Equilibria and Rates in Natural Waters, *Wiley, New York.*
Sun, W. W. & Kodama, K. P., 1992, Magnetic anisotropy, scanning electron microscopy, and X ray pole figure goniometry study of inclination shallowing in a compacting clay-rich sediment, *J. Geophys. Res*., **97**, 9599-9615.
Tarling, D. H. and Hrouda, F., 1993, The Magnetic Anisotropy of Rocks, *Chapman and Hall*, London, 217 pp.
Tauxe, L. & Kent, D.V., 1984, Properties of a detrital remanence carried by hematite from study of modern river deposits and laboratory redeposition experiments, *Geophys. J. R. Astron. Soc*., **77**, 543-561.
Tauxe, L. and Kent, D. V., 2004, A simplified statistical model for the geomagnetic field and the detection of shallow bias in paleomagnetic inclinations: Was the ancient field dipolar?, In: J.E.T. Channell, D.V. Kent, W. Lowrie and J. Meert, Editors, *Timescales of the Internal Geomagnetic Field*, Geophysical Monograph, **145**, 101-116.
Tauxe, L. and Yamazaki, T., 2007, Paleointensities, In: *Treatise on Geophysics*, Gerald Schubert, Ed., Elsevier, 5, 13, 509-563.
Tauxe, L, Pick, T., Kok, Y.S., 1995, Relative paleointensity in sediments: a pseudo-Thellier approach, *Geophys. Res. Lett.,* **22** (21), 2885-2888.
Tauxe, L., Steindorf, J.L. & Harris, A., 2006, Depositional remanent magnetization: Toward an improved theoretical and experimental foundation, *Earth Planet. Sci. Lett.*, **244**, 515-529.
Tauxe, L., Shaar, R., Jonestrask, L., Swanson-Hysell, N. L., Minnett, R., Koppers, A. A. P., Constable, C. G., Jarboe, N., Gaastra, K., & Fairchild, L., 2016, PmagPy: Software package for paleomagnetic data analysis and a bridge to the Magnetics Information Consortium (MagIC) Database, *Geochem. Geophys. Geosyst*., **17**, doi:10.1002/2016GC006307.
Thellier, E. & Thellier, O., 1959, Sur l'intensité du champ magnétique terrestre dans la passé historique et géologique, *Ann. Géophys*. **15**, 285-376.
Valet, J.P., Meynadier, L. & Guyodo, Y., 2005, Geomagnetic dipole strength and reversal rate over the past two million years, *Nature*, **435,** 802-805.
Van Vreumingen, M.J., 1993a, The magnetization intensity of some artificial suspensions while flocculating in a magnetic field*, Geophys. J. Int*., **114**, 601–606.
Van Vreumingen, M.J., 1993b, The influence of salinity and flocculation upon the acquisition of remanent magnetization in some artificial sediments, *Geophys. J. Int*., **114**, 607-614.
Veikkolainen, T., Heimpel, M., Evans, M.E., Pesonen, L.J., & Korhonen, K., 2017, A paleointensity test of the geocentric axial dipole (GAD) hypothesis, *Phys. Earth Planet. Int.*, **265**, 54-61, doi: 10.1016/j.pepi.2017.02.008
Verosub, K.L., 1977, Depositional and postdepositional processes in the magnetization of sediments, *Rev. Geophys. Space Phys*., **15**, 2, 129-143.
Winchell, N.H., 1901, Glacial lakes of Minnesota, *Bulletin of the Geological Society of America,* **12**, 109-128.

Woodcock, N.H., 1977, Specification of fabric shapes using an eigenvalue method, *Bulletin of the Geological Society of America,* **88**, 1231-1236.

Yadav, R.K., Gastine, T., Christensen, U.R., Wolk, S.J. & Poppenhaeger, K., 2016, Approaching a realistic force balance in geodynamo simulations, *Proc. Nat. Acad. Sci. U.S.A,* **113**, 12065-12070, doi: 10.1073/pnas.1608998113.

Ziegler, L.B. & Constable, C.G., 2015, Testing the geocentric axial dipole hypothesis using regional paleomagnetic intensity records from 0 to 300 ka, *Earth Planet. Sci. Let.*, **423**, 48-56, doi:1 0.1016/j.epsl.2015.04.022.

Ziegler, L.B., Constable, C.G., Johnson, C.L., & Tauxe, L., 2011, PADM2M: a penalized maximum likelihood model of the 0–2Ma palaeomagnetic axial dipole moment, *Geophys. J. Int.*, **184**, 1069-1089, http://dx.doi.org/10.1111/j.1365–246X.2010.04905.x.

Appendix A. Specimen Masses

Specimen Masses - grams

Specimen	RM25-0	RM25-30	RM25-60	RM25-90	RM50-0	RM50-30	RM50-60	RM50-90c	RM100-0	RM100-30b	RM100-60	RM100-90b
RMInt-Inc-1	2.93243	3.6568	2.8384	3.86857	2.7083	3.8208	3.6511	2.5418	2.8568	4.7701	4.1923	2.275
RMInt-Inc-10	2.95808	4.1044	2.6365	4.33198	2.7239	3.9188	3.5106	2.3799	2.8353	4.9607	4.4025	3.2318
RMInt-Inc-11	2.79431	3.787	2.6423	3.73501	2.5843	3.7303	3.2991	2.5002	3.0278	4.5306	4.2717	3.4393
RMInt-Inc-12	2.84224	3.9156	2.7229	4.56399	2.657	3.927	3.9432	2.9009	3.0117	5.2479	4.4683	3.4128
RMInt-Inc-13	2.97695	3.8714	2.6745	4.27679	2.611	3.8201	3.7884	2.6407	2.6898	5.263	4.6921	2.886
RMInt-Inc-14	3.07544	4.1121	2.877	4.26025	2.6914	3.6648	3.9545	2.2801	2.7692	5.3051	4.5588	3.2957
RMInt-Inc-15	2.96818	3.8915	2.6479	4.14614	2.6846	3.7141	3.4696	2.5756	2.836	4.9508	4.6181	3.334
RMInt-Inc-16	2.78816	3.8856	2.6644	3.70991	2.5777	4.0381	3.3338	2.4696	2.9863	4.4738	4.3054	3.5485
RMInt-Inc-17	2.83597	3.8073	2.698	4.21198	2.7489	3.8199	3.5392	2.5446	2.7993	5.273	4.4248	3.3919
RMInt-Inc-18	2.83795	3.8871	2.8409	3.95944	2.7809	3.8545	3.2113	2.5027	2.7522	5.1411	4.096	3.2786
RMInt-Inc-19	2.85456	4.0804	2.9519	3.83646	2.6066	3.5699	3.5686	2.4543	2.7925	4.9973	4.6326	3.2542
RMInt-Inc-2	2.99021	3.9693	2.7561	4.24361	2.5707	3.966	4.1333	2.6197	2.8842	5.082	4.627	3.4472
RMInt-Inc-20	2.8977	3.842	2.8159	3.92725	2.548	3.8537	3.2144	2.5801	2.9938	4.7088	4.2056	3.3341
RMInt-Inc-21	2.79597	3.6063	2.6573	3.38898	2.6095	3.6699	3.3318	2.5274	2.8434	4.4835	4.1085	3.1568
RMInt-Inc-22	2.92338	3.787	2.7441	3.71131	2.6498	3.7873	3.2137	2.5753	2.7839	4.6141	4.3281	3.3526
RMInt-Inc-23	2.91066	3.2802	2.9545	3.52138	2.6148	3.6572	3.2245	2.4983	2.8915	4.5992	4.2422	3.0008
RMInt-Inc-24	3.10273	3.7174	2.9152	4.14788	2.7211	3.9119	4.1943	2.5041	2.865	4.8432	4.4178	3.3585
RMInt-Inc-25	2.95776	3.7728	2.6913	3.75295	2.6497	3.6256	4.0733	2.5821	3.0317	4.6718	4.374	3.5722
RMInt-Inc-3	2.93504	3.8017	2.7193	3.9082	2.6249	3.8974	3.9543	2.5284	2.7203	5.1715	4.8719	3.524
RMInt-Inc-4	2.8014	4.0502	2.6842	4.35606	2.6991	3.9616	3.4549	2.6155	3.0278	5.2483	4.902	3.4803
RMInt-Inc-5	2.93426	3.7292	2.9509	3.87491	2.7258	3.8571	3.6428	2.497	2.9986	4.8434	4.7156	3.3523
RMInt-Inc-6	2.82392	3.7159	2.6691	3.97905	2.6591	3.8232	3.8058	2.5117	2.4985	4.6372	4.3954	3.2404
RMInt-Inc-7	2.95156	3.8506	2.6815	3.76046	2.6675	3.8649	3.4952	2.3168	2.7593	5.2456	4.4455	3.4497
RMInt-Inc-8	2.84206	3.8648	2.6605	4.12198	2.5557	3.5829	3.9535	2.4419	2.6224	5.0711	4.2063	3.4746
RMInt-Inc-9	2.90952	4.059	2.6201	4.3673	2.5919	3.6942	3.5996	2.7127	2.9205	5.2486	4.3437	3.4837

Appendix B. Natural remanent magnetizations

25 microTesla field intensity experiments.

Specimen	Natural Remanent Magnetizations - Am^2											
	RM25-0			RM25-30			RM25-60			RM25-90		
	Mx	My	Mz	Mx	My	Mz	Mx	My	Mz	Mx	My	Mz
RMInt-Inc-1	-3.25046E-06	-7.1642E-08	2.91603E-07	-2.23483E-06	-1.14058E-07	2.42765E-07	-1.62163E-06	-3.1369E-08	3.88035E-07	3.05224E-07	-1.31382E-07	6.62342E-07
RMInt-Inc-10	-3.31481E-06	2.2173E-08	2.20155E-07	-2.34374E-06	-9.27839E-08	2.84431E-07	-1.65021E-06	-2.05236E-08	4.75849E-07	1.98975E-07	-1.49962E-07	6.68319E-07
RMInt-Inc-11	-3.1375E-06	-2.332E-08	1.73701E-07	-2.19101E-06	-1.36777E-07	3.04474E-07	-1.54808E-06	-9.6719E-08	5.35865E-07	4.35581E-07	1.30589E-07	5.9341E-07
RMInt-Inc-12	-3.28324E-06	1.10193E-07	1.74561E-07	-2.3538E-06	-3.99942E-08	2.49257E-07	-1.65628E-06	-1.1135E-07	4.64019E-07	2.54262E-07	1.43722E-08	6.94364E-07
RMInt-Inc-13	-3.31882E-06	-5.04318E-08	-5.45878E-08	-2.43787E-06	-4.19972E-08	2.74605E-07	-1.77662E-06	8.09037E-08	3.23297E-07	2.27932E-07	-1.24595E-07	6.85714E-07
RMInt-Inc-14	-3.19984E-06	2.03169E-07	1.58822E-07	-2.31495E-06	-5.90993E-08	4.17204E-07	-1.74414E-06	-6.69596E-08	3.57209E-07	3.21205E-07	-1.86953E-07	7.07111E-07
RMInt-Inc-15	-3.24899E-06	1.32576E-08	-3.35886E-08	-2.23896E-06	3.79243E-09	3.30647E-07	-1.58522E-06	2.69864E-08	5.1326E-07	2.65081E-07	-1.19292E-07	7.0775E-07
RMInt-Inc-16	-3.32567E-06	3.19222E-08	2.71752E-08	-2.36472E-06	-7.44719E-08	4.26018E-07	-1.37553E-06	2.62884E-07	4.54244E-07	3.87976E-07	9.12397E-08	6.1104E-07
RMInt-Inc-17	-3.22052E-06	1.8954E-08	1.42346E-07	-2.35213E-06	7.72241E-08	3.90732E-07	-1.60968E-06	3.44371E-08	3.27275E-07	4.01543E-07	-6.05206E-09	6.64842E-07
RMInt-Inc-18	-3.2656E-06	7.90603E-08	9.84528E-08	-2.34771E-06	2.47004E-08	4.25911E-07	-1.51635E-06	-2.34218E-08	5.94437E-07	2.95184E-07	-9.85152E-09	6.40359E-07
RMInt-Inc-19	-3.30506E-06	6.24167E-08	1.51184E-08	-2.28493E-06	-2.28954E-08	3.84496E-07	-1.64553E-06	2.42685E-08	4.09734E-07	4.53502E-07	6.55334E-08	6.75432E-07
RMInt-Inc-2	-3.32091E-06	-1.04517E-07	2.79058E-07	-2.34144E-06	-1.1745E-07	2.40652E-07	-1.45753E-06	-1.01291E-07	5.07335E-07	4.48373E-07	-1.40165E-07	6.80631E-07
RMInt-Inc-20	-3.39092E-06	5.93741E-08	-6.93281E-08	-2.19671E-06	9.85212E-09	4.29257E-07	-1.66853E-06	9.8127E-08	5.00101E-07	1.86219E-07	3.97893E-08	6.53041E-07
RMInt-Inc-21	-3.24194E-06	2.23367E-07	1.37967E-08	-2.26138E-06	-2.96926E-08	3.16745E-07	-1.64069E-06	4.55666E-08	4.96247E-07	4.12932E-07	1.49618E-07	5.96658E-07
RMInt-Inc-22	-3.1516E-06	6.72786E-08	5.97058E-08	-2.32247E-06	5.03767E-08	2.9902E-07	-1.5965E-06	1.04517E-07	4.23346E-07	3.97313E-07	1.30896E-07	6.71001E-07
RMInt-Inc-23	-3.24102E-06	1.33702E-07	-3.13956E-08	-2.27344E-06	8.50919E-08	3.90202E-07	-1.57775E-06	1.24444E-07	4.58641E-07	4.14765E-07	1.032E-07	5.97408E-07
RMInt-Inc-24	-3.53145E-06	2.33554E-08	-8.12671E-10	-2.24558E-06	2.94569E-08	3.32141E-07	-1.69144E-06	7.50323E-08	4.41119E-07	2.95494E-07	1.68284E-08	7.08591E-07
RMInt-Inc-25	-3.23385E-06	6.87279E-08	-6.81669E-08	-2.44435E-06	-4.63956E-08	3.75566E-07	-1.73756E-06	1.34556E-07	4.18675E-07	1.94717E-07	9.95247E-08	6.22752E-07
RMInt-Inc-3	-3.25772E-06	-5.41732E-08	1.39623E-07	-2.31793E-06	-1.16778E-07	2.46553E-07	-0.000001713	-3.91837E-08	4.56206E-07	2.86081E-07	-2.43943E-07	6.71111E-07
RMInt-Inc-4	-3.2515E-06	-5.3699E-08	2.11922E-07	-2.30504E-06	-1.32319E-07	2.29412E-07	-1.53506E-06	-1.49498E-07	4.98806E-07	2.44595E-07	-2.48508E-07	6.8829E-07
RMInt-Inc-5	-3.30844E-06	3.29362E-08	1.69142E-07	-2.36397E-06	-1.19588E-07	1.86189E-07	-1.63949E-06	-1.00316E-07	5.18774E-07	2.48151E-07	-1.20643E-07	6.68658E-07
RMInt-Inc-6	-3.27624E-06	1.36563E-08	9.5336E-09	-2.36457E-06	-8.55673E-08	1.72426E-08	-1.64564E-06	-1.75497E-07	4.70422E-07	2.55323E-07	4.33693E-08	7.1239E-07
RMInt-Inc-7	-3.31589E-06	-4.6277E-08	2.61317E-07	-2.3587E-06	-1.61437E-08	5.23651E-08	-1.67325E-06	-7.06794E-08	4.90858E-07	1.51547E-07	-6.13858E-08	6.39534E-07
RMInt-Inc-8	-3.20514E-06	-3.43054E-08	8.07618E-08	-2.28951E-06	2.73212E-08	2.37624E-07	-1.58385E-06	-3.79837E-08	4.76757E-07	2.86194E-07	-1.21184E-07	6.99114E-07
RMInt-Inc-9	-3.31402E-06	5.24387E-08	4.40268E-07	-2.35842E-06	-1.82003E-08	1.9089E-07	-1.65445E-06	4.96957E-08	4.21505E-07	3.5318E-07	-1.02424E-07	6.83743E-07

50 microTesla field intensity experiments

Natural Remanent Magnetizations - Am^2

Specimen	RM50-0			RM50-30			RM50-60			RM50-90c		
	Mx	My	Mz	Mx	My	Mz	Mx	My	Mz	Mx	My	Mz
RMInt-Inc-1	-3.09355E-06	1.74793E-08	1.72567E-07	-3.50642E-06	1.84968E-07	4.53595E-07	-2.31119E-06	1.88974E-09	7.81288E-07	5.07782E-07	-1.43847E-07	8.56947E-07
RMInt-Inc-10	-3.25769E-06	8.70835E-08	-1.70279E-07	-3.45211E-06	2.01271E-08	4.05367E-07	-2.12673E-06	1.77918E-07	1.09775E-06	-1.06539E-07	1.16851E-07	1.07229E-06
RMInt-Inc-11	-3.29746E-06	9.21197E-08	2.53499E-08	-3.65564E-06	1.56878E-07	3.57292E-07	-2.35481E-06	-5.07522E-08	8.20896E-07	3.4735E-07	-1.70558E-08	9.20375E-07
RMInt-Inc-12	-3.22386E-06	1.29042E-07	-1.62407E-07	-3.57782E-06	1.41399E-07	3.85088E-07	-2.15342E-06	5.3803E-08	9.478E-07	5.95272E-08	-1.3626E-08	9.63341E-07
RMInt-Inc-13	-3.30492E-06	1.67982E-07	2.0408E-08	-3.65673E-06	1.87103E-07	3.8119E-07	-2.32007E-06	-1.14151E-07	8.57009E-07	2.06556E-08	-4.09725E-08	9.37221E-07
RMInt-Inc-14	-3.30883E-06	1.36963E-07	-6.74719E-08	-3.69379E-06	5.54214E-08	5.8127E-07	-2.4113E-06	-1.74756E-07	1.04584E-06	2.28537E-07	-1.19971E-07	9.07844E-07
RMInt-Inc-15	-3.29857E-06	6.94065E-08	-5.68524E-08	-3.25038E-06	1.7419E-07	4.55141E-07	-1.99761E-06	-1.78828E-08	8.87411E-07	1.79301E-07	-6.15102E-08	9.1838E-07
RMInt-Inc-16	-3.29835E-06	1.53497E-07	4.09937E-08	-3.51566E-06	3.08882E-07	5.12431E-07	-2.39217E-06	6.92772E-08	9.05247E-07	1.89684E-07	-2.18056E-08	9.57725E-07
RMInt-Inc-17	-3.2685E-06	1.14128E-07	-4.95871E-08	-3.63124E-06	1.76324E-07	5.4136E-07	-2.36995E-06	-9.15434E-08	8.44502E-07	2.61808E-07	1.35235E-07	9.28579E-07
RMInt-Inc-18	-3.28024E-06	1.93486E-07	4.96381E-08	-3.60876E-06	1.30779E-07	5.61567E-07	-2.3127E-06	1.01935E-08	9.08459E-07	2.6244E-07	6.40792E-08	9.09382E-07
RMInt-Inc-19	-3.23884E-06	1.56042E-07	-7.86052E-08	-3.71878E-06	2.35943E-07	3.0699E-07	-2.36461E-06	2.88556E-08	8.30114E-07	2.51716E-07	3.86645E-08	1.05325E-06
RMInt-Inc-2	-3.12334E-06	9.16894E-08	5.27092E-08	-3.55356E-06	1.87386E-07	3.72898E-07	-2.35657E-06	-2.0637E-08	8.08346E-07	1.95803E-07	-1.54788E-07	1.03474E-06
RMInt-Inc-20	-3.29142E-06	9.69154E-08	9.48615E-08	-3.53249E-06	1.25114E-07	5.52801E-07	-2.41992E-06	2.17498E-07	8.49242E-07	1.08012E-07	1.76523E-07	9.73894E-07
RMInt-Inc-21	-3.23754E-06	1.44676E-07	-1.38848E-07	-3.64916E-06	3.38549E-07	3.13282E-07	-2.28886E-06	7.02597E-08	8.34283E-07	3.17765E-07	7.96127E-08	8.67153E-07
RMInt-Inc-22	-3.23527E-06	1.37017E-07	-1.35388E-07	-3.70191E-06	1.71444E-07	2.83374E-07	-2.50114E-06	-1.29555E-08	7.94551E-07	2.42662E-07	-5.57147E-08	9.57568E-07
RMInt-Inc-23	-3.26163E-06	1.42829E-07	6.32953E-08	-3.68433E-06	2.0888E-07	2.29377E-07	-2.46356E-06	3.45057E-08	8.88145E-07	1.40773E-07	2.26041E-07	9.71508E-07
RMInt-Inc-24	-3.27459E-06	6.96398E-08	-1.7255E-07	-3.6066E-06	2.16597E-07	8.46415E-08	-2.47731E-06	5.33524E-08	8.97612E-07	3.07064E-07	2.75493E-08	9.32028E-07
RMInt-Inc-25	-3.04594E-06	1.57928E-07	-1.87355E-07	-3.78515E-06	1.36272E-07	1.37287E-07	-2.50517E-06	-2.81837E-08	9.33214E-07	8.24011E-08	2.19291E-07	9.3808E-07
RMInt-Inc-3	-3.19845E-06	7.26315E-08	-3.39409E-08	-3.56595E-06	7.48476E-08	4.8031E-07	-2.39089E-06	-9.19648E-08	9.74801E-07	1.53787E-07	-1.70486E-07	1.06422E-06
RMInt-Inc-4	-3.23987E-06	4.20073E-08	-2.10546E-07	-3.54436E-06	1.2973E-07	5.29214E-07	-2.18976E-06	1.71684E-07	9.19447E-07	1.43715E-07	-1.8554E-07	9.77779E-07
RMInt-Inc-5	-3.23977E-06	1.04289E-07	-9.98352E-08	-3.47805E-06	5.64321E-08	4.5701E-07	-2.19532E-06	-5.86231E-08	8.37355E-07	7.09214E-08	1.83472E-08	9.77018E-07
RMInt-Inc-6	-3.21072E-06	1.30253E-08	1.32055E-09	-3.5439E-06	1.89137E-07	4.13037E-07	-2.43632E-06	-2.00804E-08	9.20884E-07	2.15233E-07	-9.96029E-08	9.63855E-07
RMInt-Inc-7	-3.28827E-06	8.94481E-08	-1.52695E-07	-3.61598E-06	1.42673E-07	4.47374E-07	-2.13872E-06	-9.70797E-08	9.02285E-07	8.18321E-08	-3.91496E-08	9.40221E-07
RMInt-Inc-8	-3.33022E-06	8.94784E-08	5.69349E-08	-3.73277E-06	1.51087E-08	3.76318E-07	-2.33841E-06	-7.07326E-08	8.17748E-07	-1.98741E-08	-6.6255E-09	9.77675E-07
RMInt-Inc-9	-3.34898E-06	1.36905E-07	1.82423E-07	-3.65116E-06	6.26071E-08	2.54401E-07	-2.30409E-06	-3.6665E-08	8.77525E-07	1.5445E-07	-5.87345E-08	9.67486E-07

Natural Remanent Magnetizations - Am^2

Specimen	RM100-0			RM100-30b			RM100-60			RM100-90b		
	Mx	My	Mz	Mx	My	Mz	Mx	My	Mz	Mx	My	Mz
RMInt-Inc-1	-4.65606E-06	1.5196E-07	8.26639E-08	-6.99243E-06	3.09255E-07	1.47129E-06	-2.76301E-06	2.74934E-07	1.37108E-06	3.0621E-07	7.95806E-07	1.40404E-06
RMInt-Inc-10	-4.44039E-06	1.88267E-07	-1.32221E-07	-7.01517E-06	2.39353E-07	1.41106E-06	-3.03546E-06	2.99021E-07	1.17197E-06	4.20467E-07	-2.34366E-07	1.92592E-06
RMInt-Inc-11	-4.57985E-06	1.4518E-07	-8.597E-08	-7.15284E-06	1.13121E-07	1.17273E-06	-3.09266E-06	1.75071E-07	1.01251E-06	2.50188E-07	-2.70807E-08	1.88121E-06
RMInt-Inc-12	-4.59743E-06	7.94219E-08	-2.35038E-07	-7.28578E-06	1.47962E-08	1.10068E-06	-2.74092E-06	1.9665E-08	1.14694E-06	6.19574E-07	4.08542E-08	1.85666E-06
RMInt-Inc-13	-4.24727E-06	2.10644E-07	-3.62805E-08	-7.18923E-06	2.7484E-08	1.24384E-06	-2.61658E-06	2.54956E-07	1.05362E-06	6.9492E-08	1.16247E-07	1.72356E-06
RMInt-Inc-14	-4.31207E-06	2.44449E-07	-5.11229E-08	-7.29307E-06	1.95394E-07	1.21392E-06	-2.51934E-06	3.71951E-07	1.36397E-06	-9.04106E-08	2.52248E-07	1.8507E-06
RMInt-Inc-15	-4.61693E-06	1.55478E-07	-1.62638E-07	-7.00782E-06	3.24577E-07	1.03684E-06	-2.7883E-06	2.54288E-07	1.22628E-06	3.54519E-07	2.81962E-08	1.9504E-06
RMInt-Inc-16	-4.70982E-06	2.50101E-07	-7.89767E-08	-7.33816E-06	1.79368E-07	7.36939E-07	-0.00000298	7.70512E-08	1.21431E-06	4.03769E-07	6.73029E-08	1.90971E-06
RMInt-Inc-17	-4.44884E-06	1.30532E-07	-1.97772E-07	-7.11499E-06	5.86566E-08	1.07556E-06	-2.76576E-06	4.31905E-07	1.18845E-06	3.88916E-07	1.63736E-07	0.000001934
RMInt-Inc-18	-4.42152E-06	2.27672E-07	-5.53127E-07	-7.58745E-06	1.3725E-07	8.80139E-07	-2.74613E-06	3.45236E-07	1.14925E-06	-1.25587E-07	2.34244E-07	1.92487E-06
RMInt-Inc-19	-4.45085E-06	1.07069E-07	-2.12309E-07	-7.30242E-06	2.20367E-07	1.07698E-06	-2.94141E-06	5.06033E-07	1.00802E-06	8.93518E-08	6.88735E-07	1.8886E-06
RMInt-Inc-2	-4.63315E-06	1.23546E-07	-1.11364E-07	-7.21809E-06	2.28766E-07	1.03896E-06	-2.82349E-06	-4.00936E-08	1.1291E-06	2.67529E-07	-8.55913E-08	1.9626E-06
RMInt-Inc-20	-4.53712E-06	1.43628E-07	-3.00028E-07	-7.17156E-06	1.87083E-07	7.44556E-07	-2.98643E-06	4.23555E-07	9.4286E-07	3.95798E-07	4.15945E-08	1.87625E-06
RMInt-Inc-21	-4.70502E-06	1.91879E-07	-9.95312E-08	-7.31788E-06	5.66382E-07	4.89903E-07	-2.7761E-06	-6.83835E-09	1.12793E-06	-1.46564E-08	1.32513E-07	1.88441E-06
RMInt-Inc-22	-4.44698E-06	1.1541E-07	1.97256E-07	-6.84347E-06	3.04484E-07	9.27047E-07	-3.0277E-06	2.51616E-07	1.1996E-06	3.98879E-08	-9.89293E-08	1.87359E-06
RMInt-Inc-23	-4.49186E-06	7.59605E-08	-1.75345E-07	-6.96614E-06	3.55084E-07	8.74308E-07	-2.96304E-06	2.97177E-07	1.03231E-06	1.08046E-07	3.22664E-07	1.84291E-06
RMInt-Inc-24	-4.56659E-06	1.77309E-07	-2.85414E-08	-7.15071E-06	7.23147E-08	7.40995E-07	-3.17153E-06	2.36272E-07	1.05295E-06	2.73791E-07	2.22243E-08	1.91848E-06
RMInt-Inc-25	-4.85805E-06	1.36813E-07	7.60394E-08	-7.14807E-06	5.10899E-07	7.4088E-07	-3.02722E-06	3.89098E-07	1.1716E-06	2.13447E-08	1.16665E-08	2.23779E-06
RMInt-Inc-3	-4.5488E-06	1.7185E-07	-2.90994E-07	-7.36902E-06	1.45083E-07	1.41605E-06	-2.69193E-06	9.6798E-08	1.29032E-06	4.13409E-07	-2.08869E-07	1.96203E-06
RMInt-Inc-4	-4.6412E-06	1.66288E-07	1.09513E-07	-7.36485E-06	-3.3687E-08	1.35358E-06	-2.84193E-06	3.83367E-07	1.12445E-06	3.85566E-07	1.21027E-07	1.98846E-06
RMInt-Inc-5	-4.64013E-06	2.34635E-07	1.14941E-08	-7.13933E-06	5.46968E-08	1.08037E-06	-2.86564E-06	2.18662E-07	1.20756E-06	2.55778E-07	-4.37509E-09	2.01138E-06
RMInt-Inc-6	-4.28407E-06	-1.91373E-08	-3.13573E-07	-7.12871E-06	4.9499E-07	1.27836E-06	-2.79112E-06	1.26429E-07	1.32384E-06	3.53433E-07	1.25076E-07	1.99266E-06
RMInt-Inc-7	-4.59464E-06	1.69748E-07	-1.65836E-07	-7.10326E-06	3.77262E-08	9.87186E-07	-2.51931E-06	-1.48764E-08	1.24791E-06	1.0026E-06	1.38022E-07	1.84677E-06
RMInt-Inc-8	-4.26482E-06	1.26798E-07	-7.45064E-08	-7.4707E-06	7.97803E-08	1.01268E-06	-2.51195E-06	3.1487E-07	1.16446E-06	1.76642E-07	1.9794E-07	1.89601E-06
RMInt-Inc-9	-4.4146E-06	1.54608E-07	7.13475E-09	-7.44357E-06	2.31502E-07	9.2883E-07	-2.6738E-06	4.62793E-07	1.29039E-06	6.02715E-07	-1.7201E-07	1.85063E-06

Appendix C. Anhysteretic remanent magnetizations

25 microTesla field intensity experiments

Specimen	Anhysteretic Remanent Magnetizations - Am^2											
	RM25-0			RM25-30			RM25-60			RM25-90		
	Mx	My	Mz	Mx	My	Mz	Mx	My	Mz	Mx	My	Mz
RMInt-Inc-1	9.62905E-07	-9.52762E-08	2.14239E-08	1.20632E-06	-4.11321E-08	7.25748E-08	9.87442E-07	7.71975E-09	3.54692E-08	1.32474E-06	-3.59491E-08	4.76423E-08
RMInt-Inc-10	9.86404E-07	-3.10342E-08	-2.8114E-08	1.19098E-06	-6.06296E-08	-3.85755E-09	9.13127E-07	-1.91678E-08	3.20385E-08	1.40559E-06	-4.26724E-08	1.05795E-07
RMInt-Inc-11	9.71842E-07	-3.71817E-08	-2.21023E-08	1.1987E-06	-1.32563E-07	-2.73445E-08	9.77658E-07	-4.57911E-08	2.0617E-08	1.38516E-06	-1.21643E-08	3.39471E-09
RMInt-Inc-12	9.46723E-07	-8.15156E-09	-2.13507E-08	1.23356E-06	-4.89523E-08	1.35357E-09	9.70206E-07	-3.24555E-08	2.16963E-08	1.39939E-06	-3.84998E-08	9.78108E-08
RMInt-Inc-13	9.46831E-07	-3.11506E-08	-4.54774E-09	1.16661E-06	-2.31278E-08	1.37313E-08	8.9161E-07	-4.93597E-08	-2.06514E-08	1.37217E-06	-5.82121E-08	-1.43005E-09
RMInt-Inc-14	9.81245E-07	-4.33615E-08	1.75583E-08	1.15554E-06	-7.79945E-08	-5.58591E-08	9.41007E-07	-5.59284E-08	6.34186E-08	1.46561E-06	-4.11657E-08	4.75276E-08
RMInt-Inc-15	9.97652E-07	-4.00574E-08	-5.34121E-08	1.23223E-06	-1.72837E-08	-3.0866E-09	9.6842E-07	-3.99392E-08	3.68557E-08	1.42604E-06	-5.45499E-08	3.95303E-08
RMInt-Inc-16	9.37682E-07	-1.89439E-08	-1.27611E-08	1.2048E-06	-4.68778E-08	5.95091E-09	9.67642E-07	-9.48154E-08	4.37934E-08	1.31991E-06	-2.67853E-08	5.29129E-08
RMInt-Inc-17	9.2841E-07	-3.79627E-08	-1.29413E-08	1.16446E-06	-2.76449E-08	9.85249E-10	9.27795E-07	-3.48392E-08	7.1978E-09	1.37406E-06	-2.4049E-08	7.79206E-08
RMInt-Inc-18	9.78732E-07	-3.1494E-08	-3.45599E-08	1.15737E-06	-3.89555E-08	-2.84973E-09	9.45647E-07	-5.1943E-08	9.83109E-09	1.38052E-06	-3.60494E-08	5.60197E-08
RMInt-Inc-19	9.8836E-07	-4.71323E-08	-5.28299E-08	1.25644E-06	-3.03171E-08	-2.67617E-08	1.00596E-06	-1.20846E-08	6.8162E-08	1.38133E-06	-3.05859E-08	4.55697E-08
RMInt-Inc-2	1.07064E-06	2.65658E-08	-2.873E-08	1.21184E-06	-1.04174E-07	-2.6584E-08	9.59524E-07	-1.54375E-08	3.48655E-08	1.42758E-06	-5.05709E-08	6.62728E-08
RMInt-Inc-20	1.00012E-06	-1.9192E-08	2.77319E-08	0.000001252	-3.41228E-08	6.5426E-08	1.00979E-06	-3.55908E-08	1.34053E-08	1.32991E-06	-3.26867E-08	5.37671E-08
RMInt-Inc-21	9.18496E-07	-6.00989E-08	-9.83632E-09	1.15703E-06	-1.37108E-08	-1.94778E-08	9.5295E-07	-2.63053E-08	2.41777E-08	1.29427E-06	-2.32934E-08	3.54656E-08
RMInt-Inc-22	1.00309E-06	-1.69095E-08	-1.07733E-08	1.18419E-06	-2.68654E-08	2.43425E-08	9.53678E-07	-2.81748E-08	6.53114E-08	1.33591E-06	-4.17573E-08	2.58276E-08
RMInt-Inc-23	9.91488E-07	-1.79161E-08	-1.16482E-08	1.16496E-06	-7.71354E-08	-4.26209E-08	1.00235E-06	-1.02464E-09	-1.43999E-09	1.33656E-06	3.2323E-09	7.00502E-08
RMInt-Inc-24	1.00354E-06	-4.59984E-09	-9.85675E-09	1.24711E-06	-4.85964E-08	-4.27579E-08	1.02499E-06	-1.42732E-08	7.1613E-08	1.45061E-06	-1.14454E-08	1.41243E-07
RMInt-Inc-25	9.87381E-07	-4.33244E-08	-5.18822E-08	1.16537E-06	-3.9742E-08	-2.58971E-08	9.65146E-07	-3.42358E-08	3.66659E-08	1.35719E-06	-2.07324E-08	4.16717E-08
RMInt-Inc-3	1.00908E-06	-6.89147E-08	4.12151E-09	1.20821E-06	-1.06493E-08	-1.98331E-08	9.60781E-07	-3.49437E-08	4.18894E-08	1.36716E-06	-1.49703E-08	7.99354E-08
RMInt-Inc-4	9.47454E-07	-5.06937E-08	2.8095E-08	1.25454E-06	-5.23493E-08	-1.30762E-08	9.65627E-07	-1.80685E-08	4.04438E-08	1.37041E-06	-1.19667E-08	9.31145E-08
RMInt-Inc-5	9.12081E-07	-4.93191E-08	1.28634E-08	1.18434E-06	-3.61013E-08	6.52199E-08	9.5359E-07	-4.73173E-08	6.44694E-08	1.28515E-06	-7.40526E-08	3.18218E-08
RMInt-Inc-6	9.59656E-07	-8.58845E-09	2.48965E-08	1.15794E-06	-6.4924E-08	4.55699E-08	9.41035E-07	-2.54575E-08	-1.99701E-09	1.39558E-06	-8.8389E-08	3.24448E-08
RMInt-Inc-7	1.00019E-06	-2.86914E-08	-2.3216E-08	1.21158E-06	-1.42989E-07	-9.53697E-09	9.58904E-07	-2.98141E-08	9.43609E-08	1.36902E-06	-4.74669E-08	4.60059E-09
RMInt-Inc-8	9.39761E-07	-1.451E-08	-2.77859E-08	1.21976E-06	-6.47868E-08	-4.57547E-09	9.38788E-07	-2.38661E-08	1.34233E-08	1.32855E-06	-3.09916E-08	1.02576E-07
RMInt-Inc-9	9.34107E-07	-4.40752E-08	-7.49616E-09	1.17106E-06	-3.36461E-08	-3.23455E-08	8.95067E-07	-3.29821E-08	3.37117E-08	1.34755E-06	-1.43416E-07	6.09277E-08

50 microTesla field intensity experiments

Anhysteretic Remanent Magnetizations - Am^2

Specimen	RM50-0			RM50-30			RM50-60			RM50-90c		
	Mx	My	Mz	Mx	My	Mz	Mx	My	Mz	Mx	My	Mz
RMInt-Inc-1	8.23064E-07	-1.73665E-08	3.16306E-08	1.29599E-06	-1.22441E-08	1.25122E-07	1.09853E-06	-1.94058E-08	1.34044E-07	9.43417E-07	-6.20168E-08	-4.61344E-08
RMInt-Inc-10	8.89483E-07	-2.68432E-08	4.43121E-09	1.26464E-06	-6.21536E-08	3.53718E-08	1.03989E-06	-6.73739E-08	1.14595E-07	9.09367E-07	-1.4489E-08	1.79135E-08
RMInt-Inc-11	8.59635E-07	-2.74549E-08	4.4261E-08	1.3015E-06	-1.82543E-08	8.85919E-08	1.09767E-06	-2.46588E-08	1.02855E-07	9.8678E-07	-2.56297E-08	1.34952E-08
RMInt-Inc-12	8.08425E-07	-1.40253E-08	2.69772E-08	1.37404E-06	-2.77517E-08	5.05343E-08	1.18692E-06	7.1337E-08	1.37548E-07	1.01153E-06	-2.19578E-08	1.41514E-08
RMInt-Inc-13	8.2056E-07	-2.40957E-08	3.28674E-08	1.30044E-06	-2.81482E-08	1.15857E-07	0.0000011	-4.3626E-09	6.72987E-08	9.45087E-07	-5.4581E-08	6.40157E-08
RMInt-Inc-14	8.58655E-07	-2.66572E-08	-1.56408E-08	1.20465E-06	-3.15283E-08	8.20508E-08	1.10026E-06	-4.40497E-08	1.17214E-07	9.03056E-07	-9.90736E-08	4.08511E-08
RMInt-Inc-15	8.60864E-07	-1.45749E-08	2.76408E-08	1.31384E-06	-4.36133E-08	6.22535E-08	1.12584E-06	-4.45019E-08	7.17491E-08	9.82859E-07	2.19207E-08	6.96876E-08
RMInt-Inc-16	8.10214E-07	-2.30353E-08	1.64518E-08	1.39134E-06	-2.21837E-08	1.22597E-07	1.09266E-06	-3.23341E-08	1.00961E-07	9.46439E-07	-2.32644E-08	2.9444E-08
RMInt-Inc-17	8.65974E-07	1.45841E-08	4.12721E-08	1.31025E-06	-2.20029E-08	-1.02445E-08	0.000001111	-4.5197E-08	6.97811E-09	9.55914E-07	-4.08878E-08	-3.03591E-09
RMInt-Inc-18	8.65035E-07	-3.52004E-08	2.332E-08	1.2535E-06	-5.55698E-08	6.54873E-08	1.12218E-06	-3.30749E-08	4.05744E-08	9.77601E-07	-7.78788E-08	1.49337E-08
RMInt-Inc-19	8.65324E-07	-3.2884E-08	4.48345E-08	1.25174E-06	-4.74377E-08	6.56367E-08	1.14339E-06	-4.33872E-08	4.97415E-08	9.78295E-07	-3.61316E-08	1.45184E-08
RMInt-Inc-2	8.42028E-07	-3.5355E-08	3.35127E-08	1.28868E-06	-7.0544E-08	7.00383E-08	1.20576E-06	-2.99892E-08	1.18263E-07	1.0017E-06	-4.44996E-08	4.1239E-08
RMInt-Inc-20	7.97041E-07	-2.9638E-08	3.40034E-08	1.33063E-06	-3.56699E-08	3.24454E-08	1.0773E-06	-3.98004E-08	6.48815E-08	9.42356E-07	-1.27918E-08	3.4734E-08
RMInt-Inc-21	8.25021E-07	-1.51823E-08	5.03546E-08	1.26074E-06	-2.4596E-08	1.07617E-07	1.06412E-06	-5.2727E-08	9.32811E-08	9.13659E-07	-5.19904E-08	8.03789E-08
RMInt-Inc-22	8.67068E-07	-8.67557E-09	-4.04506E-08	1.26451E-06	-2.97156E-08	8.37672E-08	1.13772E-06	-4.63599E-10	9.49356E-08	9.75654E-07	-4.02509E-08	9.5511E-08
RMInt-Inc-23	8.63501E-07	-1.48707E-09	1.09002E-08	1.27883E-06	-1.87302E-08	1.07234E-07	1.09621E-06	-9.79576E-09	1.09925E-07	9.99507E-07	-1.67853E-08	8.83413E-08
RMInt-Inc-24	8.4317E-07	-3.73607E-08	3.23542E-09	1.33721E-06	-2.23703E-08	6.41953E-08	1.12873E-06	-4.20875E-08	1.42362E-07	9.68236E-07	-9.08804E-09	5.28148E-08
RMInt-Inc-25	8.28607E-07	-6.00833E-09	5.43764E-08	1.25285E-06	-1.56712E-08	1.09988E-07	1.16075E-06	-3.1693E-08	1.16644E-07	9.9368E-07	-3.51766E-08	5.48406E-08
RMInt-Inc-3	8.40183E-07	-1.36159E-08	9.4932E-09	1.35884E-06	-5.54573E-08	6.06598E-08	1.17003E-06	-3.68199E-08	7.43052E-08	9.95711E-07	-3.05688E-08	2.81561E-08
RMInt-Inc-4	7.96923E-07	-2.8075E-08	2.50827E-08	1.40085E-06	-2.71455E-08	5.06975E-08	1.11285E-06	-3.84053E-08	8.86499E-08	9.74956E-07	-1.47069E-08	8.43923E-09
RMInt-Inc-5	8.42918E-07	-1.4985E-08	5.22999E-08	1.30241E-06	-2.06239E-08	7.78044E-08	1.1029E-06	6.70363E-09	1.10949E-07	9.15043E-07	-2.42754E-08	7.20989E-08
RMInt-Inc-6	8.63485E-07	-2.08769E-08	2.61575E-09	1.24701E-06	-4.72627E-08	7.30445E-08	1.16164E-06	-2.61155E-08	1.37032E-07	9.65168E-07	-3.86618E-08	6.25649E-08
RMInt-Inc-7	8.59459E-07	-1.66627E-08	8.05067E-09	1.33492E-06	-4.50357E-08	6.51582E-08	1.17488E-06	-3.11721E-08	1.17596E-07	9.08527E-07	-2.63517E-08	4.25378E-08
RMInt-Inc-8	7.85816E-07	-2.62982E-08	-8.70142E-09	1.25565E-06	-3.5351E-08	7.10568E-08	1.12853E-06	-4.9762E-08	1.23015E-07	9.38342E-07	-3.14095E-08	6.2444E-08
RMInt-Inc-9	8.17114E-07	-4.14357E-08	3.92246E-08	1.24209E-06	-3.71717E-08	6.41795E-08	1.07992E-06	-4.33205E-08	1.21184E-07	9.3508E-07	-4.3374E-08	3.64386E-08

100 microTesla field intensity experiments.

Anhysteretic Remanent Magnetizations - Am^2

Specimen	RM100-0			RM100-30b			RM100-60			RM100-90b		
	Mx	My	Mz	Mx	My	Mz	Mx	My	Mz	Mx	My	Mz
RMInt-Inc-1	8.48001E-07	-3.33053E-08	1.0673E-08	1.27201E-06	-8.04842E-09	4.07451E-08	8.59571E-07	-4.39081E-08	5.44235E-08	9.4603E-07	5.79471E-09	1.09392E-07
RMInt-Inc-10	8.01524E-07	-4.45403E-08	2.59259E-09	1.37719E-06	-4.18087E-08	5.07372E-08	8.92023E-07	-5.06653E-08	7.53621E-08	1.33731E-06	-3.79743E-08	1.4222E-07
RMInt-Inc-11	8.78208E-07	-2.11594E-08	-2.55163E-09	1.26362E-06	-1.05373E-08	8.11517E-08	9.17864E-07	-2.4925E-08	1.03158E-07	1.39349E-06	-2.3043E-08	1.06994E-07
RMInt-Inc-12	8.842E-07	-2.4059E-08	4.91331E-08	1.35877E-06	-3.10618E-08	1.01888E-07	9.64854E-07	-1.4151E-08	1.12623E-07	1.33883E-06	-7.55209E-08	1.35971E-07
RMInt-Inc-13	7.94024E-07	-1.2278E-08	2.93843E-08	1.30841E-06	-7.24912E-08	8.20553E-08	8.78024E-07	-4.55636E-08	5.72718E-08	1.19582E-06	3.53408E-08	1.17366E-07
RMInt-Inc-14	7.66272E-07	-3.29699E-08	1.12197E-08	1.31127E-06	-5.66448E-08	8.8496E-08	9.64751E-07	-9.13097E-09	7.74164E-08	1.36876E-06	-5.17024E-08	1.4194E-07
RMInt-Inc-15	8.43723E-07	-1.54595E-08	3.50021E-08	1.36891E-06	-2.37748E-08	8.36384E-08	8.98829E-07	-4.21413E-08	6.39659E-08	1.34893E-06	-3.08588E-08	1.62088E-07
RMInt-Inc-16	8.58552E-07	-8.87269E-08	2.41098E-08	1.29455E-06	-4.9722E-08	1.02624E-07	8.79888E-07	-1.40505E-08	9.0547E-08	1.35913E-06	-5.41314E-08	1.25876E-07
RMInt-Inc-17	7.99493E-07	-9.10692E-09	2.9969E-08	1.35705E-06	-5.57573E-08	1.23259E-07	9.18739E-07	-3.62417E-08	5.65688E-08	1.36123E-06	-5.63981E-08	8.26539E-08
RMInt-Inc-18	7.66381E-07	-1.69929E-08	6.93505E-09	1.40799E-06	-6.05322E-08	1.34631E-07	9.62247E-07	-1.71033E-08	9.2075E-08	1.35649E-06	-1.11125E-07	9.71813E-08
RMInt-Inc-19	8.30661E-07	-1.63766E-08	3.60507E-08	1.29868E-06	-2.76174E-08	4.26058E-08	9.40376E-07	-1.03245E-08	9.35757E-08	1.36635E-06	-1.17579E-07	1.54011E-07
RMInt-Inc-2	8.18282E-07	-2.48893E-08	2.78213E-08	1.30733E-06	-3.55517E-08	1.18367E-07	9.63319E-07	-2.38942E-08	8.06376E-08	1.41011E-06	-4.42069E-08	5.09759E-08
RMInt-Inc-20	8.71465E-07	-4.15766E-08	-1.24468E-08	1.37059E-06	-2.09251E-08	6.53542E-08	8.44571E-07	-1.28703E-08	1.02101E-07	1.34911E-06	-4.20453E-08	9.96057E-08
RMInt-Inc-21	8.71153E-07	-3.71547E-08	3.54491E-08	1.29283E-06	-2.0216E-08	9.89965E-08	8.39074E-07	-3.36092E-08	3.21825E-08	1.2667E-06	-3.79257E-08	1.13736E-07
RMInt-Inc-22	8.10935E-07	-4.65762E-09	3.49351E-08	0.000001367	-1.58545E-08	8.32815E-08	9.51017E-07	5.01632E-09	1.07173E-07	1.37283E-06	-4.74887E-08	1.2096E-07
RMInt-Inc-23	7.92696E-07	-1.94842E-08	1.04302E-08	1.30203E-06	-2.69852E-08	3.58311E-08	8.6968E-07	-2.145E-08	5.80569E-08	1.27664E-06	-1.32269E-08	1.07228E-07
RMInt-Inc-24	8.5915E-07	-1.1992E-08	1.04827E-08	1.41601E-06	-2.99182E-08	7.14524E-08	8.63911E-07	-1.53926E-08	9.78107E-08	1.36588E-06	1.44197E-08	1.53308E-07
RMInt-Inc-25	8.91871E-07	5.78425E-09	4.6382E-08	1.28761E-06	-4.96936E-08	4.8682E-08	8.83671E-07	-1.91778E-08	5.88472E-08	1.44348E-06	-7.10871E-08	1.62393E-07
RMInt-Inc-3	8.2424E-07	-5.66908E-09	-1.94369E-08	1.37531E-06	-2.33298E-08	1.26786E-07	9.54279E-07	-2.15676E-08	7.867E-08	1.41413E-06	-2.00546E-08	1.09327E-07
RMInt-Inc-4	8.85058E-07	-1.94778E-08	-4.70133E-08	1.39332E-06	-3.94201E-08	1.63717E-07	8.9282E-07	-6.47966E-09	1.28188E-07	1.32215E-06	-4.70093E-08	1.23925E-07
RMInt-Inc-5	8.52012E-07	-2.97037E-08	3.22154E-08	1.38183E-06	-4.09448E-08	8.87874E-08	8.19865E-07	-3.28248E-08	9.1652E-08	1.30075E-06	-1.18761E-07	1.88773E-07
RMInt-Inc-6	7.17103E-07	-2.80685E-08	-4.58031E-09	1.26926E-06	2.42324E-08	8.74542E-08	9.19358E-07	-2.66945E-08	1.07929E-07	1.39331E-06	-1.13692E-08	1.91714E-07
RMInt-Inc-7	8.35937E-07	-1.59002E-08	-8.3771E-09	1.32867E-06	-4.05055E-08	7.7857E-08	9.68687E-07	-1.99238E-08	2.37241E-08	1.36837E-06	-4.61225E-08	1.18566E-07
RMInt-Inc-8	8.06001E-07	-8.1901E-09	1.91733E-08	1.35334E-06	-3.79078E-08	5.8591E-08	9.00443E-07	-1.71451E-08	9.22966E-08	1.35594E-06	-1.10653E-08	1.56689E-07
RMInt-Inc-9	8.19951E-07	-1.89005E-08	1.91496E-08	1.39234E-06	-2.29435E-08	1.00002E-07	9.1507E-07	-3.07751E-08	8.13592E-08			

Appendix D. Isothermal remanent magnetizations

25 microTesla field intensity experiments

Specimen	Isothermal Remanent Magnetizations - Am^2											
	RM25-0			RM25-30			RM25-60			RM25-90		
	Mx	My	Mz	Mx	My	Mz	Mx	My	Mz	Mx	My	Mz
RMInt-Inc-1	4.35485E-05	-4.27515E-06	-2.97138E-07	4.64022E-05	-4.12163E-06	5.44114E-07	3.79954E-05	-2.81618E-06	4.92532E-07	4.74586E-05	-2.50818E-06	2.21969E-07
RMInt-Inc-10	4.41211E-05	-3.44105E-06	-6.0162E-07	4.69544E-05	-4.05289E-06	-5.7909E-07	3.57337E-05	-3.58359E-06	-1.45781E-06	4.72712E-05	-4.41311E-06	1.15496E-06
RMInt-Inc-11	4.32261E-05	-1.88913E-06	-1.77186E-06	4.50378E-05	-3.75751E-06	-1.79565E-06	3.65975E-05	-3.05082E-06	-1.11019E-06	4.71907E-05	-3.96476E-06	-3.48623E-07
RMInt-Inc-12	4.33925E-05	-3.58941E-07	1.86646E-07	0.000045179	-5.5747E-06	4.41658E-06	3.64581E-05	-3.8763E-06	-6.66571E-07	4.77635E-05	-0.000005655	2.01171E-06
RMInt-Inc-13	0.000043899	4.34477E-06	-3.83171E-07	4.44126E-05	-3.94334E-06	-4.74458E-07	3.54606E-05	-4.04631E-06	1.67343E-06	4.78959E-05	-3.12451E-06	1.33851E-06
RMInt-Inc-14	4.32554E-05	-5.92555E-06	3.87281E-07	4.54301E-05	-4.08295E-06	-7.03885E-07	3.61331E-05	-3.28557E-06	8.68399E-07	4.94746E-05	-3.03918E-06	2.69257E-07
RMInt-Inc-15	4.40018E-05	-2.33264E-06	-2.48376E-06	4.74698E-05	-0.000003323	-9.53976E-07	3.59621E-05	-4.16614E-06	-0.000002217	0.000050047	-2.96762E-06	-1.47628E-07
RMInt-Inc-16	4.30029E-05	-2.66952E-06	-1.87986E-06	4.52592E-05	-4.15158E-06	-5.01926E-07	0.000036642	-4.03599E-06	5.90149E-07	4.93353E-05	-4.0978E-06	-2.02883E-06
RMInt-Inc-17	4.23426E-05	1.59437E-06	-2.05583E-06	4.51252E-05	-3.63198E-06	-7.58487E-07	3.65127E-05	-3.03327E-06	-4.30989E-07	5.02491E-05	-4.03596E-06	-6.65934E-07
RMInt-Inc-18	4.21379E-05	-7.18963E-07	-9.93021E-07	4.45794E-05	-0.000002472	8.88234E-07	3.61392E-05	-3.05655E-06	-1.47482E-06	4.93604E-05	-4.31017E-06	-4.52486E-07
RMInt-Inc-19	4.20966E-05	2.72066E-06	2.6177E-07	4.51141E-05	-3.36383E-06	-1.22076E-06	0.000037106	-3.10159E-06	5.31378E-08	4.91148E-05	-3.14862E-06	-5.70981E-07
RMInt-Inc-2	4.45827E-05	-5.43718E-06	-2.60623E-06	0.000046914	-5.13454E-06	3.48951E-07	3.74592E-05	-2.02687E-06	-3.77822E-07	4.77727E-05	-3.9418E-06	-2.18595E-06
RMInt-Inc-20	4.44856E-05	2.55748E-06	-1.08439E-06	4.62507E-05	3.13986E-07	-7.73638E-07	3.72799E-05	-2.68041E-06	-1.06905E-06	5.02557E-05	-2.71051E-06	8.13153E-07
RMInt-Inc-21	0.000043919	4.54048E-06	1.92555E-07	4.39633E-05	-3.86329E-06	-3.98793E-07	3.56784E-05	-5.5398E-06	1.68906E-07	4.48086E-05	-4.39503E-06	-4.54808E-06
RMInt-Inc-22	4.44154E-05	-1.42618E-06	-6.33203E-07	4.55698E-05	-2.72724E-06	1.22456E-06	3.68904E-05	-1.83128E-06	-1.89285E-07	4.66147E-05	-3.69861E-06	1.51198E-06
RMInt-Inc-23	4.38771E-05	-2.3359E-06	8.42938E-07	4.46327E-05	-2.93736E-06	9.50009E-07	3.66013E-05	-3.17665E-06	-1.63953E-06	4.60332E-05	-3.1912E-06	-1.65211E-07
RMInt-Inc-24	4.55654E-05	9.26601E-07	-1.43693E-06	4.79652E-05	-3.0447E-06	-6.02526E-07	3.77223E-05	-3.59687E-06	1.61112E-06	4.85536E-05	-3.76502E-06	2.82893E-06
RMInt-Inc-25	4.18829E-05	-6.80731E-06	-1.36022E-06	4.66828E-05	1.83181E-07	-2.1396E-06	3.67715E-05	-6.36006E-06	-4.52356E-07	4.96407E-05	-3.16011E-06	-1.01245E-07
RMInt-Inc-3	4.42669E-05	-4.54153E-06	-1.03084E-06	4.42851E-05	-3.95122E-06	-3.773E-07	3.65088E-05	-3.73619E-06	-7.92385E-07	4.61644E-05	-3.82041E-06	-2.17366E-06
RMInt-Inc-4	4.35204E-05	2.31816E-06	5.33849E-07	4.54277E-05	-3.85933E-06	-2.31099E-06	3.66702E-05	-4.98204E-06	-3.00825E-07	4.87308E-05	-4.6059E-06	1.04799E-06
RMInt-Inc-5	4.46071E-05	1.0076E-06	-9.4819E-07	0.000045185	-4.09169E-06	-1.56541E-06	3.77565E-05	-4.41919E-06	-1.02533E-06	4.64715E-05	-4.70384E-06	2.3186E-07
RMInt-Inc-6	4.36625E-05	-2.42727E-07	-1.92942E-06	4.42788E-05	-3.49308E-06	-2.53403E-06	3.64379E-05	-2.7163E-06	-1.81688E-06	4.81534E-05	-3.26366E-06	2.33932E-06
RMInt-Inc-7	4.43221E-05	1.22213E-06	-5.01083E-07	4.36358E-05	-3.74783E-06	9.38556E-07	3.66753E-05	-2.75522E-06	5.11815E-07	4.88238E-05	-4.09243E-06	1.88585E-06
RMInt-Inc-8	4.27323E-05	-3.0661E-06	4.9681E-08	4.53457E-05	-3.96859E-06	-1.3584E-06	3.56673E-05	-3.72758E-06	-1.47603E-06	4.84931E-05	-6.88323E-06	-2.28767E-06
RMInt-Inc-9	4.36172E-05	1.86974E-06	-8.50847E-07	4.52321E-05	-3.56574E-06	1.16373E-07	0.000035776	-2.97766E-06	-4.57678E-07	5.02745E-05	-3.49223E-06	2.21265E-08

50 microTesla field intensity experiments

Isothermal Remanent Magnetizations - Am^2

Specimen	RM50-0			RM50-30			RM50-60			RM50-90c		
	Mx	My	Mz	Mx	My	Mz	Mx	My	Mz	Mx	My	Mz
RMInt-Inc-1	3.65543E-05	-3.12833E-06	-6.48284E-07	4.86325E-05	-3.11349E-06	4.7753E-06	4.64202E-05	-2.13254E-06	-1.90642E-06	3.76119E-05	-3.48802E-06	2.14948E-06
RMInt-Inc-10	3.69339E-05	-3.82241E-06	8.54209E-07	4.82071E-05	-4.8414E-06	-2.98095E-06	4.69576E-05	-3.9209E-06	4.12256E-07	3.63022E-05	2.06486E-06	-9.20629E-07
RMInt-Inc-11	3.61527E-05	-3.62588E-06	2.09904E-06	4.81386E-05	-5.1104E-06	2.11517E-06	4.56736E-05	-3.06855E-06	-1.0995E-06	3.64977E-05	-1.95152E-06	3.61081E-07
RMInt-Inc-12	3.58655E-05	-2.08608E-06	1.26139E-06	5.13931E-05	-3.83203E-06	1.90202E-06	4.78649E-05	-2.86212E-06	-3.34652E-07	3.75643E-05	-5.31951E-07	-1.64017E-06
RMInt-Inc-13	3.58052E-05	-3.3197E-06	8.44544E-07	5.43522E-05	-6.49661E-06	1.12979E-06	4.78238E-05	-2.36535E-06	-4.99087E-06	3.65981E-05	-6.27802E-06	-3.36647E-07
RMInt-Inc-14	3.62227E-05	-3.2039E-06	7.23174E-07	5.50367E-05	-3.88899E-06	6.72933E-07	0.000048672	-2.71057E-06	-1.72772E-06	3.56243E-05	-3.05822E-06	8.27714E-07
RMInt-Inc-15	3.64374E-05	-1.63787E-06	-8.32282E-07	5.65697E-05	-5.34493E-06	2.40301E-06	4.86666E-05	-3.25975E-06	2.47273E-06	3.55267E-05	-9.73656E-06	-1.55858E-06
RMInt-Inc-16	3.54799E-05	-3.46797E-06	1.01147E-06	6.15519E-05	-3.66285E-06	7.75651E-07	0.000044415	-3.40118E-06	-4.22601E-07	3.65291E-05	-0.000001124	8.33013E-07
RMInt-Inc-17	3.75905E-05	-3.0593E-06	1.10527E-06	4.99056E-05	-5.06976E-06	1.79875E-06	4.57863E-05	-3.68008E-06	-1.3659E-06	3.67992E-05	-2.64308E-06	-8.77162E-07
RMInt-Inc-18	3.63342E-05	-3.3253E-06	-2.24761E-07	5.13818E-05	-1.44493E-06	3.07867E-06	4.71227E-05	-3.36374E-06	-1.43777E-06	3.62433E-05	-3.28846E-06	-1.98718E-06
RMInt-Inc-19	3.62079E-05	-3.08444E-06	1.40142E-06	4.94711E-05	-4.99599E-06	1.51685E-06	4.66096E-05	-3.0596E-06	-1.01179E-06	3.81776E-05	-3.68693E-06	3.68952E-07
RMInt-Inc-2	3.55533E-05	-4.28187E-06	-1.3543E-06	5.23951E-05	-5.40639E-06	2.07336E-06	4.87437E-05	-4.17854E-06	8.33037E-07	0.000037544	-5.37678E-06	-3.02252E-07
RMInt-Inc-20	3.57441E-05	-1.89179E-06	3.50917E-07	5.29828E-05	-4.54362E-06	-1.01379E-06	4.64141E-05	-4.34155E-06	1.38088E-06	3.88808E-05	-7.42637E-08	-9.53439E-07
RMInt-Inc-21	3.62211E-05	-2.33741E-06	2.14863E-06	5.60169E-05	-4.58829E-06	2.18383E-06	4.67535E-05	-2.28059E-06	-8.45645E-07	3.76761E-05	-3.45513E-06	9.85712E-07
RMInt-Inc-22	3.63964E-05	-7.7187E-07	1.13772E-06	0.000057839	-4.73219E-06	1.69649E-06	4.87385E-05	-2.70677E-06	-2.90497E-07	3.77072E-05	-3.53945E-06	-3.80716E-07
RMInt-Inc-23	3.62805E-05	-2.83978E-06	-3.68486E-08	5.85308E-05	-5.0995E-06	3.55533E-07	4.62791E-05	-1.09751E-06	2.26252E-06	3.82112E-05	-5.04865E-06	2.47614E-07
RMInt-Inc-24	3.73593E-05	-1.64193E-06	1.79283E-06	6.04612E-05	-4.71706E-06	-1.16891E-06	4.42628E-05	-3.66627E-06	-1.47117E-06	0.000038327	-1.22617E-06	2.15398E-06
RMInt-Inc-25	3.53189E-05	-2.19184E-06	1.68441E-06	4.62807E-05	-3.81838E-06	2.90927E-06	4.97987E-05	-2.39898E-06	2.17737E-06	3.72997E-05	-2.45182E-06	-2.91572E-06
RMInt-Inc-3	3.58383E-05	-3.0716E-06	-9.98497E-07	5.50342E-05	-4.33867E-06	7.80284E-08	4.86015E-05	-3.83955E-06	1.03803E-06	3.69172E-05	-3.36949E-06	-3.29842E-06
RMInt-Inc-4	3.60182E-05	-2.69421E-06	-1.04595E-06	5.94236E-05	-5.22945E-06	2.48442E-06	4.91792E-05	-3.94274E-06	1.84172E-06	3.71718E-05	-1.29454E-06	-2.30277E-06
RMInt-Inc-5	3.68842E-05	-3.1153E-06	1.40796E-06	5.84308E-05	-4.72336E-06	2.92955E-06	4.72742E-05	-3.8263E-06	-7.97012E-07	3.66988E-05	-4.98883E-06	-9.07305E-07
RMInt-Inc-6	3.65041E-05	-2.26897E-06	4.99594E-07	6.01521E-05	-4.23849E-06	1.91115E-06	4.77202E-05	-4.1225E-06	1.51935E-06	3.67753E-05	-1.95408E-06	5.67859E-07
RMInt-Inc-7	3.65444E-05	-3.49944E-06	1.14897E-06	6.22181E-05	-5.25706E-06	5.27396E-07	4.76836E-05	-4.09313E-06	9.37096E-07	3.37971E-05	-4.46726E-06	1.04108E-06
RMInt-Inc-8	0.000035547	-3.5748E-06	-2.08459E-07	5.89869E-05	-3.85546E-06	1.17908E-06	0.000045315	-4.97989E-06	-2.43024E-07	3.65235E-05	-3.18092E-06	1.26046E-06
RMInt-Inc-9	3.57417E-05	-3.37549E-06	3.08524E-07	4.67479E-05	-4.38707E-06	2.66808E-06	4.54496E-05	-4.47495E-06	9.55229E-07	3.66231E-05	-4.10704E-06	-1.06131E-07

100 microTesla field intensity experiments

Isothermal Remanent Magnetizations - Am^2

Specimen	RM100-0			RM100-30b			RM100-60			RM100-90b		
	Mx	My	Mz	Mx	My	Mz	Mx	My	Mz	Mx	My	Mz
RMInt-Inc-1	0.000040777	-2.50731E-06	5.74478E-07	IRM's were not measured for this experiment			3.85537E-05	-3.8398E-06	-2.2438E-06	3.24014E-05	-3.22224E-06	-2.12286E-07
RMInt-Inc-10	4.07047E-05	-3.35049E-06	-8.127E-07				3.90304E-05	-3.74002E-06	-1.06644E-06	0.000052807	-4.28445E-06	2.58757E-06
RMInt-Inc-11	4.22968E-05	-2.93194E-06	-1.61848E-06				3.83265E-05	-2.88232E-06	-2.22273E-07	5.24166E-05	-3.96077E-06	-3.09056E-07
RMInt-Inc-12	4.25705E-05	-3.28031E-06	-3.36291E-07				3.95314E-05	-2.6432E-06	1.16725E-06	5.09713E-05	-4.85684E-06	9.82122E-08
RMInt-Inc-13	3.92997E-05	-3.00241E-06	-3.14864E-08				3.84805E-05	-3.67482E-06	-1.24633E-06	4.59229E-05	-4.39839E-06	-7.73369E-07
RMInt-Inc-14	3.95601E-05	-3.77491E-06	1.34068E-06				3.89042E-05	-2.73351E-06	-1.62977E-06	4.99794E-05	-4.44529E-06	1.05808E-06
RMInt-Inc-15	4.11505E-05	-2.49075E-06	8.76721E-07				3.95951E-05	-3.28365E-06	-1.25964E-06	4.93207E-05	-4.56902E-06	-2.1269E-06
RMInt-Inc-16	4.14213E-05	-4.2058E-06	1.0836E-06				3.88082E-05	-2.98967E-06	6.23412E-07	4.88399E-05	-4.68451E-06	-1.35979E-06
RMInt-Inc-17	4.03297E-05	-3.20498E-06	1.34628E-06				0.000038727	-2.99727E-06	-2.75487E-06	4.70686E-05	-2.95446E-06	-2.45697E-06
RMInt-Inc-18	3.96681E-05	-3.47451E-06	-1.10817E-06				3.87857E-05	-3.04986E-06	-2.37201E-06	5.42774E-05	-3.38723E-06	2.93757E-08
RMInt-Inc-19	4.02938E-05	-3.44724E-06	-7.49061E-07				3.81755E-05	-3.08469E-06	-4.76898E-06	5.52493E-05	-4.73104E-06	1.11883E-06
RMInt-Inc-2	4.12709E-05	-5.40394E-06	-2.12196E-07				3.97426E-05	-3.09986E-06	-1.8382E-06	4.40145E-05	-4.81757E-06	-2.59775E-06
RMInt-Inc-20	4.24312E-05	-3.30125E-06	-1.4608E-06				3.92004E-05	-2.78926E-06	1.37061E-06	5.43105E-05	-5.02755E-06	-1.72714E-06
RMInt-Inc-21	4.19405E-05	-3.24991E-06	2.87995E-07				3.84268E-05	-3.08825E-06	-1.76835E-06	0.0000524	-3.75519E-06	-2.33585E-07
RMInt-Inc-22	4.07029E-05	-2.44394E-06	1.37389E-06				4.00996E-05	-2.22118E-06	-5.68883E-07	5.14375E-05	-4.34058E-06	-1.43274E-06
RMInt-Inc-23	4.08306E-05	-3.21389E-06	-2.29706E-07				3.80501E-05	-2.43669E-06	-1.33189E-06	4.96121E-05	-3.11748E-06	3.15111E-07
RMInt-Inc-24	4.13114E-05	-4.82348E-06	-2.0831E-06				3.92216E-05	-2.9313E-06	-1.63661E-06	5.27633E-05	-4.14466E-06	-1.95066E-06
RMInt-Inc-25	4.02164E-05	-2.47332E-06	-5.25604E-07				3.89186E-05	-2.80249E-06	-3.85265E-07	5.28148E-05	-3.77045E-06	-6.45481E-08
RMInt-Inc-3	3.95488E-05	-4.07558E-06	-8.7655E-08				3.89752E-05	-2.75173E-06	-2.40171E-06	4.74165E-05	-3.86997E-06	-1.18531E-06
RMInt-Inc-4	4.29737E-05	-2.98224E-06	-1.46672E-06				3.85412E-05	-4.34897E-06	1.76978E-07	4.80943E-05	-4.06528E-06	-2.0404E-06
RMInt-Inc-5	4.33584E-05	-2.65079E-06	1.10244E-06				3.93782E-05	-2.94446E-06	-4.48528E-07	4.78666E-05	-4.73836E-06	1.21165E-06
RMInt-Inc-6	3.88499E-05	-2.72229E-06	3.40746E-07				3.88767E-05	-3.24133E-06	4.42949E-07	4.86731E-05	-3.31957E-06	2.67718E-07
RMInt-Inc-7	4.09281E-05	-2.42553E-06	1.86656E-06				0.00003924	-3.03765E-06	-1.00497E-06	5.01283E-05	-6.04411E-06	-9.46155E-07
RMInt-Inc-8	3.87787E-05	-3.33912E-06	8.13802E-07				0.000038001	-3.83603E-06	5.09189E-07	5.23072E-05	-3.54783E-06	1.13503E-06
RMInt-Inc-9	4.06648E-05	-3.41925E-06	9.86543E-07				3.90996E-05	-3.47421E-06	-2.19807E-06			

Appendix E. Anisotropy of anhysteretic remanent magnetization

Depositional conditions: 25 μT, 0° Inclination

	Tensor elements (upper half of symmetrical 3x3 matrix)					
Specimen_ID	kxx	kyy	kzz	kxy	kyz	kzx
RM25-0-1	2.30544E-06	2.20374E-06	1.84074E-06	2.85366E-08	1.67435E-08	-7.36256E-09
RM25-0-10	2.32186E-06	2.23094E-06	1.86636E-06	1.52343E-08	-3.37252E-09	-1.57412E-08
RM25-0-11	2.40608E-06	2.33426E-06	1.96448E-06	2.45754E-08	6.43533E-09	-1.81297E-08
RM25-0-12	2.33657E-06	2.26748E-06	1.86485E-06	2.28831E-08	9.26771E-09	3.47022E-09
RM25-0-13	2.24271E-06	2.16454E-06	1.79281E-06	2.10723E-08	-1.0608E-08	2.93911E-08
RM25-0-14	2.23795E-06	2.15153E-06	1.77937E-06	1.57284E-08	-2.96606E-08	-9.44862E-09
RM25-0-15	2.34623E-06	2.26301E-06	1.87465E-06	2.0113E-08	-1.56353E-08	-5.40957E-09
RM25-0-16	2.35068E-06	2.26801E-06	1.8812E-06	1.87059E-08	-5.6724E-09	1.80988E-08
RM25-0-17	2.2845E-06	2.19068E-06	1.86433E-06	5.76907E-09	5.13383E-09	1.10807E-08
RM25-0-18	2.39376E-06	2.2926E-06	1.96724E-06	2.08778E-08	-2.04661E-08	4.07037E-09
RM25-0-19	2.39318E-06	2.31611E-06	1.91652E-06	1.96988E-08	-3.30729E-08	1.63502E-09
RM25-0-2	2.45043E-06	2.33054E-06	1.95741E-06	2.31467E-08	-1.82326E-08	-2.78441E-08
RM25-0-20	2.3925E-06	2.30985E-06	1.87532E-06	3.26589E-08	-5.60819E-08	3.4751E-09
RM25-0-21	2.32428E-06	2.21831E-06	1.89417E-06	3.3952E-08	3.24768E-08	-7.09979E-09
RM25-0-22	2.35817E-06	2.26621E-06	1.93013E-06	1.35116E-08	1.84384E-08	-6.78504E-09
RM25-0-23	2.36249E-06	2.26514E-06	1.87438E-06	1.52016E-08	-2.97774E-09	1.735E-08
RM25-0-24	2.2401E-06	2.17875E-06	1.71246E-06	-5.65826E-09	-2.74795E-08	2.3301E-08
RM25-0-25	2.33847E-06	2.24574E-06	1.87096E-06	5.57426E-08	-9.43932E-09	4.00042E-08
RM25-0-3	2.34511E-06	2.2653E-06	1.90849E-06	2.51591E-08	-1.24282E-08	3.20837E-09
RM25-0-4	2.29892E-06	2.23084E-06	1.88087E-06	2.49256E-08	-9.72951E-09	-1.69538E-08
RM25-0-5	2.27231E-06	2.19826E-06	1.7958E-06	2.27613E-08	-3.25516E-09	1.24387E-09
RM25-0-6	2.38059E-06	2.3008E-06	1.91182E-06	1.35666E-08	-9.84038E-09	2.3823E-08
RM25-0-7	2.34334E-06	2.25253E-06	1.85385E-06	1.6232E-08	-2.21402E-08	2.16465E-08
RM25-0-8	2.25905E-06	2.17556E-06	1.83295E-06	1.178E-08	-1.81228E-08	1.74069E-09
RM25-0-9	2.25258E-06	2.16768E-06	1.86931E-06	1.87258E-08	-4.06896E-09	-2.92805E-09

25 μT, 30° Inclination

Tensor elements (upper half of symmetrical 3x3 matrix)

Specimen_ID	kxx	kyy	kzz	kxy	kyz	kzx
RM25-30-1	2.14362E-06	2.09602E-06	1.68475E-06	2.93945E-08	1.66251E-08	9.66286E-09
RM25-30-10	1.90697E-06	1.85898E-06	1.50141E-06	5.84046E-09	3.19909E-08	-1.03078E-08
RM25-30-11	2.0764E-06	2.03202E-06	1.66116E-06	1.66073E-08	2.61115E-08	-1.19706E-08
RM25-30-12	2.06903E-06	2.01311E-06	1.62065E-06	2.51469E-08	9.20335E-09	4.74516E-09
RM25-30-13	1.98463E-06	1.92258E-06	1.52393E-06	2.82027E-08	9.0516E-09	1.03429E-08
RM25-30-14	1.88147E-06	1.8114E-06	1.50328E-06	1.57674E-08	-3.58623E-09	-6.90078E-09
RM25-30-15	2.09171E-06	2.03652E-06	1.64839E-06	1.41529E-08	5.33366E-09	9.16947E-09
RM25-30-16	2.05042E-06	1.97093E-06	1.56874E-06	1.16312E-08	-4.83592E-09	3.78164E-09
RM25-30-17	2.03663E-06	1.95939E-06	1.55402E-06	1.40499E-08	-3.50897E-09	8.944E-09
RM25-30-18	1.94572E-06	1.87305E-06	1.58546E-06	3.22241E-08	-5.44623E-09	3.42723E-09
RM25-30-19	1.98932E-06	1.92237E-06	1.5742E-06	3.56838E-08	-4.50288E-09	-3.47556E-09
RM25-30-2	1.97459E-06	1.94135E-06	1.55864E-06	1.40205E-08	-1.09266E-08	7.4826E-10
RM25-30-20	2.09743E-06	2.03258E-06	1.66037E-06	3.12584E-08	-2.05336E-08	-8.53387E-09
RM25-30-21	2.06421E-06	1.9997E-06	1.58921E-06	3.2616E-08	-5.40725E-09	-1.9262E-09
RM25-30-22	2.0008E-06	1.96313E-06	1.58522E-06	2.57651E-08	-1.91036E-08	7.62576E-11
RM25-30-23	2.30369E-06	2.24517E-06	1.83539E-06	1.61186E-08	-2.46259E-08	1.09642E-08
RM25-30-24	2.17134E-06	2.1093E-06	1.73648E-06	1.18973E-08	-1.13411E-08	1.54786E-08
RM25-30-25	2.03395E-06	1.97498E-06	1.55913E-06	8.24856E-09	-5.63858E-09	1.35478E-08
RM25-30-3	2.04773E-06	1.99673E-06	1.59224E-06	1.83304E-08	1.92847E-09	-2.60377E-09
RM25-30-4	1.9918E-06	1.93551E-06	1.56991E-06	1.75853E-08	-2.10865E-08	-8.33027E-09
RM25-30-5	2.04898E-06	1.98153E-06	1.61789E-06	1.80726E-08	-7.26244E-09	-5.8163E-09
RM25-30-6	1.98088E-06	1.95442E-06	1.60203E-06	1.66976E-08	-1.49021E-08	8.29285E-09
RM25-30-7	2.03624E-06	1.99275E-06	1.61039E-06	2.42284E-08	-1.27842E-08	4.81891E-09
RM25-30-8	2.0413E-06	1.97882E-06	1.59511E-06	2.64058E-08	-2.81938E-08	-2.48883E-10
RM25-30-9	1.89819E-06	1.80877E-06	1.48699E-06	2.53383E-08	-1.77999E-08	6.05136E-09

25 μT, 60° Inclination

Tensor elements (upper half of symmetrical 3x3 matrix)

Specimen_ID	kxx	kyy	kzz	kxy	kyz	kzx
RM25-60-1	2.28436E-06	2.21586E-06	1.73351E-06	5.47697E-08	-4.90138E-08	3.92515E-08
RM25-60-10	2.25837E-06	2.19509E-06	1.8266E-06	-1.57205E-08	4.52702E-09	2.16804E-08
RM25-60-11	2.45218E-06	2.38141E-06	1.9382E-06	-9.91229E-09	-3.52626E-10	1.54338E-08
RM25-60-12	2.40267E-06	2.29912E-06	1.89429E-06	-7.00265E-09	2.29893E-08	1.74757E-08
RM25-60-13	2.31898E-06	2.23969E-06	1.76148E-06	-4.43192E-09	4.79363E-09	2.87489E-08
RM25-60-14	2.10234E-06	2.0898E-06	1.71287E-06	5.55847E-09	-6.23069E-09	2.44867E-08
RM25-60-15	2.38418E-06	2.36491E-06	1.91394E-06	3.09403E-10	1.52641E-08	1.57804E-08
RM25-60-16	2.38849E-06	2.36398E-06	1.88118E-06	-3.62564E-09	-8.18215E-09	2.76755E-09
RM25-60-17	2.29362E-06	2.27215E-06	1.81872E-06	-4.36582E-09	1.06735E-09	-8.17932E-10
RM25-60-18	2.11197E-06	2.0567E-06	1.67794E-06	1.5248E-08	-3.60818E-09	-1.92031E-08
RM25-60-19	2.19065E-06	2.14243E-06	1.72493E-06	2.97682E-08	8.18904E-09	2.71726E-08
RM25-60-2	2.25131E-06	2.18363E-06	1.77128E-06	2.46234E-08	4.97108E-09	-4.8209E-09
RM25-60-20	2.29747E-06	2.23632E-06	1.79136E-06	1.7449E-08	-1.08298E-08	1.08741E-09
RM25-60-21	2.30395E-06	2.22633E-06	1.78866E-06	1.23748E-08	3.4885E-09	-5.81439E-09
RM25-60-22	2.22549E-06	2.16976E-06	1.77863E-06	2.42326E-08	-1.03822E-08	-7.35057E-10
RM25-60-23	2.15663E-06	2.09834E-06	1.69526E-06	2.05843E-08	-2.32267E-08	-1.28647E-09
RM25-60-24	2.24833E-06	2.19725E-06	1.73452E-06	1.60355E-08	-2.72403E-08	2.91986E-08
RM25-60-25	2.30306E-06	2.26688E-06	1.78018E-06	7.24996E-09	-2.73813E-08	1.8535E-08
RM25-60-3	2.31119E-06	2.26647E-06	1.81755E-06	2.78531E-08	1.37869E-09	1.32618E-09
RM25-60-4	2.36844E-06	2.33949E-06	1.84058E-06	1.84639E-08	-1.18182E-08	2.26282E-09
RM25-60-5	2.17016E-06	2.1315E-06	1.64339E-06	1.55807E-08	-5.73642E-09	1.3841E-08
RM25-60-6	2.28541E-06	2.24945E-06	1.84767E-06	8.92438E-09	-8.85757E-09	8.3343E-09
RM25-60-7	2.35906E-06	2.29337E-06	1.91043E-06	1.52695E-08	-9.08707E-10	4.43692E-09
RM25-60-8	2.30914E-06	2.25798E-06	1.85707E-06	2.3531E-08	-1.49108E-09	1.07544E-10
RM25-60-9	2.26912E-06	2.20828E-06	1.82135E-06	3.08465E-08	-1.22843E-08	7.06866E-09

25 μT, 90° Inclination

Tensor elements (upper half of symmetrical 3x3 matrix)

Specimen_ID	kxx	kyy	kzz	kxy	kyz	kzx
RM25-90b-1	2.06868E-06	2.00491E-06	1.61179E-06	3.62881E-08	-6.8678E-09	-8.85195E-09
RM25-90b-10	1.94802E-06	1.89071E-06	1.52402E-06	6.93816E-09	1.10685E-08	8.72243E-10
RM25-90b-11	2.20127E-06	2.17061E-06	1.76086E-06	-2.40795E-09	8.40588E-09	-8.70529E-09
RM25-90b-12	1.80514E-06	1.79127E-06	1.43437E-06	-1.77589E-09	-1.17613E-08	-1.7895E-08
RM25-90b-13	1.91265E-06	1.85141E-06	1.6025E-06	4.46918E-08	-9.63001E-10	1.17596E-09
RM25-90b-14	2.06659E-06	1.99861E-06	1.74407E-06	3.3413E-08	-4.07293E-09	7.17025E-09
RM25-90b-15	2.06857E-06	2.00726E-06	1.74794E-06	2.64678E-08	-5.14675E-09	9.92971E-09
RM25-90b-16	2.1477E-06	2.11629E-06	1.82652E-06	1.97144E-08	5.13399E-09	2.05827E-08
RM25-90b-17	1.97804E-06	1.88837E-06	1.67142E-06	5.0787E-08	-1.47622E-09	2.84527E-08
RM25-90b-18	2.12863E-06	2.0506E-06	1.78499E-06	2.68187E-08	-8.61043E-09	2.9105E-08
RM25-90b-19	2.19625E-06	2.09486E-06	1.82393E-06	2.41573E-08	-7.46143E-09	1.56704E-08
RM25-90b-2	2.01358E-06	1.97165E-06	1.58235E-06	2.29745E-08	-1.25407E-08	-2.21112E-09
RM25-90b-20	2.07033E-06	1.99251E-06	1.7219E-06	-8.79526E-09	-1.15579E-08	1.34115E-08
RM25-90b-21	2.27497E-06	2.19736E-06	1.77766E-06	2.74339E-08	6.06983E-11	1.54496E-08
RM25-90b-22	2.15906E-06	2.21872E-06	1.71362E-06	2.11235E-08	1.77282E-08	-1.92236E-08
RM25-90b-23	2.25268E-06	2.22115E-06	1.8417E-06	2.81417E-08	-1.80207E-08	-6.39953E-09
RM25-90b-24	2.04988E-06	1.92874E-06	1.64779E-06	2.75055E-08	-4.81808E-08	7.23832E-09
RM25-90b-25	2.18963E-06	2.14229E-06	1.72627E-06	3.64E-08	3.04691E-08	9.07403E-09
RM25-90b-3	2.08198E-06	2.04718E-06	1.66573E-06	6.46354E-09	-6.4503E-09	-8.53156E-09
RM25-90b-4	1.85385E-06	1.82463E-06	1.47244E-06	-1.25856E-08	-3.58194E-09	-6.94135E-09
RM25-90b-5	1.99503E-06	1.93519E-06	1.59318E-06	4.48338E-09	-7.63682E-09	-5.9843E-09
RM25-90b-6	2.08807E-06	2.03806E-06	1.64092E-06	1.98648E-08	-4.83708E-09	2.85779E-09
RM25-90b-7	2.1696E-06	2.11685E-06	1.72166E-06	1.31994E-08	-1.11442E-08	1.85846E-09
RM25-90b-8	1.92041E-06	1.8876E-06	1.47146E-06	1.42513E-08	-7.80166E-09	-9.11919E-09
RM25-90b-9	1.86587E-06	1.80462E-06	1.45984E-06	1.40758E-08	1.68916E-09	9.59001E-09

50 μT, 0° Inclination

Tensor elements (upper half of symmetrical 3x3 matrix)

Specimen_ID	kxx	kyy	kzz	kxy	kyz	kzx
RM50-0-1	2.20777E-06	2.07888E-06	1.76031E-06	2.82956E-08	-7.85742E-09	7.42804E-09
RM50-0-10	2.36295E-06	2.26956E-06	1.83785E-06	-8.91521E-08	-2.6213E-10	1.57423E-08
RM50-0-11	2.43236E-06	2.36144E-06	1.94292E-06	-9.0717E-08	-1.90525E-08	2.69602E-08
RM50-0-12	2.22851E-06	2.1924E-06	1.77118E-06	-8.11215E-08	-1.05689E-08	2.48313E-08
RM50-0-13	2.33584E-06	2.19185E-06	1.8531E-06	-5.92021E-08	-7.15205E-09	1.81595E-08
RM50-0-14	2.32076E-06	2.2233E-06	1.86957E-06	-4.36414E-08	-1.57543E-08	2.01262E-08
RM50-0-15	2.31627E-06	2.23057E-06	1.85897E-06	-1.82252E-08	1.73238E-08	2.38437E-08
RM50-0-16	2.25284E-06	2.20321E-06	1.8338E-06	2.26091E-08	-8.17703E-09	1.08388E-08
RM50-0-17	2.25711E-06	2.19176E-06	1.82128E-06	2.85638E-08	-1.92211E-09	2.15493E-08
RM50-0-18	2.2282E-06	2.15647E-06	1.80581E-06	2.32513E-08	-6.69348E-09	6.31947E-09
RM50-0-19	2.37699E-06	2.29179E-06	1.95523E-06	1.62096E-08	-1.87008E-08	3.44943E-08
RM50-0-2	2.36226E-06	2.27094E-06	1.9568E-06	2.40239E-08	4.54725E-09	2.91733E-09
RM50-0-20	2.29124E-06	2.20023E-06	1.86553E-06	1.97994E-08	-2.32697E-08	2.32693E-08
RM50-0-21	2.28109E-06	2.21966E-06	1.80233E-06	1.65789E-08	-1.68072E-08	4.38176E-08
RM50-0-22	2.33011E-06	2.24805E-06	1.91382E-06	2.83393E-08	5.74584E-09	3.09583E-08
RM50-0-23	2.36513E-06	2.28141E-06	1.95534E-06	2.04091E-08	1.74865E-08	2.98316E-08
RM50-0-24	2.24394E-06	2.14194E-06	1.84218E-06	2.71812E-08	5.36193E-09	8.38418E-09
RM50-0-25	2.33053E-06	2.06546E-06	1.68427E-06	7.09852E-08	-2.77914E-07	7.55347E-08
RM50-0-3	2.30135E-06	2.21545E-06	1.91924E-06	1.52291E-08	-6.00379E-09	-2.18243E-08
RM50-0-4	2.13099E-06	2.10329E-06	1.80006E-06	1.13677E-08	-1.28889E-08	-8.3587E-09
RM50-0-5	2.20684E-06	2.09441E-06	1.78348E-06	2.23888E-08	-1.02469E-08	1.21789E-08
RM50-0-6	2.32026E-06	2.21731E-06	1.91095E-06	2.05503E-08	-1.56822E-08	2.12879E-08
RM50-0-7	2.31837E-06	2.23027E-06	1.8876E-06	2.39191E-08	-1.19029E-08	9.2855E-09
RM50-0-8	2.28153E-06	2.19308E-06	1.84893E-06	3.11664E-08	-5.4569E-09	1.51712E-08
RM50-0-9	2.26814E-06	2.15611E-06	1.84751E-06	6.34755E-08	-1.71593E-08	6.6183E-09

50 μT, 30° Inclination

Tensor elements (upper half of symmetrical 3x3 matrix)

Specimen_ID	kxx	kyy	kzz	kxy	kyz	kzx
RM50-30-1	2.31992E-06	2.28393E-06	1.87576E-06	-9.34322E-10	5.91919E-09	-2.12737E-09
RM50-30-10	2.36629E-06	2.29237E-06	1.91522E-06	2.07088E-08	-1.73652E-08	6.48157E-09
RM50-30-11	2.43295E-06	2.35042E-06	1.96382E-06	2.47656E-08	-1.33229E-08	2.06327E-08
RM50-30-12	2.35739E-06	2.23563E-06	1.86951E-06	2.09914E-08	1.2863E-08	1.25808E-09
RM50-30-13	2.31412E-06	2.28683E-06	1.87331E-06	1.82741E-08	-3.54252E-08	-3.81281E-08
RM50-30-14	2.43396E-06	2.30793E-06	1.95779E-06	1.85266E-08	-4.29605E-08	-1.19716E-09
TM50-30-15	2.46109E-06	2.36692E-06	1.99395E-06	2.89097E-08	-3.73688E-08	-3.65685E-09
RM50-30-16	2.27664E-06	2.2214E-06	1.87651E-06	1.70933E-08	-2.18078E-08	2.90304E-08
RM50-30-17	2.39809E-06	2.28097E-06	1.92894E-06	-1.00026E-10	-1.1077E-08	3.37598E-08
RM50-30-18	2.41475E-06	2.32958E-06	1.95874E-06	1.12827E-08	-5.18369E-10	1.8885E-08
RM50-30-19	2.46905E-06	2.38843E-06	1.96119E-06	2.02984E-08	8.48428E-09	4.06672E-08
RM50-30-2	2.41274E-06	2.32914E-06	1.97632E-06	3.20389E-09	-1.37428E-08	7.30958E-10
RM50-30-20	2.28265E-06	2.25593E-06	1.85937E-06	4.22112E-08	-8.92268E-09	2.36221E-08
RM50-30-21	2.41137E-06	2.27076E-06	1.96355E-06	2.30352E-08	-1.44928E-08	5.69764E-08
RM50-30-22	2.47141E-06	2.36536E-06	0.000001988	4.35062E-08	-5.63041E-09	2.08348E-08
RM50-30-23	2.46136E-06	2.39031E-06	1.9559E-06	5.33293E-08	4.86457E-09	1.81119E-08
RM50-30-24	2.28871E-06	2.25974E-06	1.8255E-06	7.11129E-08	-3.87742E-09	3.55604E-08
RM50-30-25	2.42533E-06	2.2886E-06	1.90518E-06	7.39014E-08	-3.58806E-09	-2.48803E-08
RM50-30-3	2.44804E-06	2.35686E-06	1.96345E-06	-1.34173E-09	1.41571E-08	5.39885E-09
RM50-30-4	2.36803E-06	2.26479E-06	1.89719E-06	2.44765E-09	-1.57518E-08	-8.93601E-09
RM50-30-5	2.2784E-06	2.22856E-06	1.88791E-06	2.08731E-08	-4.87921E-09	-6.57661E-09
RM50-30-6	2.3841E-06	2.32753E-06	1.94898E-06	2.38309E-08	-9.31318E-09	1.12037E-08
RM50-30-7	2.39479E-06	2.33045E-06	1.95135E-06	2.39859E-08	-9.65013E-09	8.34111E-09
RM50-30-8	2.36292E-06	2.27532E-06	1.87167E-06	1.79735E-08	-1.11837E-08	-5.0748E-09
RM50-30-9	2.2819E-06	2.23531E-06	1.90604E-06	2.67208E-08	-1.59629E-08	2.86427E-08

50 μT, 60° Inclination

Tensor elements (upper half of symmetrical 3x3 matrix)

Specimen_ID	kxx	kyy	kzz	kxy	kyz	kzx
RM50-60-1	2.04104E-06	1.99478E-06	1.69926E-06	2.3323E-08	-1.15393E-08	-4.53585E-09
RM50-60-10	2.08677E-06	2.05352E-06	1.65212E-06	-9.25759E-09	5.97422E-09	-1.53797E-08
RM50-60-11	2.24293E-06	0.000002185	1.80704E-06	8.47341E-09	1.28837E-09	-9.69621E-10
RM50-60-12	1.94771E-06	1.89646E-06	1.5256E-06	5.09334E-09	1.86685E-09	-8.76588E-10
RM50-60-13	1.94506E-06	1.86953E-06	1.58973E-06	2.58711E-08	1.02275E-08	1.08433E-08
RM50-60-14	1.96461E-06	1.90572E-06	1.55209E-06	2.65612E-08	-2.51455E-09	1.95096E-08
RM50-60-15	2.16943E-06	0.000002123	1.73774E-06	1.71448E-08	5.35109E-09	7.31047E-09
RM50-60-16	2.10667E-06	2.05671E-06	1.69398E-06	2.86639E-08	-3.02617E-08	4.62506E-09
RM50-60-17	2.09855E-06	0.000002034	1.66689E-06	2.56848E-08	2.87848E-10	1.21014E-08
RM50-60-18	2.32243E-06	2.24873E-06	1.89828E-06	9.089E-09	5.76516E-09	2.01301E-10
RM50-60-19	2.12507E-06	2.07922E-06	1.70579E-06	1.20515E-08	-3.32894E-09	1.04835E-08
RM50-60-2	1.97279E-06	1.92763E-06	1.58925E-06	1.46262E-08	4.48804E-09	7.50602E-09
RM50-60-20	2.22601E-06	2.18775E-06	1.82797E-06	9.0208E-09	-1.29982E-08	1.36401E-08
RM50-60-21	2.12655E-06	2.07958E-06	1.7129E-06	1.30047E-08	-8.47852E-10	-5.11322E-09
RM50-60-22	2.36403E-06	2.29888E-06	1.9458E-06	2.6769E-08	9.25244E-09	-2.17188E-09
RM50-60-23	2.28524E-06	2.22319E-06	1.87087E-06	3.45841E-08	-7.47476E-09	5.14145E-09
RM50-60-24	1.81833E-06	1.75995E-06	1.47347E-06	4.07606E-08	-2.60221E-09	1.29135E-08
RM50-60-25	1.92752E-06	0.00000187	1.49075E-06	3.52034E-09	-1.11597E-08	4.20832E-08
RM50-60-3	2.0176E-06	1.97259E-06	1.60144E-06	2.53475E-08	-5.39533E-09	2.49374E-09
RM50-60-4	2.21023E-06	2.17874E-06	1.79571E-06	3.26738E-08	-1.75878E-08	2.02057E-08
RM50-60-5	2.05662E-06	2.02225E-06	1.62525E-06	2.24266E-08	3.47044E-09	9.09176E-09
RM50-60-6	2.04043E-06	1.99283E-06	1.6156E-06	2.4164E-08	-1.56807E-08	6.22632E-09
RM50-60-7	2.22628E-06	2.16561E-06	1.81634E-06	2.68477E-08	4.26013E-09	2.5499E-09
RM50-60-8	1.89475E-06	1.83596E-06	1.52428E-06	1.58881E-08	-6.51929E-09	2.43637E-09
RM50-60-9	2.00559E-06	1.9403E-06	1.61621E-06	1.86134E-08	-1.03524E-08	9.3638E-09

50 μT, 90° Inclination

Tensor elements (upper half of symmetrical 3x3 matrix)

Specimen_ID	kxx	kyy	kzz	kxy	kyz	kzx
RM50-90c-1	2.2761E-06	2.20487E-06	1.89509E-06	2.20574E-08	-4.44388E-08	-1.91805E-08
RM50-90c-10	2.32787E-06	2.24908E-06	1.93539E-06	2.94708E-08	3.98375E-08	-3.03007E-08
RM50-90c-11	2.34473E-06	2.29896E-06	1.98913E-06	3.60644E-08	-2.02491E-08	-6.94989E-09
RM50-90c-12	2.06605E-06	2.03611E-06	1.67154E-06	2.61498E-08	-2.13924E-08	-6.7035E-09
RM50-90c-13	2.17592E-06	2.09163E-06	1.83022E-06	-9.53856E-09	4.27154E-09	1.30334E-08
RM50-90c-14	2.38791E-06	2.35062E-06	1.98143E-06	8.60058E-09	7.71636E-09	2.96538E-09
RM50-90c-15	2.28037E-06	2.25446E-06	1.94583E-06	8.19244E-09	2.2084E-09	5.54458E-09
RM50-90c-16	2.25876E-06	2.25837E-06	1.93098E-06	8.87999E-09	6.28491E-10	2.20453E-08
RM50-90c-17	2.24686E-06	2.18703E-06	1.87974E-06	2.68588E-08	2.17965E-08	-1.67485E-08
RM50-90c-18	2.33299E-06	2.26971E-06	1.96371E-06	2.20012E-08	2.29937E-09	-5.72173E-09
RM50-90c-19	2.36151E-06	2.31427E-06	1.95848E-06	1.37556E-08	-7.69826E-09	-8.29563E-10
RM50-90c-2	2.29683E-06	2.2593E-06	1.90238E-06	1.17645E-08	-1.93731E-08	-8.02133E-09
RM50-90c-20	2.16655E-06	2.14332E-06	1.80138E-06	1.25248E-08	-2.73765E-08	1.28408E-08
RM50-90c-21	2.19242E-06	2.13818E-06	1.87804E-06	-4.21031E-10	-7.8953E-09	-2.68807E-08
RM50-90c-22	2.27356E-06	2.23149E-06	1.89633E-06	6.40563E-09	-1.14482E-08	9.2729E-09
RM50-90c-23	2.39908E-06	2.33181E-06	2.01235E-06	1.2324E-08	-9.7946E-09	1.91014E-08
RM50-90c-24	2.30775E-06	2.22659E-06	1.8922E-06	1.08135E-08	-2.05632E-08	-6.66104E-09
RM50-90c-25	2.31166E-06	2.26119E-06	1.93511E-06	2.703E-08	-1.29496E-08	7.45338E-09
RM50-90c-3	2.34192E-06	2.2797E-06	1.91867E-06	3.55568E-09	-3.61956E-08	-5.88483E-09
RM50-90c-4	2.17212E-06	2.15466E-06	1.80068E-06	-9.75294E-09	-1.60326E-08	-3.47634E-09
RM50-90c-5	2.27779E-06	2.17679E-06	1.86102E-06	4.64904E-08	-3.44237E-08	7.88967E-09
RM50-90c-6	2.3266E-06	2.25943E-06	1.91343E-06	3.74736E-08	-2.02145E-08	4.40011E-09
RM50-90c-7	2.34292E-06	2.26344E-06	1.9175E-06	1.76627E-08	-2.48715E-08	-1.65909E-08
RM50-90c-8	2.29804E-06	2.26294E-06	1.8598E-06	1.93459E-08	1.19208E-08	1.57325E-08
RM50-90c-9	2.11708E-06	2.03923E-06	1.75228E-06	3.19037E-08	-7.78016E-09	-9.56069E-09

100 μT, 0° Inclination

Tensor elements (upper half of symmetrical 3x3 matrix)

Specimen_ID	kxx	kyy	kzz	kxy	kyz	kzx
RM100-0-1	2.28222E-06	2.13988E-06	1.77513E-06	3.70914E-08	-3.54315E-08	1.11717E-08
RM100-0-10	2.37982E-06	2.27862E-06	1.93331E-06	4.89927E-08	-1.10473E-08	1.76795E-08
RM100-0-11	2.30073E-06	2.21346E-06	1.87898E-06	2.86569E-08	-9.64072E-09	4.58126E-08
RM100-0-12	2.27515E-06	2.14028E-06	1.78103E-06	3.6313E-08	-1.70296E-08	3.28824E-08
RM100-0-13	2.25679E-06	2.18799E-06	1.92143E-06	2.21549E-08	1.36765E-09	3.32225E-08
RM100-0-14	2.31161E-06	2.25442E-06	1.93544E-06	3.13065E-08	-2.02867E-08	2.06269E-08
RM100-0-15	2.38636E-06	2.31326E-06	1.97357E-06	3.4018E-08	-3.91262E-08	3.56723E-08
RM100-0-16	2.3585E-06	2.18153E-06	1.82233E-06	3.00236E-08	-1.6818E-08	3.28697E-08
RM100-0-17	2.31851E-06	2.2553E-06	1.9079E-06	2.57736E-08	1.38705E-08	3.74605E-08
RM100-0-18	2.40985E-06	2.30408E-06	1.95875E-06	2.67821E-08	1.27236E-09	1.0974E-08
RM100-0-19	2.3861E-06	2.27659E-06	1.86756E-06	2.93111E-08	-1.77674E-08	4.42276E-08
RM100-0-2	2.37505E-06	2.23828E-06	1.88485E-06	2.56596E-08	-9.07031E-09	2.10006E-08
RM100-0-20	2.27403E-06	2.13569E-06	1.81389E-06	2.40835E-08	2.02614E-10	3.97556E-08
RM100-0-21	2.38785E-06	2.37128E-06	1.92785E-06	6.75019E-08	3.89134E-08	2.06128E-08
RM100-0-22	2.26732E-06	2.12698E-06	1.82502E-06	2.15178E-08	-3.43986E-08	2.9009E-08
RM100-0-23	2.31728E-06	2.1897E-06	1.85557E-06	3.32659E-08	-1.45813E-08	2.204E-08
RM100-0-24	2.35517E-06	2.24556E-06	1.90662E-06	1.70667E-08	-7.48637E-09	2.62836E-08
RM100-0-25	2.24151E-06	2.14163E-06	1.71917E-06	1.16044E-08	1.91838E-08	3.80218E-08
RM100-0-3	2.38743E-06	2.24074E-06	1.87104E-06	2.56475E-08	-2.92037E-08	2.67409E-08
RM100-0-4	2.2184E-06	2.15441E-06	1.76904E-06	1.22231E-08	-1.25337E-08	1.69004E-08
RM100-0-5	2.25689E-06	2.18242E-06	1.80456E-06	4.45444E-08	-9.46287E-09	1.38979E-08
RM100-0-6	2.3845E-06	2.27828E-06	1.88103E-06	3.1639E-08	-1.55511E-08	3.14798E-08
RM100-0-7	0.000002433	2.31005E-06	1.92363E-06	2.48591E-08	-1.71648E-08	2.81945E-08
RM100-0-8	2.37344E-06	2.23598E-06	1.86151E-06	2.6283E-08	-8.90333E-09	2.54283E-08
RM100-0-9	2.20183E-06	2.09804E-06	1.79399E-06	3.80402E-08	-6.64219E-09	3.5483E-08

100 μT, 30° Inclination

Tensor elements (upper half of symmetrical 3x3 matrix)

Specimen_ID	kxx	kyy	kzz	kxy	kyz	kzx
RM100-30b-1	2.03515E-06	1.93372E-06	1.55745E-06	3.25045E-08	-2.7821E-09	-3.01495E-09
RM100-30b-10	2.05283E-06	1.93588E-06	1.60997E-06	1.45193E-08	-2.76418E-09	3.181E-08
RM100-30b-11	2.09765E-06	1.98593E-06	1.62312E-06	5.10226E-09	-2.16903E-08	7.89856E-09
RM100-30b-12	1.89159E-06	1.8522E-06	1.50818E-06	1.35097E-08	-1.2225E-08	1.4253E-08
RM100-30b-13	1.88271E-06	1.80198E-06	1.44817E-06	3.99374E-08	8.31933E-09	-8.77349E-09
RM100-30b-14	1.8881E-06	1.77873E-06	1.44687E-06	3.04258E-08	4.55313E-08	2.50292E-08
RM100-30b-15	2.03844E-06	1.96361E-06	1.5857E-06	2.78654E-08	3.09061E-09	-3.48643E-09
RM100-30b-16	2.16059E-06	2.07531E-06	1.71607E-06	1.8108E-08	1.0058E-09	1.12989E-08
RM100-30b-17	1.90895E-06	1.7994E-06	1.47895E-06	2.00785E-09	-3.59829E-09	-3.53375E-09
RM100-30b-18	2.03498E-06	1.93388E-06	1.58292E-06	2.06805E-08	1.05681E-08	3.53402E-08
RM100-30b-19	1.93994E-06	1.87806E-06	1.53981E-06	3.75329E-08	-1.27859E-08	2.64921E-08
RM100-30b-2	1.95534E-06	1.85659E-06	1.54801E-06	4.69305E-08	-2.96682E-09	1.98999E-08
RM100-30b-20	2.12454E-06	2.06194E-06	1.6816E-06	3.09449E-08	-3.00515E-09	9.39518E-09
RM100-30b-21	2.15944E-06	2.05489E-06	1.66574E-06	2.91882E-09	-1.74355E-08	1.16981E-08
RM100-30b-22	2.12025E-06	2.06834E-06	1.65822E-06	1.53437E-08	-8.80854E-10	1.34877E-08
RM100-30b-23	2.05179E-06	1.97252E-06	1.58126E-06	7.80972E-09	-5.41769E-09	7.18037E-09
RM100-30b-24	2.1237E-06	2.03873E-06	1.65347E-06	2.34726E-08	-8.46626E-09	1.26896E-08
RM100-30b-25	2.0349E-06	1.94602E-06	1.62524E-06	-2.05169E-08	-4.09294E-08	1.40467E-08
RM100-30b-3	1.99105E-06	1.8882E-06	1.55549E-06	2.83656E-08	1.18408E-08	7.39607E-09
RM100-30b-4	1.98193E-06	1.89561E-06	1.55502E-06	2.09556E-08	-5.16989E-09	1.25093E-08
RM100-30b-5	2.12297E-06	0.000002028	1.66232E-06	3.52035E-08	-9.91251E-10	2.4088E-08
RM100-30b-6	2.05041E-06	1.94189E-06	1.62412E-06	8.1716E-09	1.05918E-09	6.43457E-09
RM100-30b-7	1.88574E-06	1.78662E-06	1.51127E-06	3.4114E-08	6.38914E-09	5.26563E-09
RM100-30b-8	1.97745E-06	1.89315E-06	1.53347E-06	2.53689E-08	-1.22274E-08	1.71531E-08
RM100-30b-9	1.96878E-06	1.85838E-06	1.52988E-06	2.55602E-08	-1.57252E-09	1.46159E-08

100 μT, 60° Inclination

Tensor elements (upper half of symmetrical 3x3 matrix)

Specimen_ID	kxx	kyy	kzz	kxy	kyz	kzx
RM100-60-1	2.00621E-06	1.93846E-06	1.52991E-06	3.66914E-08	8.22632E-09	-2.22478E-08
RM100-60-10	2.15866E-06	2.09462E-06	1.69651E-06	2.22301E-08	-3.63023E-08	8.20574E-09
RM100-60-11	2.01182E-06	1.96209E-06	1.54479E-06	2.01191E-08	5.02076E-09	7.00523E-09
RM100-60-12	1.81944E-06	1.7715E-06	1.38269E-06	1.90775E-08	1.96865E-08	-2.75029E-09
RM100-60-13	2.11526E-06	2.00832E-06	1.69327E-06	-1.23424E-08	-2.55708E-08	-2.22114E-08
RM100-60-14	1.84277E-06	1.76685E-06	1.41605E-06	1.14224E-08	-9.20003E-09	-8.262E-09
RM100-60-15	2.17496E-06	2.09668E-06	1.71082E-06	2.28572E-08	-1.86004E-08	1.38258E-08
RM100-60-16	1.90185E-06	1.81946E-06	1.44782E-06	4.30938E-08	-8.79614E-09	8.25438E-09
RM100-60-17	1.96627E-06	1.87606E-06	1.53533E-06	3.79787E-08	-3.24424E-08	1.105E-08
RM100-60-18	1.90311E-06	1.83312E-06	1.47773E-06	2.0748E-08	-1.60091E-08	-1.16564E-08
RM100-60-19	1.87545E-06	1.80251E-06	1.46705E-06	1.77104E-08	-2.05775E-08	2.09422E-09
RM100-60-2	1.93327E-06	1.87622E-06	1.45943E-06	2.51137E-08	2.92011E-09	-1.14054E-09
RM100-60-20	2.11402E-06	2.03359E-06	1.70603E-06	2.60925E-08	-8.26287E-09	1.02709E-08
RM100-60-21	2.04903E-06	1.94937E-06	1.59786E-06	3.84543E-08	3.88144E-09	1.45463E-08
RM100-60-22	1.92589E-06	1.83993E-06	1.4541E-06	1.78603E-08	-3.89336E-09	6.8884E-09
RM100-60-23	2.11346E-06	2.03854E-06	1.66258E-06	3.27318E-08	-7.22025E-09	1.89687E-08
RM100-60-24	2.05138E-06	1.96971E-06	1.57642E-06	2.23121E-08	-6.44875E-09	2.19796E-08
RM100-60-25	2.01051E-06	1.9521E-06	1.65193E-06	1.80827E-08	5.16648E-11	9.10152E-09
RM100-60-3	2.0254E-06	1.94199E-06	1.51271E-06	3.23875E-08	-1.15673E-08	-1.62663E-08
RM100-60-4	1.90607E-06	1.83693E-06	1.43878E-06	1.30373E-08	-1.29697E-08	-6.16404E-10
RM100-60-5	2.08824E-06	2.00878E-06	1.6566E-06	1.33921E-08	1.93677E-09	-2.77937E-08
RM100-60-6	1.95056E-06	1.87329E-06	1.51143E-06	2.48992E-08	-4.20421E-09	-2.87575E-09
RM100-60-7	1.93169E-06	1.86014E-06	1.48361E-06	2.75565E-08	-6.79837E-09	-1.79587E-08
RM100-60-8	2.04807E-06	1.96503E-06	1.6022E-06	2.70018E-08	-8.22512E-10	1.38913E-11
RM100-60-9	1.77588E-06	1.72475E-06	1.38563E-06	2.04942E-08	-3.82748E-08	-9.76734E-09

100 μT, 90° Inclination

Tensor elements (upper half of symmetrical 3x3 matrix)

Specimen_ID	kxx	kyy	kzz	kxy	kyz	kzx
RM100-90b-1	2.46831E-06	2.40795E-06	2.01265E-06	1.57432E-08	-3.844E-08	2.68963E-08
RM100-90b-10	2.46387E-06	2.4327E-06	2.03437E-06	1.2871E-08	-4.96446E-09	-7.72538E-09
RM100-90b-11	2.41738E-06	2.36016E-06	1.99625E-06	9.51978E-09	-1.51797E-08	-1.17852E-08
RM100-90b-12	2.34952E-06	2.31788E-06	1.95431E-06	4.44223E-09	-1.53027E-08	-9.61297E-09
RM100-90b-13	2.47508E-06	2.42107E-06	1.98811E-06	4.55831E-09	2.37528E-08	-3.29371E-09
RM100-90b-14	2.49934E-06	2.45093E-06	2.0495E-06	1.17332E-08	1.36925E-09	9.78186E-09
RM100-90b-15	2.43369E-06	2.40101E-06	2.03017E-06	1.54783E-08	9.02875E-09	-1.37043E-08
RM100-90b-16	2.29612E-06	2.24008E-06	1.89469E-06	1.00787E-08	-1.50455E-08	1.29528E-08
RM100-90b-17	2.39647E-06	2.35985E-06	1.95554E-06	8.41252E-09	5.16042E-09	-4.75672E-09
RM100-90b-18	2.46398E-06	2.44282E-06	2.02346E-06	-1.19322E-08	5.59591E-09	-1.55009E-08
RM100-90b-19	2.51033E-06	2.4561E-06	2.04357E-06	9.76773E-09	3.48282E-09	1.86427E-08
RM100-90b-2	2.40466E-06	2.37537E-06	1.95972E-06	-1.59826E-08	-4.69327E-09	-1.65555E-08
RM100-90b-20	2.36262E-06	2.32484E-06	1.97599E-06	1.18089E-08	-1.25185E-08	-2.40183E-08
RM100-90b-21	2.46745E-06	2.40443E-06	2.0191E-06	2.78206E-08	4.9563E-09	2.39404E-08
RM100-90b-22	2.44066E-06	2.38388E-06	2.0483E-06	1.30341E-08	-1.05189E-08	-2.69944E-09
RM100-90b-23	2.52831E-06	2.48403E-06	2.14458E-06	1.38084E-08	-2.00981E-08	1.46604E-08
RM100-90b-24	2.34451E-06	2.34384E-06	1.96472E-06	1.62773E-08	-1.84291E-08	-5.67051E-09
RM100-90b-25	2.37421E-06	2.22333E-06	2.00322E-06	-3.12705E-07	-1.94374E-08	1.56266E-08
RM100-90b-3	2.4021E-06	2.34888E-06	1.96015E-06	2.92501E-08	-5.23883E-09	2.48179E-08
RM100-90b-4	2.30303E-06	2.23449E-06	1.91561E-06	4.05618E-08	-2.50458E-08	5.65244E-09
RM100-90b-5	2.33855E-06	2.29058E-06	1.92626E-06	1.16942E-08	8.74478E-09	4.55072E-09
RM100-90b-7	2.39858E-06	2.34015E-06	1.97212E-06	1.28323E-08	-1.98008E-09	-1.30018E-08
RM100-90b-8	2.30221E-06	2.22644E-06	1.88718E-06	-3.38667E-08	-4.88742E-08	-5.45493E-08
RM100-90b-9	2.29657E-06	2.26769E-06	1.89918E-06	5.10529E-09	1.68087E-09	-1.48205E-08